



UNIVERSITY OF THESSALY  
SCHOOL OF ENGINEERING  
DEPARTMENT OF MECHANICAL ENGINEERING

# Experimental Investigation of Droplet Impingement on Dry Solid Surfaces

---

By  
Lymperopoulou Ilianna  
Trovas Georgios

Submitted in partial fulfilment of the requirements for the diploma of Mechanical Engineering  
VOLOS 2020

© 2020 Lymperopoulou Ilianna, Trovas Georgios

The approval of the diploma thesis by the Department of Mechanical Engineering of the University of Thessaly does not imply acceptance of the author's opinion (Law 5343/32 article, 202 paragraph.2).

Certified by the members of the Thesis Committee:

First examiner            Dr. Georgios Charalampous  
[Supervisor]             Assistant Professor, Department of Mechanical Engineering,  
University of Thessaly

Second examiner        Dr. Anastasios Stamatellos  
Professor, Department of Mechanical Engineering,  
University of Thessaly

Third examiner         Dr. Nikolaos Pelekasis  
Professor, Department of Mechanical Engineering,  
University of Thessaly

# Abstract

The current thesis examines the droplet impingement on solid dry surfaces. This phenomenon affects a great range of industrial applications. The effect is examined on two aluminum surfaces one smooth ( $0.45\mu\text{m}$ ) and one of  $4.3\mu\text{m}$  roughness value (Ra). These surfaces are placed on a flat plane and on inclined planes of  $10^\circ$ ,  $20^\circ$  and  $30^\circ$  with respect to the horizontal x-axis in order to examine symmetric and asymmetric impact. The droplets detach from the lip of a syringe. The height of the syringe is adjusted at several heights, resulting in different Weber and Reynolds numbers during impact. The liquids of the droplets are distilled water-methanol mixtures. Beginning from pure distilled water 100% w/w, each time adding 20% w/w methanol for the next mixture till the last which is pure methanol 100% w/w. The collision moment is captured on a CCD camera and the images are processed. On each image the spreading diameter is measured. For the images where a splashing event is documented, the angles formed between the crown and the surface are measured on each side. Moreover, a pertinent splashing threshold is researched. The results are depicted on diagrams in order to reveal trends and differences for the variable circumstances of the experiment.

# Περίληψη

Η παρούσα διπλωματική εργασία εξετάζει την επίδραση σταγόνων σε στεγνές στερεές επιφάνειες. Αυτό το φαινόμενο επηρεάζει ένα μεγάλο εύρος βιομηχανικών εφαρμογών. Η επίδραση των σταγόνων εξετάζεται για 2 επιφάνειες από αλουμίνιο, μια σχεδόν λεία ( $0.45\mu\text{m}$ ) και μια με ονομαστική τραχύτητα  $4.3\mu\text{m}$ . Οι επιφάνειες τοποθετούνται είτε επίπεδες είτε επικλινείς  $10^\circ$ ,  $20^\circ$  και  $30^\circ$  σε σχέση με τον οριζόντιο άξονα  $x$ . Οι σταγόνες αποκολλώνται από το χείλος μίας σύριγγας. Το ύψος της σύριγγας ρυθμίζεται σε διάφορα ύψη, αποδίδοντας διαφορετικούς αριθμούς Weber και Reynolds κατά τη πρόσκρουση. Τα υγρά που χρησιμοποιούνται για τις σταγόνες είναι μίγματα αποσταγμένου νερού και μεθανόλης. Ξεκινώντας από καθαρό νερό 100% κατά βάρος, προσθέτοντας κάθε φορά 20% μεθανόλη κατά βάρος για το επόμενο μίγμα έως το τελευταίο που είναι καθαρή μεθανόλη 100% κατά βάρος. Η στιγμή της πρόσκρουσης καταγράφεται από μια κάμερα CCD και ακολουθεί η επεξεργασία των εικόνων. Σε κάθε εικόνα μετριέται η διάμετρος της σταγόνας που απλώνεται. Για τις εικόνες που παρατηρείται *splashing*, μετριέται η γωνία που σχηματίζεται μεταξύ της κορώνας και της στερεής επιφάνειας σε κάθε πλευρά. Επιπλέον αναζητείται ένα σχετικό όριο εκκίνησης του *splashing*. Τα αποτελέσματα αποτυπώνονται σε διαγράμματα, προκειμένου να παρατηρηθούν τάσεις και διαφορές για τις μεταβαλλόμενες συνθήκες του πειράματος.

# Acknowledgements

Firstly, we would like to express our appreciation and gratitude to our academic supervisor Prof. Georgios Charalampous, for giving us the opportunity and the means to complete this Thesis. His constant guidance helped us overcome every difficulty during the experimental investigation and his crucial suggestions contributed highly to the outcome of our work.

We would also like to thank Laboratory staff member Mister Anastasios Dafereras for programming and installing the Arduino microcontroller device and thus making our work easier and more efficient.

Last but not least, we would like to thank our families. Without their support and encouragement this endeavor would have never been possible.

# Table of contents

1	Introduction .....	15
2	Boundary Conditions.....	16
2.1	Dimensionless Numbers .....	16
2.2	Surface Boundary Conditions.....	17
3	Regimes of impact.....	18
3.1	Deposition.....	20
3.2	Rebound.....	21
3.3	Splashing .....	22
3.3.1	Splashing Threshold .....	23
3.3.2	Impact Parameters.....	25
3.3.3	Liquid Properties .....	28
3.3.4	Substrate Characteristics .....	31
3.3.5	Surface Wettability .....	32
3.3.6	Surrounding Gas Characteristics .....	33
3.3.7	Air Entrapment.....	34
3.4	Thesis Aim and Objectives .....	36
4	Methods.....	37
4.1	Experimental Setup.....	37
4.1.1	Support Structure.....	38
4.1.2	Arduino.....	38
4.1.3	Droplets.....	39
4.1.4	Camera .....	47
4.1.5	Illumination .....	47
4.1.6	Substrates .....	48
4.2	Image Processing .....	49
5	Results and Discussion .....	50
5.1	Vander Wals Criterion for Splashing on Flat Surfaces .....	50
5.2	Corona Splash .....	51
5.2.1	Formation and Disintegration.....	51
5.2.2	Splashing Angles.....	52

5.2.3	Riboux-Gordillo Criterion – Inclined Surfaces .....	63
5.3	Spreading Lamella .....	84
5.3.1	Temporal evolution for different solutions and inclinations .....	84
5.3.2	Surface Roughness .....	94
5.3.3	Characteristic Time To .....	106
6	Conclusions .....	111
7	References .....	113



# List of Figures

Figure 1.1: Droplet impact on super hydrophobic surface (Girard et al., 2019). .....	15
Figure 2.1: Dependence of the surface wettability on the contact angle( Pochylý et al., 2010). .....	17
Figure 2.2: Advancing and receding contact angles.....	18
Figure 2.3: a) Wenzel homogeneous wetting and b) Cassie-Baxter heterogeneous wetting on a rough surface(Qu et al., 2007).....	18
Figure 3.1: a) Prompt splash, b) Corona splash, c) Receding breakup, d) Rebound, e) Partial rebound and f) Deposition( Charalampous & Hardalupas, 2017).....	19
Figure 3.2: Corona splash and prompt splash. The photograph on the left is a corona splash on a smooth dry surface. Droplets are created from a symmetric corona. In the photograph on the right, a prompt splash occurs on a rough dry surface. In this case there is no corona and droplets are ejected from the advancing contact line. From Xu, Barcos, & Nagel, 2007.....	23
Figure 3.3: Map depicting the outcome of drop impact at normal ambient pressure ( Roisman et al., 2015). .....	25
Figure 3.4: A water droplet of diameter 3.7 mm, traveling at 10 m/s, impacts a smooth dry glass surface surrounded by air. This example of a prompt splash shows the ejection of secondary droplets from the spreading rim at the surface; scale bar 500 $\mu\text{m}$ . From (Burzynski & Bansmer, 2019). .....	26
Figure 3.5: Splash of an isopropanol droplet on smooth glass ( $We=544$ , surface angle $45^\circ$ ). Image from Šikalo, Tropea, & Ganić (2005). .....	26
Figure 3.6: Schematic of oblique droplet impact. (a) The droplet falls at a velocity $v_d$ , the substrate moves horizontally at a velocity $v_s$ , (b) $v_n$ and $v_t$ are the drop's normal and tangential velocity respectively. From (Aboud & Kietzig, 2015). .....	27
Figure 3.7: The model predicts three behaviors based on the magnitude of the tangential velocity: the lamella will spread in all directions (white symbols), splash in all directions (black symbols) or asymmetrically splash (gray symbols). Experiment with ethanol drops on to a dry, smooth, aluminum surface. Here $K=5700$ . From Bird et al., 2009. ....	28
Figure 3.8: The range of the $We$ and $Re$ numbers of various studies: (a) (Mundo et al., 1995), (b) (Vander Wal et al., 2006), (c) (Stevens, 2014), (d) (Bird et al., 2009), (e) (Palacios, Hernández, Gómez, Zanzi, & López, 2013), (f) (Riboux & Gordillo, 2014), and (g) (Almohammadi & Amirfazli, 2019). Experimental data of previous studies are not depicted in a single plot as the roughness and wettability of the surfaces differ from one study to another. From Almohammadi et al. 2019. ....	29
Figure 3.9: Impact outcomes for drops of (a) glycerol-water mixture (high surface tension); (b) silicone oil (low surface tension) onto surfaces with different wettabilities. Open symbols signify spreading; gray and black filled symbols denote prompt and corona splashing, respectively. The shaded region indicates the splashing regions, and the lines denote the splashing boundary to guide the eye. The maximum standard deviation for the droplet velocity is 0.08 m/s, so error bars are not shown. From Almohammadi et al. (2019). .....	30
Figure 3.10: Scheme of the radial stream inside a drop during its impact on a solid wall, after Levin and Hobbs. The arrows outside the drop indicate the forces due to surface tension). .....	31
Figure 3.11: The roughness of the glass and mica surfaces: AFM topographic images of 30x30 mm regions of (a) Corning glass, (b) Fisher glass and (c) freshly cleaved mica surface. For the Corning glass, $RMS=7.3$ nm, max. to min. =49 nm; for the Fisher glass, $RMS=1.2$ nm, max. to min. =10 nm; for the mica, $RMS < 0.5$ nm. From Li, Vakarelski, & Thoroddsen (2015). .....	31
Figure 3.12: Photographs of a liquid drop hitting a smooth dry substrate. A $3.4 \pm 0.1$ mm diameter alcohol drop hits a smooth glass substrate at impact velocity $V_0=3.74 \pm 0.02$ m/s. In the top row, with the air atmospheric pressure, the drop splashes. In the second row, with the air just slightly above the threshold pressure, $P_T=38,4$ kPa, the drop emits only a few droplets. In the third row, at a pressure of 30.0 kPa, no droplets are emitted and no splashing occurs. However, there is an undulation in the thickness of the rim. In the fourth row, taken at 17.2 kPa, there is no splashing and no apparent undulations in the rim of the drop. From Xu et al. (2005). .....	34

Figure 3.13: X-ray imaging setup for the entrapment of an air disc and its contraction into an air bubble, with a subsatellite pinched off at its center (Lee et al.2012). .....	35
Figure 4.1: Diagram of the experimental apparatus. ....	37
Figure 4.2: Drop impact aluminum support structure. ....	38
Figure 4.3: The Arduino microcontroller-LCD Keypad system showing regulating the wanted capturing delay. ....	39
Figure 4.4: Droplets crossing the photo interrupter (black). ....	39
Figure 4.5: The syringe pump .....	41
Figure 4.6: The deionizing column. ....	41
Figure 4.7: Forces acting on a free-falling drop under air resistance effects. ....	41
Figure 4.8: Graph depiction of the time values of set delay (blue dots) and free-fall (orange dots). ....	43
Figure 4.9: Image capture with exposure at 2000 $\mu$ s .....	46
Figure 4.10: TSI Powerview plus HS-200. ....	47
Figure 4.11: SIGMA 70-200mm F.2.8 APO zoom lens. ....	<b>Error! Bookmark not defined.</b>
Figure 4.12: Illumination source. ....	48
Figure 4.13: Metal base for adjusting impact angle. ....	49
Figure 4.14: Images processed at ImageJ a) Ruler distance selected in order to set a stable scale, b) Measured drop diameter in pixels after the impact. Converted to mm distance after scaling comparison with a. ....	49
Figure 5.1: (a) deposition (100% solution on smooth flat substrate, drop falling from 88cm, $u=3.449$ m/s, $We=1352.28$ ), (b) prompt splash (20% solution on P24 substrate tilted by 10 degrees, drop falling from 99cm, $u=3.802$ m/s, $We=1197.20$ ), (c) corona splash (60% solution on smooth flat substrate, drop falling from 99cm, $u=3.678$ m/s, $We=1431.38$ ).....	50
Figure 5.2: Splash behavior of several mixtures of distilled water-methanol, plotted with respect to the dimensionless Reynolds and Ohnesorge numbers. The equation for the border fit line is included on the graph.....	51
Figure 5.3: Splashing of 40% water-methanol solution, impacting on the smooth substrate from 100cm height. ....	52
Figure 5.4: Crown angles on the left and right side for horizontal substrate, $H=0.99$ m .....	53
Figure 5.5: Crown angles on the upslope (left) and downslope (right) side for inclination of $\vartheta=10^\circ$ , $H=0.99$ m .....	54
Figure 5.6: Crown angles on the upslope (left) and downslope (right) side for inclination of $\vartheta=20^\circ$ , $H=0.99$ m .....	55
Figure 5.7: Crown angles on the upslope (left) and downslope (right) side for inclination of $\vartheta=30^\circ$ , $H=0.99$ m .....	56
Figure 5.8: Crown angles on the left and right side for horizontal substrate, $H=0.89$ m .....	56
Figure 5.9: Crown angles on the upslope (left) and downslope (right) side for inclination of $\vartheta=10^\circ$ , $H=0.89$ m .....	57
Figure 5.10: Crown angles on the upslope (left) and downslope (right) side for inclination of $\vartheta=20^\circ$ , $H=0.89$ m .....	58
Figure 5.11: Crown angles on the upslope (left) and downslope (right) side or inclination of $\vartheta=30^\circ$ , $H=0.89$ m.....	59
Figure 5.12: Crown angles on the left and right side for horizontal substrate, $H=0.79$ m .....	59
Figure 5.13: Crown angles on the upslope (left) and downslope (right) side for inclination of $\vartheta=10^\circ$ , $H=0.79$ m .....	60
Figure 5.14: Crown angles on the upslope (left) and downslope (right) side for inclination of $\vartheta=20^\circ$ , $H=0.79$ m .....	61
Figure 5.15: Crown angle on the downslope (right) side for inclination of $\vartheta=30^\circ$ , $H=0.79$ m .....	62
Figure 5.16: Riboux-Gordillo velocity thresholds for 40% water-methanol solution at 10 degrees tilt angle. ....	64
Figure 5.17: 40% w/w methanol solution at 10 degrees tilt angle.....	65
Figure 5.18: Riboux-Gordillo velocity thresholds for 40% water-methanol solution at 20 degrees tilt angle. ....	65
Figure 5.19: 40% w/w methanol solution at 20 degrees tilt angle.....	66
Figure 5.20: Riboux-Gordillo velocity thresholds for 40% water-methanol solution at 30 degrees tilt angle. ....	66
Figure 5.21: 40% w/w methanol solution at 30 degrees tilt angle.....	67
Figure 5.22: Riboux-Gordillo velocity thresholds for 60% water-methanol solution at 10 degrees tilt angle. ....	68
Figure 5.23: 60% w/w methanol solution at 10 degrees tilt angle.....	68
Figure 5.24: Riboux-Gordillo velocity thresholds for 60% water-methanol solution at 20 degrees tilt angle. ....	69
Figure 5.25: 60% w/w methanol solution at 20 degrees tilt angle.....	69
Figure 5.26: Riboux-Gordillo velocity thresholds for 60% water-methanol solution at 30 degrees tilt angle. ....	70
Figure 5.27: 60% w/w methanol solution at 30 degrees tilt angle.....	70
Figure 5.28: Riboux-Gordillo velocity thresholds for 80% water-methanol solution at 10 degrees tilt angle. ....	71

Figure 5.29: 80% w/w methanol solution at 10 degrees tilt angle.....	71
Figure 5.30: Riboux-Gordillo velocity thresholds for 80% water-methanol solution at 20 degrees tilt angle. ....	72
Figure 5.31: 80% w/w methanol solution at 20 degrees tilt angle.....	72
Figure 5.32: Riboux-Gordillo velocity thresholds for 80% water-methanol solution at 30 degrees tilt angle. ....	73
Figure 5.33: 80% w/w methanol solution at 30 degrees tilt angle.....	73
Figure 5.34: Riboux-Gordillo velocity thresholds for 100% water-methanol solution at 10 degrees tilt angle. ....	74
Figure 5.35: 100% w/w methanol solution at 10 degrees tilt angle.....	74
Figure 5.36: Riboux-Gordillo velocity thresholds for 100% water-methanol solution at 20 degrees tilt angle. ....	75
Figure 5.37: 100% w/w methanol solution at 20 degrees tilt angle.....	75
Figure 5.38: Riboux-Gordillo velocity thresholds for 100% water-methanol solution at 30 degrees tilt angle. ....	76
Figure 5.39: 100% w/w methanol solution at 20 degrees tilt angle.....	76
Figure 5.40: Riboux-Gordillo velocity thresholds for 20% water-methanol solution at 10 degrees tilt angle. ....	77
Figure 5.41: 20% w/w methanol solution at 10 degrees tilt angle.....	77
Figure 5.42: Riboux-Gordillo velocity thresholds for 20% water-methanol solution at 20 degrees tilt angle. ....	78
Figure 5.43: 20% w/w methanol solution at 20 degrees tilt angle.....	78
Figure 5.44: Riboux-Gordillo velocity thresholds for 20% water-methanol solution at 30 degrees tilt angle. ....	79
Figure 5.45: 20% w/w methanol solution at 30 degrees tilt angle.....	79
Figure 5.46: Riboux-Gordillo velocity thresholds for 0% water-methanol solution at 10 degrees tilt angle. ....	80
Figure 5.47: Pure water at 10 degrees tilt angle.....	80
Figure 5.48: Riboux-Gordillo velocity thresholds for 0% water-methanol solution at 20 degrees tilt angle. ....	80
Figure 5.49: Pure water at 20 degrees tilt angle.....	81
Figure 5.50: Riboux-Gordillo velocity thresholds for 0% water-methanol solution at 30 degrees tilt angle. ....	81
Figure 5.51: Pure water at 30 degrees tilt angle.....	81
Figure 5.52: Spreading diameter evolution for horizontal and 10° inclined substrate, H=0.99m, Ra=0.45μm.....	85
Figure 5.53: Spreading diameter evolution for 20° and 30° inclined substrate, H=0.99m, Ra=0.45μm.....	86
Figure 5.54: Spreading diameter evolution for horizontal and 10° inclined substrate, H=0.89m, Ra=0.45μm.....	87
Figure 5.55: Spreading diameter evolution for 20° and 30° inclined substrate, H=0.89m, Ra=0.45μm.....	87
Figure 5.56: Spreading diameter evolution for horizontal and 10° inclined substrate, H=0.79m, Ra=0.45μm.....	88
Figure 5.57: Spreading diameter evolution for 20° and 30° inclined substrate, H=0.79m, Ra=0.45μm.....	89
Figure 5.58: Spreading diameter evolution for horizontal and 10° inclined substrate, H=0.99m, Ra=4.3μm.....	90
Figure 5.59: Spreading diameter evolution for 20° and 30° inclined substrate, H=0.99m, Ra=4.3μm.....	91
Figure 5.60: Spreading diameter evolution for horizontal and 10° inclined substrate, H=0.89m, Ra=4.3μm.....	92
Figure 5.61: Spreading diameter evolution for 20° and 30° inclined substrate, H=0.89m, Ra=4.3μm.....	92
Figure 5.62: Spreading diameter evolution for horizontal and 10° inclined substrate, H=0.79m, Ra=4.3μm.....	93
Figure 5.63: Spreading diameter evolution for 20° and 30° inclined substrate, H=0.79m, Ra=4.3μm.....	94
Figure 5.64: 0% w/w methanol solution (We=B. 765.89, We=909.43, We=971.39 for 80, 90 and 100 cm respectively).	95
Figure 5.65: 0% w/w methanol solution (We=B. 765.89, We=909.43, We=971.39 for 80, 90 and 100 cm respectively).	95
Figure 5.66: 0% w/w methanol solution (We=765.89, We=909.43, We=971.39 for 80, 90 and 100 cm respectively). .	95
Figure 5.67: 0% w/w methanol solution (We=765.89, We=909.43, We=971.39 for 80, 90 and 100 cm respectively). .	96
Figure 5.68: 20% w/w methanol solution (We=986.35, We=1125.26, We=1197.2 for 80, 90 and 100 cm respectively).	96
.....	
Figure 5.69: 20% w/w methanol solution (We=986.35, We=1125.26, We=1197.2 for 80, 90 and 100 cm respectively).	97
.....	
Figure 5.70: 20% w/w methanol solution (We=986.35, We=1125.26, We=1197.2 for 80, 90 and 100 cm respectively).	97
.....	
Figure 5.71: 20% w/w methanol solution (We=986.35, We=1125.26, We=1197.2 for 80, 90 and 100 cm respectively).	98
.....	

Figure 5.72: 40% w/w methanol solution ( $We=1233.33$ , $We=1390.58$ , $We=1462.99$ for 80, 90 and 100 cm respectively).....	98
Figure 5.73: 40% w/w methanol solution ( $We=1233.33$ , $We=1390.58$ , $We=1462.99$ for 80, 90 and 100 cm respectively).....	99
Figure 5.74: 40% w/w methanol solution ( $We=1233.33$ , $We=1390.58$ , $We=1462.99$ for 80, 90 and 100 cm respectively).....	99
Figure 5.75: 40% w/w methanol solution ( $We=1233.33$ , $We=1390.58$ , $We=1462.99$ for 80, 90 and 100 cm respectively).....	100
Figure 5.76: 60% w/w methanol solution ( $We=1124.52$ , $We=1295.45$ , $We=1431.38$ for 80, 90 and 100 cm respectively).....	100
Figure 5.77: 60% w/w methanol solution ( $We=1124.52$ , $We=1295.45$ , $We=1431.38$ for 80, 90 and 100 cm respectively).....	101
Figure 5.78: 60% w/w methanol solution ( $We=1124.52$ , $We=1295.45$ , $We=1431.38$ for 80, 90 and 100 cm respectively).....	101
Figure 5.79: 60% w/w methanol solution ( $We=1124.52$ , $We=1295.45$ , $We=1431.38$ for 80, 90 and 100 cm respectively).....	102
Figure 5.80: 80% w/w methanol solution ( $We=1183.17$ , $We=1321.50$ , $We=1448.52$ for 80, 90 and 100 cm respectively).....	102
Figure 5.81: 80% w/w methanol solution ( $We=1183.17$ , $We=1321.50$ , $We=1448.52$ for 80, 90 and 100 cm respectively).....	103
Figure 5.82: 80% w/w methanol solution ( $We=1183.17$ , $We=1321.50$ , $We=1448.52$ for 80, 90 and 100 cm respectively).....	103
Figure 5.83: 80% w/w methanol solution ( $We=1183.17$ , $We=1321.50$ , $We=1448.52$ for 80, 90 and 100 cm respectively).....	104
Figure 5.84: 100% w/w methanol solution ( $We=1225.99$ , $We=1352.28$ , $We=1490.52$ for 80, 90 and 100 cm respectively).....	104
Figure 5.85: 100% w/w methanol solution ( $We=1225.99$ , $We=1352.28$ , $We=1490.52$ for 80, 90 and 100 cm respectively).....	105
Figure 5.86: 100% w/w methanol solution ( $We=1225.99$ , $We=1352.28$ , $We=1490.52$ for 80, 90 and 100 cm respectively).....	105
Figure 5.87: 100% w/w methanol solution ( $We=1225.99$ , $We=1352.28$ , $We=1490.52$ for 80, 90 and 100 cm respectively).....	106
Figure 5.88: Approximation of the experimental curve based on equation (38) .....	107
Figure 5.89: Characteristic time $T_0$ values for pure water.....	107
Figure 5.90: Characteristic time $T_0$ values for 20% w/w methanol solution.....	108
Figure 5.91: Characteristic time $T_0$ values for 40% w/w methanol solution.....	108
Figure 5.92: Characteristic time $T_0$ values for 60% w/w methanol solution.....	109
Figure 5.93: Characteristic time $T_0$ values for 80% w/w methanol solution.....	109
Figure 5.94: Characteristic time $T_0$ values for 100% w/w methanol solution. ....	110

# List of Tables

Table 3.1: Effect of boundary conditions on the regimes of impact (Romain Rioboo & Marengo, 2001).....	19
Table 3.2: Spreading factor $\beta$ models (Josserand & Thoroddsen, 2016). .....	20
Table 3.3: Summary of the disintegration mechanism thresholds (Moreira et al., 2010). .....	24
Table 4.1: For each height value is shown the Arduino set delay (Time Impact, 2nd column), the height calculated for free-fall corresponding to this time value (3rd column), the calculated time of free-fall for this height (4th column) and the deviation between the 2 <sup>nd</sup> and 3 <sup>rd</sup> columns .....	43
Table 4.2: Calculation of impact time for a free-falling drop with initial velocity. Comparison of these values with the experimental ones. ....	44
Table 4.3: Values of diameter measured in the experiment and values of the diameter from Rayleigh-Plateau's instability, Tate's Law and Yildirim's dimensional analysis. ....	45
Table 4.4: Measurement of impact velocities for pure water .....	46
Table 4.5: a) Weber and b) Reynolds numbers for the liquid mixtures of the experiment .....	46
Table 5.1: Right side velocity deviations in m/s and percentage $(=(V_{exp}-V_{thr}) * 100 / V_{thr})$ . ....	82
Table 5.2: Left side velocity deviations in m/s and percentage $(=(V_{exp}-V_{thr}) * 100 / V_{thr})$ .....	83
Table 5.3: Kinematic viscosity for the solutions .....	84

## Nomenclature

$A$	Cross sectional area	$m^2$
$Ca$	Capillary number	–
$C_D$	Drag coefficient	–
$D$	Droplet diameter	$m$
$D_{ND}$	Dimensionless diameter	–
$Fr$	Froude number	–
$G$	Bond number	–
$Oh$	Ohnesorge number	–
$R_a$	Arithmetic average roughness	$m$
$Re$	Reynolds number	–
$R_l$	Lamella radius	$m$
$R_{ND}$	Dimensionless roughness	–
$R_{rms}$	Root mean square roughness	$m$
$t^*$	Dimensionless time	–
$U$	Droplet velocity	$m/s$
$V$	Sphere Volume	$m^3$
$We$	Weber number	–
$\beta$	Maximum spreading ratio	–
$\gamma$	Surface energy	$J/m^2$
$\theta$	Young's equilibrium angle	°
$\theta_a$	Advancing angle	°
$\theta_r$	Receding angle	°
$\mu$	Dynamic viscosity	$Pa \cdot s$
$\nu$	Kinematic viscosity	$m^2 \cdot s$
$\rho$	Density	$kg/m^3$
$\sigma$	Surface tension	$N/m$
$\varphi$	Angular position	°

# 1 Introduction

The interaction of liquid droplets with solid surfaces is a phenomenon that the human eye encounters on a daily basis. Either as a part of a physical procedure or as a part of a human driven procedure, the impact of a droplet on a surface is a vivid memory for everyone. In nature droplets impinge on earth's soil. This procedure causes erosion of the soil's properties and affects the surface morphology. The splashing of rain droplets is also known for facilitating the reproduction cycle of several fungus microorganisms. Moreover, the phenomenon is part of extensive scientific research because it concerns a great deal of applications in several engineering and industrial branches. Knowledge earned upon the mechanisms of this interaction is applied as a means of improving inkjet printing efficiency (avoidance of satellite ink droplets formation). The effects of break-off of jets, emanating from a spray nozzle, into droplets are researched in experiments concerning combustion chamber anti-pollution technology and pesticide scattering, for environmental purposes (Moreira et al., 2010). Furthermore anti-icing surfaces, that prevent the accumulation of ice on surfaces, wing tips, cables etc., are developed (Girard et al., 2019)(**Figure 1-1**) Other applications where drop impact plays an important role are rapid spray cooling, spray drying, spray coating of surfaces, desalination of water, forensic science and encapsulation mechanisms.



*Figure 1-1: Droplet impact on super hydrophobic surface (Girard et al., 2019).*

The impact phenomenon and its subsequent effects rely on a great range of conditions and parameters. Indicatively the shape and the oscillation frequency of the drop during impact are important (Ashgriz, 2011). The angle of impact (perpendicular or inclined) can have a great effect on the outcome. Moreover, Newtonian and non-Newtonian liquids behave extremely different

under the same conditions. The first experimental investigation of the phenomenon dates back over a century (Worthington,1876), when the impact of mercury drops on a glass surface was researched. Though the analytical solution of the problem presents great complexity, due to the number of parameters involved, the development of numerical algorithms, provided valuable information. In addition, the advent of high-speed video technology, provided time resolved images and enabled us to better understand the underlying rapid dynamics of the impact process (Thoroddsen et al., 2008).

## 2 Boundary Conditions

The decisive factors to the outcome of the droplet impingement on the solid substrate are known as the boundary conditions of the procedure. They consist of the physical properties of the liquid, the kinematic conditions of the interaction, the surface conditions of the substrate and the surrounding air conditions.

### 2.1 Dimensionless Numbers

In order to interpret the behavior of the {droplet-solid surface-surrounding gas} system, a group of dimensionless numbers is used. They are generated through the combination of the physical properties of the liquid, namely the droplet's dynamic viscosity  $\mu_l$ , density  $\rho_l$  and surface tension  $\sigma$ , the current kinematic conditions, namely the droplet's diameter  $D$  and velocity  $U$  and the dynamic viscosity  $\mu_g$  and density  $\rho_g$  of the surrounding gas. These dimensionless numbers that determine the system's dynamic evolution are the following.

$$Re = \frac{\rho_l U D}{\mu_l} \quad (1), \quad We = \frac{\rho_l U^2 D}{\sigma} \quad (2), \quad Oh = \frac{\sqrt{We}}{Re} = \frac{\mu_l}{\sqrt{\rho_l D \sigma}} \quad (3), \quad Ca = \frac{\mu_l U}{\sigma} \quad (4),$$

$$Fr = \frac{U}{\sqrt{gD}} \quad (5)$$

The Reynolds number expresses the ratio of inertial to viscous forces, the Weber number the ratio of inertial to surface tension forces, the Ohnesorge number is a combination of Reynolds and Weber, the Capillary number expresses the ratio of viscous to surface tension forces and the Froude number expresses the ratio of inertial to gravity forces. The fact that inertial forces greatly outnumber gravitational forces, render  $Fr \gg 1$ . Therefore, the gravitational effects can be considered negligible during the impact phenomenon. Further useful dimensionless expressions are the ratios of liquid-gas density and dynamic viscosity respectively.

$$\frac{\rho_l}{\rho_g} \quad (6), \quad \frac{\mu_l}{\mu_g} \quad (7)$$



## 2.2 Surface Boundary Conditions

The surface boundary conditions are not included on the dimensionless numbers, therefore their effects are expressed through the roughness and the wettability of the solid substrate. The roughness of the solid substrate is usually expressed as the arithmetic amplitude average roughness  $R_a$  and is given by

$$R_a = \frac{1}{n} \sum_{i=1}^n |y_i| \quad (8)$$

, where  $n$  is the number of intersections of the measured profile at the mean line and  $y_i$  is the vertical distance of the  $i_{th}$  point from the mean line. For simplicity it is a measure of the average surface roughness of the surface i.e. the average difference between the peaks and valleys of the surface. Root-mean-square roughness ( $R_{rms}$ ) is also commonly used. Sometimes in research the roughness effects are expressed through the dimensionless roughness  $R_{ND} = R_a/D$  (9). In addition, some studies use mean roughness  $R_z$ , average height of protruding peaks  $R_{pk}$  and mean width of a profile element  $R_{sm}$  (Roisman et al., 2015). Xu, Barcos, & Nagel, (2007) used the average particle diameter  $D_p$  (called  $R_a$  in their study).

The wettability of the solid substrate plays also a crucial role on the outcome of the collision with the liquid droplet. A quantification of the wettability of a solid surface is the contact angle or thermodynamic equilibrium angle  $\theta$  (Figure 2-1) namely the angle measured when a liquid-vapor interface meets a solid surface. The values of  $\theta$  range from 0 to 180 degrees. Based on rising  $\theta$  value, a surface can be classified as hydrophilic, neutral, hydrophobic and super hydrophobic.

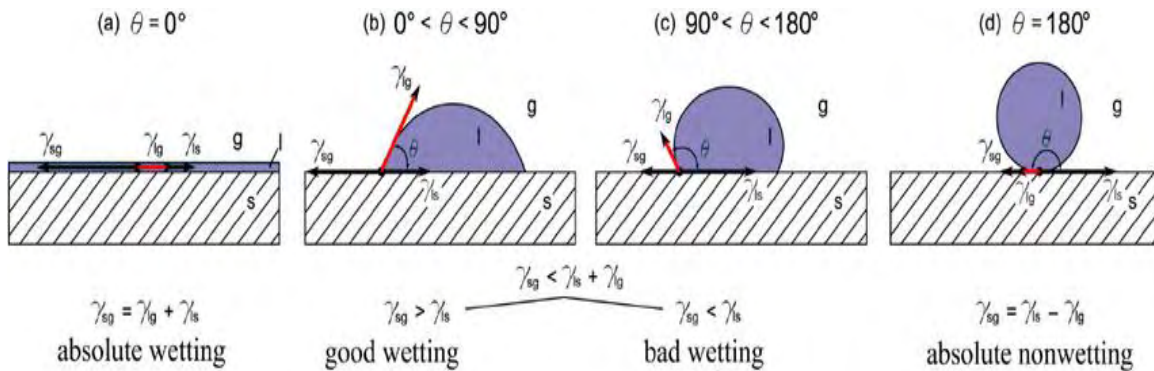


Figure 2-1: Dependence of the surface wettability on the contact angle (Pochylý et al., 2010).

In Figure 2-1 the quantities  $\gamma_{sl}$ ,  $\gamma_{lg}$  and  $\gamma_{sg}$  express the interfacial energy i.e. surface tension developed between the solid, liquid and gas phases. The value of the contact angle  $\theta$  derives from the Young equation (10), considering a thermodynamic equilibrium between the three phases for a smooth and homogeneous surface.

$$\gamma_{lg} \cos \theta = \gamma_{sg} - \gamma_{sl} \quad (10)$$

In general, we consider high wettability for  $\theta$  values below 90 degrees and low wettability for values above 90 degrees. Examples of high wettability regimes are high surface energy solids (e.g.

metals) in contact with low surface energy organic liquids (e.g. hexane), while impingement of high surface energy liquids (e.g. mercury) on low surface energy solids (e.g. polymers), indicate low wettability regimes. For real, not-ideal surface cases the experimentally found contact angle does not confirm the Young's equation theoretical one (Ukiwe & Kwok, 2005), (Romain Rioboo & Marengo, 2001). Hence the advancing contact angle  $\theta_a$  and receding contact angle  $\theta_r$  are more useful there. The advancing angle is the contact angle found at the advancing edge of a liquid drop, while the receding the one found at the receding edge, when the drop is moving on a tilted surface (Figure 2-2), (Liu et al., 2010). The wetting is further classified as homogeneous (Wenzel model) or heterogeneous (Cassie-Baxter model) on rough surfaces (Figure 2-3). Since the contact line is moving the dynamic advancing ( $\theta_a$ ) and receding ( $\theta_r$ ) contact angles also have to be considered, depending on whether the droplet edge is spreading outwards or retreating (Ashgriz, 2011).

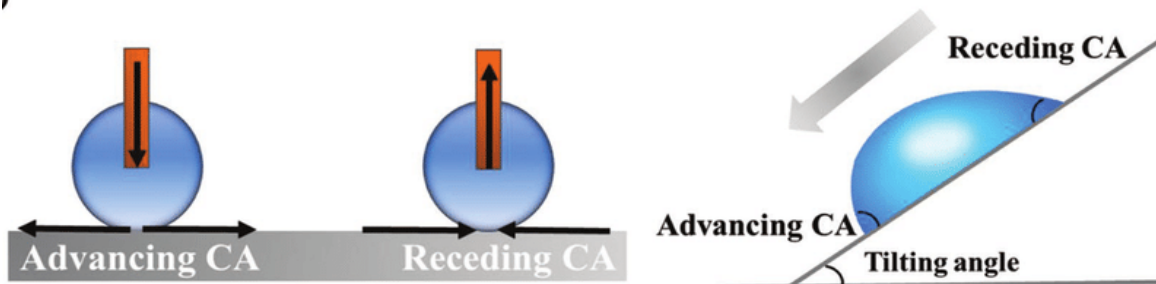


Figure 2-2: Advancing and receding contact angles.

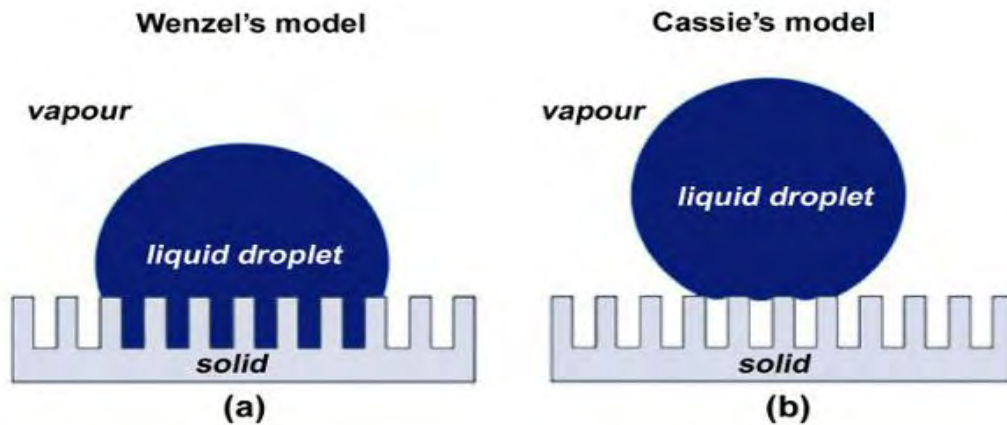


Figure 2-3: a) Wenzel homogeneous wetting and b) Cassie-Baxter heterogeneous wetting on a rough surface (Qu et al., 2007).

### 3 Regimes of impact

The possible regimes of a liquid droplet impinging on a solid surface are deposition, partial rebound, total rebound, corona splash, prompt splash and receding breakup (Romain Rioboo &

Marengo, 2001), (Figure 3-1). A summary of the influence of the boundary conditions on each regime is provided at Table 3.1.

An increase of	Deposition	Prompt splash	Receding breakup	Complete rebound	Corona splash	Partial rebound
$V$	↓	↑	↑		↑	↑
$D$	↓	↑				
$\sigma$		↓	↑	↑	↓	↑
$\mu$	↑	↓	↓		↓	
$R_a$	↓	↑			↓	
$R_w$		↓				
$\theta_{rec.}$			↑	↑		↑

Table 3.1: Effect of boundary conditions on the regimes of impact (Romain Rioboo & Marengo, 2001).

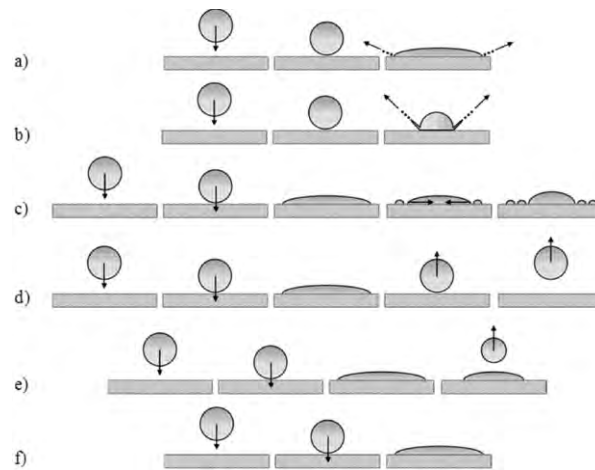


Figure 3-1: a) Prompt splash, b) Corona splash, c) Receding breakup, d) Rebound, e) Partial rebound and f) Deposition (Charalampous & Hardalupas, 2017)

The impact phenomenon consists of several phases, describing the temporal development of the droplet's diameter. The initial one is the kinematic, which is common in all outcomes. During this inertia dominated phase, there is no visible deformation of the droplet and the diameter  $D$  grows proportional to  $t^{*0.5}$ , where  $t^* = t/(D_0/U_0)$  (11), accounts for the dimensionless time passed since the impact moment (R Rioboo et al., 2002). This phase is terminated, when the radial expansion of the droplet's lamella begins. Afterwards, different behaviors are possible, depending on the boundary conditions of the impact. For splashing the disintegration mechanisms take action, while for deposition and rebound the spreading mechanisms. Thus, every regime is separately analyzed.

### 3.1 Deposition

The impact regime of deposition is characterized by the permanent attachment of the drop onto the substrate surface throughout all the phases (Romain Rioboo & Marengo, 2001). When the lamella ejection begins, this regime proceeds to the spreading phase, until the droplet’s diameter is maximized. The spreading factor  $\beta$  is used, to quantify the growth of the droplet’s diameter as a ratio between the maximum diameter and the initial one:

$$\beta = \frac{D_{max}}{D_0} \quad (12).$$

Vadillo, Soucemarianadin, Delattre, & Roux (2012), proposed that during this dynamic phase, inertial forces counteract with viscous and capillary forces that suppress the spreading.

Model	Expression	Comment
Scheller & Bousfield (1995)	$\beta \sim 0.61 (Re^2 Ob)^{1/6} = 0.61 Re^{1/5} (We Re^{-2/5})^{1/6}$	Empirical law based on experimental results
Pasandideh-Fard et al. (1996)	$\beta = \sqrt{\frac{We+12}{3(1-\cos\theta_d)+4(We/\sqrt{Re})}}$	Detailed energy balance, including contact angle ( $\theta_d$ ), and initial conditions
Ukiwe & Kwok (2005)	$(We + 12)\beta = 8 + \beta^3 \left( 3(1 - \cos \theta_d) + 4 \frac{We}{\sqrt{Re}} \right)$	Extension of the above model, with $\theta_d$ the dynamical contact angle during spreading
Clanet et al. (2004)	$\beta \propto We^{1/4}$	Mass balance using the impact capillary length
Roisman (2009)	$\beta \sim 0.87 Re^{1/5} - 0.4 Re^{2/5} We^{-1/2}$	Formula obtained using a dynamical model for the spreading of the drop involving a viscous boundary layer
Eggers et al. (2010)	$\beta = Re^{1/5} f(P)$	Similar approach to that in Roisman (2009); impact number $P$ is defined by $P = We Re^{-2/5}$

Table 3.2: Spreading factor  $\beta$  models (Josserand & Thoroddsen, 2016).

In order to describe the phase of spreading, a great deal of relations has been extracted from the analysis of the subtle balances between these forces. Some of them are presented at **Table 3.2**. Although all these relations derive from different impact conditions, approaches and formulations, they share a great deal of common results with experiments and numerical simulations. Therefore, we can assume two basic distinct conditions that define the spreading factor  $\beta$ . The one is governed by capillary forces, concerns liquids that are inviscid and non- or partial wetting substrates and  $\beta$  is proportional to  $We^{1/4}$ . The other is governed by viscous forces and  $\beta$  is proportional to  $Re^{1/5}$ . The effects of viscous dissipation are expressed through the energy conservation principle (Ashgriz, 2011):

$$E_{Ki} + E_{Si} = E_{Kf} + E_{Sf} + E_{diss} \quad (13)$$

, where  $E_K$  and  $E_S$  express the kinetic and surface energy at the initial and final stages respectively, and  $E_{diss}$  expresses the part of initial energy that dissipates due to viscous effects. Attempts to merge the two conditions have given some of the most accurate models (Eggers et al., 2010), (Roisman et al., 2014). In addition, (Clanet, 2004) considered the impact number  $P \equiv We/Re^{4/5}$  (14), as a correlation between the two conditions, where  $P=1$  describes the transition between the two states. For  $P$  values below 1 where the capillary state dominates, the drop is considered inviscid and the spreading is limited by capillarity, while for values above 1 where the viscous state dominates, the drop is considered viscous and the spreading is limited by viscosity effects. .

If the drop-substrate interaction allows partial wetting, the recoiling or receding phase initiates after the spreading phase has come to a conclusion. Under the effect of surface tension, the drop is retracted from the maximum diameter of the spreading phase to a lower diameter and its free surface is minimized. The receding contact angle  $\theta_r$  and the roughness influence the recoiling (R Rioboo et al., 2002). The diameter attained after the phase completion will be the final one, as the impact phenomenon concludes with the equilibrium phase. In contrary, if the drop-substrate interaction allows complete wetting, the spreading halts for some time. Afterwards it initiates again as part of the wetting phase. In the course of this phase the diameter grows proportional to  $t^{1/10}$  (Tanner, 1979) under the influence of capillary forces. Finally, the phenomenon reaches a constant diameter at the equilibrium phase.

## 3.2 Rebound

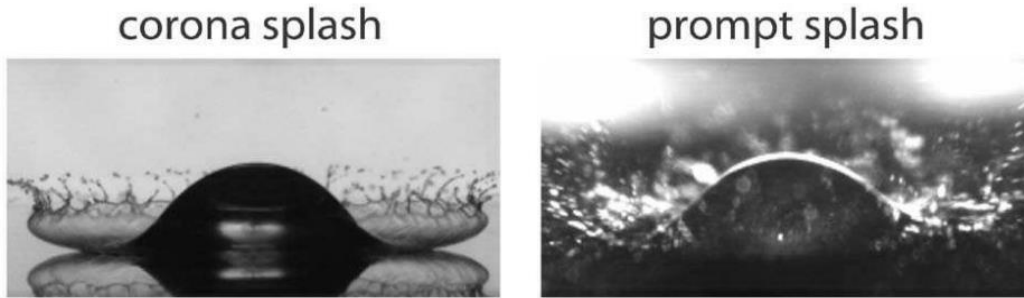
This regime occurs only when a receding phase is present. During retraction the whole droplet (total rebound) or a part of the droplet (partial) bounces from the substrate and starts moving upwards. Rioboo et al. described rebound as a regime where the impact energy is high and remains high enough during the receding phase. Similar observations were also made in other researches (Moreira et al., 2010), proposing that the dissipation energy  $E_{diss}$  should be low enough, in order to have high kinetic energy during retraction and achieve a rebound. Numerical simulations (Bange & Bhardwaj, 2015) revealed that the regime is achieved if the total energy at the time of maximum recoiling is greater than the initial surface and gravitational energy. After the droplet reaches the maximum diameter,  $D_{max}$  the recoiling phase begins and the droplet retracts. In cases of energetic retraction, capillary waves converge at the apex of the drops free surface and provide the mechanism for rebound (Josserand & Thoroddsen, 2016). Moreover high temperatures and especially the emergence of the Leidenfrost effect are believed to favor rebounding (Chandra & Avedisian, 1991). The regime concerns drop-substrate interactions that allow bad or no-wetting and is thus mainly observed for hydrophobic substrates. However for high enough impact velocities, even in the most hydrophobic substrates, the rebound could be partial because the possibility of lamella break-up during spreading is high (Josserand & Thoroddsen,

2016). The receding contact angle  $\theta_r$  is a determinant factor for the allowance of the rebound regime and the separation between total (high values) and partial rebound (low values). This angle is measured quasi-statically (considering a static droplet and extracting an amount of its liquid with a syringe,  $\theta_r$  is the instant angle before the contact area with the substrate is reduced) and is used to analyze the dynamic behavior of the interaction. Thus a transition from the Cassie-Baxter to the Wenzel state should be considered as a possibility (Antonini et al., 2013). When this transition happens the  $\theta_r$  drops rapidly and blocks the rebound regime.

Rebounding is a regime desired in self-cleaning and anti-icing applications. The aim of researchers investigating the phenomenon is the development of new super hydrophobic surfaces that promote the regime and reduce the contact time between the droplet and the substrate. Indicative are surfaces that promote the regime of pancake rebound, during which the droplet bounces from the substrate before lateral retraction happens and thus the contact time is further reduced (Moevius et al., 2014). A threshold value of  $\theta_r$  is used as a criterion of super hydrophobicity. X. Li, Ma, & Lan (2010), defined this threshold above  $138.6^\circ$  while  $135^\circ$  was the result of another experimental investigation (R Rioboo et al., 2012). Antonini et al. (2013), used wetting surfaces of  $\theta_r$  from  $89^\circ$  to  $161^\circ$  and concluded that rebounding occurs for values above  $100^\circ$  if the velocity during impact is sufficiently high for initial kinetic energy to overcome the dissipated energy.

### 3.3 Splashing

As discussed in the previous parts of the thesis, right after the impact, a falling drop spreads radially upon a cold solid surface, creating a lamella which can deposit, bounce off the substrate or disintegrate. The latter has been classified in two main categories according to when secondary drops are ejected. The first category is called prompt splash and is characterized by droplets generated directly from the contact line between the advancing lamella and the substrate, usually at a parallel direction to the latter. The droplets emerge at the beginning of the spreading phase when the lamella has high radial velocity. The second one is known as corona splash and the droplets are ejected from the rim of a liquid film in the shape of a bowl which occurs by the elevation of the lamella after it detaches from the substrate. The corona formation happens at a later stage of the impact process.



*Figure 3-2: Corona splash and prompt splash. The photograph on the left is a corona splash on a smooth dry surface. Droplets are created from a symmetric corona. In the photograph on the right, a prompt splash occurs on a rough dry surface. In this case there is no corona and droplets are ejected from the advancing contact line. From Xu, Barcos, & Nagel, 2007.*

Although the exact splashing mechanism has not been yet defined, in this section are discussed various parameters known to influence its result. These parameters include droplet kinematics (impact velocity and angle), liquid properties (viscosity, surface tension and density) as well as surface and surrounding gas characteristics.

### 3.3.1 Splashing Threshold

Many processes involving droplet-solid substrate interaction, are highly dependent on the splashing regime, its behavior and the underlying mechanisms affecting it. The splashing threshold is an empirical correlation deduced from experiments that investigated the transition from deposition impact regime to splashing impact regime.

The first attempt to find a deposition/splashing threshold was made in 1981 (Stow & Hadfield, 1981). The liquid used, was distilled water droplets and the solid substrate was HE30 aluminum alloy of variable roughness. The conclusion after repeating the experiment for various droplet diameters was that there exists a critical velocity, named  $V_T$ , below which the probability of splashing is negligible. A similar conclusion was latter made by another experimenter (Hao, 2017), who named  $V_{T1}$  the velocity below which occurs deposition,  $V_{T2}$  the velocity above which occurs corona splashing and proposed that for velocity values between those two occurs prompt splashing. These threshold velocities were determined by experiments with low-viscosity water, alcohol 16.6% and ethanol droplets of variable diameter, in order to include surface tension and droplet size effects. Stow et al. observed the weak dependence of the criterion on high roughness (above 1  $\mu\text{m}$ ) surfaces, thus the following criterion was proposed.

$$K = We\sqrt{Re} \quad (15)$$

This correlation is known as the splashing threshold and incorporates the inertial, viscous and surface tension effects. It is obvious, that the dimensionless numbers are essential to mathematically define this threshold criterion. The greater the  $K$  value, the greater the energy, that the droplet requires in order to splash. They proposed that for values of  $K$  above 3000 a



splash should be expected. It can be considered for a range of fluids among which is water. An alternative expression for correlation (15) is the ensuing:

$$K = AOh^aWe^b \quad (16)$$

Reference	$K_c = A Oh^a We^b$			Boundary conditions	Observations
	A	a	b		
Stow and Hadfield [60]	1	-0.37	1	Dry surfaces with different roughness.	$K_c = f(R_s)$ – the parameters a and b were adjusted as a function of $R_s$ in a logarithmical empirical adjustment. It is not explicit of which disintegration mechanism is being considered because the correlation is also adjusted to measurements of Stow and Stainer [66] who considered a wide range of data for impacts onto liquid films. Overall it is interpreted that the correlation was developed for prompt splash.
Wu [65]	1	0	1	Dry surfaces with different roughness.	Took the correlation of Stow and Hadfield [60], considering that for their experimental conditions Oh could be neglected. $K_c = We_c = f(R_s) = A_1 \log(R_s/R_0)^{b_1}$ where $A_1$ and $b_1$ depend on the properties of the liquid and on the nature of the surface [36,47].
Mundo et al. [61]	1	-0.4	1	Wetted surfaces with different roughness.	The authors compared 2 surfaces with very different roughness but did not observe relevant differences so that for them $K_c$ does not depend on $R_s$ . Later, Mundo et al. [67] recognized the presence of a liquid film over the surfaces which should explain the minor importance of the surface roughness.
Bai and Gosman [34]	Depends on surface roughness	0.36	0	Dry surfaces.	The correlation for dry surfaces was adjusted to the data of Stow and Hadfield [60].
Gavaises et al. [68]	1	0	1	-	$K_c = We_c = 100$ – major limitation is to consider a constant value for the threshold. Care must be taken before neglecting viscous effects [36,69].
Randy et al. [70]	1	0.4	-0.3	Dry smooth surfaces.	The correlation fits well the experimental data for high Reynolds numbers ( $Re > 7000$ ) but larger discrepancies with the experimental data are found as the inertial forces become less important ( $Re < 3000$ ).

**Table 3.3: Summary of the disintegration mechanism thresholds (Moreira et al., 2010).**

According to Table 3.3 different  $K$  values were deduced from different experimenters. Some claim dependence of the threshold on surface roughness (via the A parameter), while others don't have clues pointing to this observation. This indicates the extremely complex nature of the splashing due to the non-linearity of the phenomenon and justifies the fact that a universal correlation for the splashing threshold is yet to be established (Roisman et al., 2015).

Other experimental relations considering the splashing threshold are the following:

$$OhRe^{0.609} = 0.85 \quad (17)$$

(Vander Wal et al., 2006) that was extracted through experiments for a broad range of surface tension and viscosity fluids. Values greater than the numerical value, pointed to a splashing regime.

In addition,

$$Ca = 0.067 + 0.60h^{0.55} \quad (18) \quad \text{and} \quad Oh = 0.0044 \quad (19)$$

(Roisman et al., 2015), where relation (18) indicates the corona splash and the deposition/lamella lifting boundary, while relation (19) indicates the corona and prompt splash boundary. A map (Figure 3-3), of several research data, illustrates the values of  $We$  and  $Re$  that produce a splashing event.



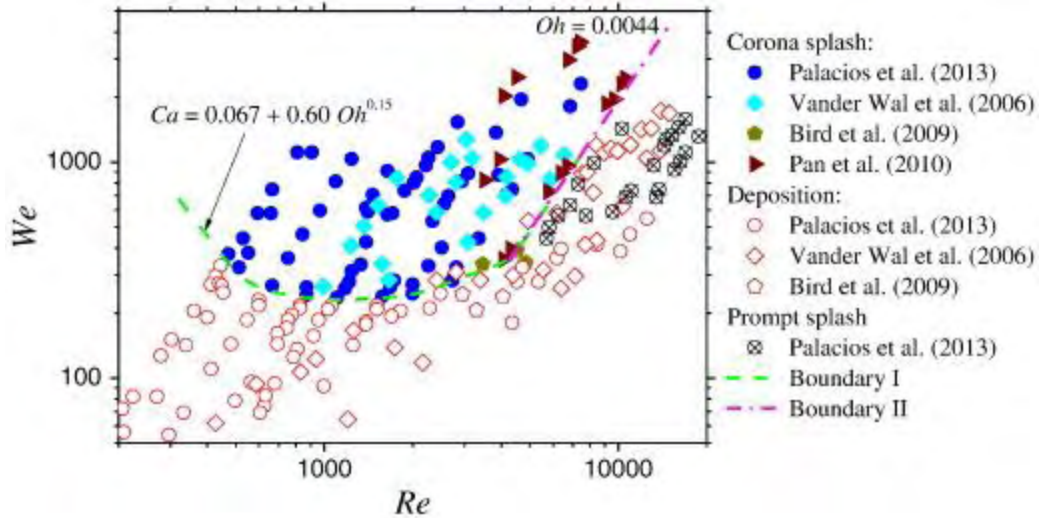


Figure 3-3: Map depicting the outcome of drop impact at normal ambient pressure ( Roisman et al., 2015).

Last but not least it should be mentioned that the surrounding gas pressure can affect the splashing behavior. Xu et al. (2005), discovered the suppression of splashing for pressure conditions lower than the atmospheric and proposed a pressure threshold  $P_T$  for splashing, dependent on impact velocity  $U_0$ .

### 3.3.2 Impact Parameters

With the term impact parameters, we refer to droplet kinematics and diameter.

#### 3.3.2.1 Impact Velocity (Normal)

Velocity is a dominant parameter regarding the impact outcome. In drop impacts on thin liquid films splashing threshold is almost solely based on velocity for a certain liquid (Yarin & Weiss 1995, Rioboo et al. 2002), except when the film is extremely thin and surface roughness becomes important (Cossali et al., 1997).

Drop impacts on dry surfaces exhibit more complicated flow patterns than those on wetted surfaces due to the influence of surface texture. As a result, velocity is always examined in relevance with surface roughness or wettability. However, it is experimentally confirmed that splashing occurs when the liquid drop hits a dry surface at high velocity (in the bibliography we based on, velocities vary from 1 to 30 m/s, at which compressibility effects in Newtonian liquids are negligible).

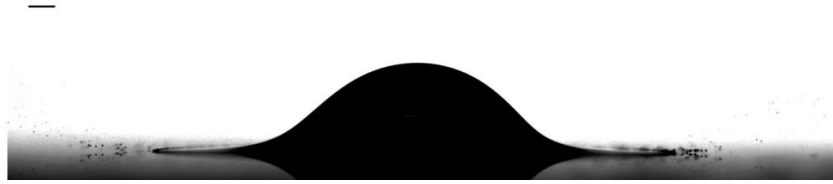


Figure 3-4: A water droplet of diameter 3.7 mm, traveling at 10 m/s, impacts a smooth dry glass surface surrounded by air. This example of a prompt splash shows the ejection of secondary droplets from the spreading rim at the surface; scale bar 500  $\mu\text{m}$ . From (Burzynski & Bansmer, 2019).

### 3.3.2.2 Impact Velocity (Tangential)

In many naturally occurring splashes and technical applications the drop does not impact normally on the surface or the surface is in motion. In both cases the impact velocity has a tangential component which alters the impact outcome and therefore has been under experimental investigation. Studies show that the splashing threshold can be estimated with the K parameter, using the normal velocity in its calculation (Stow & Hadfield, 1981; Mundo, Sommerfeld, & Tropea, 1995).

The asymmetry of collisions on inclined surfaces may lead to more complex impact behaviors such as one-sided corona/prompt splashing and corona-prompt splashing. During the latter corona and prompt splashes occur at each side of the lamella. Furthermore, H. Li (2013) observed unique splashing outcomes, while conducting experiments on moving inclined surfaces, such as the aerodynamic breakup and the splashing rebound.

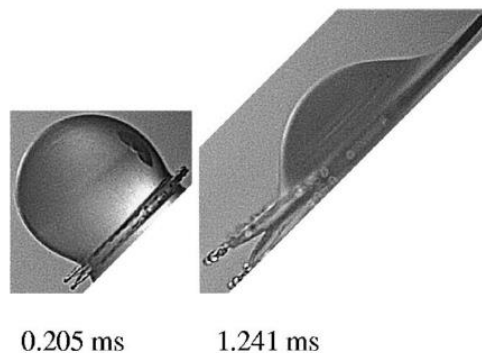


Figure 3-5: Splash of an isopropanol droplet on smooth glass ( $We=544$ , surface angle  $45^\circ$ ). Image from Šikalo, Tropea, & Ganić (2005).

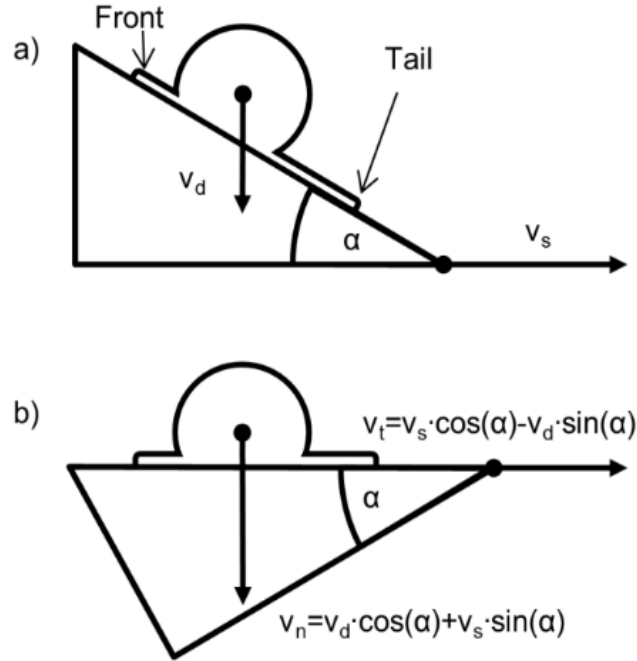


Figure 3-6: Schematic of oblique droplet impact. (a) The droplet falls at a velocity  $v_d$ , the substrate moves horizontally at a velocity  $v_s$ , (b)  $v_n$  and  $v_t$  are the drop's normal and tangential velocity respectively. From (Aboud & Kietzig, 2015).

Bird, Tsai, & Stone (2009a) proposed the following equation for splashing threshold of oblique impacts:

$$We\sqrt{Re}\left(1 - \frac{v_t k}{v_n \sqrt{Re}}\right)^2 = K \quad (20)$$

In eq. (20),  $k = \frac{1}{c}$  (21), where  $c$  is a constant relative to the radius of the lamella  $R_l$ .

$$R_l = 2c \sqrt{\frac{t v_n}{D}} \quad (22)$$

And  $t$  the time passed since the moment of the collision.

Based on the magnitude of the tangential velocity, there are three behaviors: the lamella will spread in all directions, splash in all directions, or asymmetrically splash. The sign of tangential velocity  $v_t$ , is considered to be positive for the tail of the lamella, as shown in Figure 3-6, because its direction points at the way of substrate's velocity  $v_s$ . On the other hand,  $v_t$  is negative for the front of the lamella which spreads against the motion of the substrate. As a result, two splashing thresholds occur (one for each side of the lamella) and outcomes such as two-sided splashing or one-sided splashing/spreading can be differentiated.

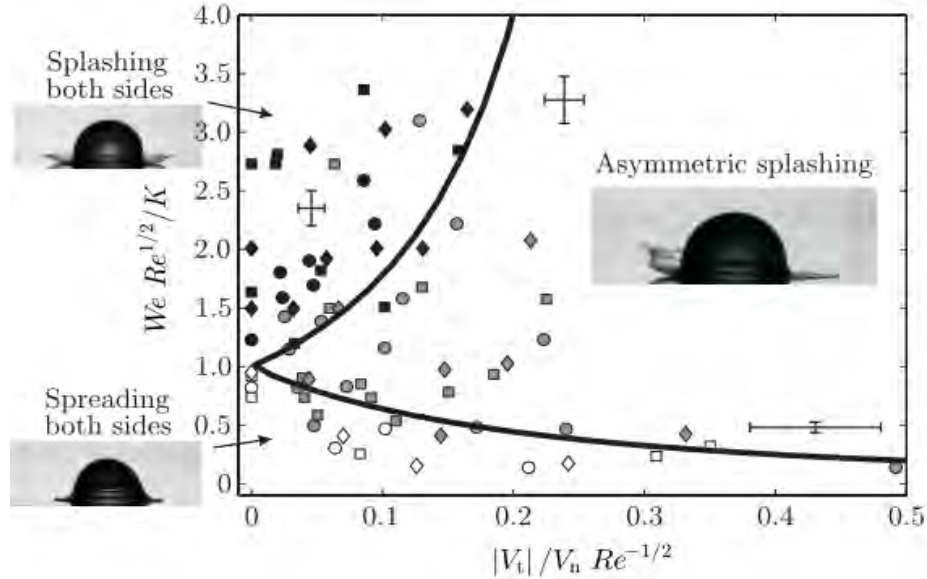


Figure 3-7: The model predicts three behaviors based on the magnitude of the tangential velocity: the lamella will spread in all directions (white symbols), splash in all directions (black symbols) or asymmetrically splash (gray symbols). Experiment with ethanol drops on to a dry, smooth, aluminum surface. Here  $K=5700$ . From Bird et al., 2009.

Chou et al. (2009) showed strong asymmetry and splashing even at low Weber numbers according to experiments on a dry rotating silicon wafer, when the impact angle to the vertical direction exceeds  $85^\circ$ . Liu et al. (2010), observed that splashing weakens as the impact angle increases, although the spreading velocity increases (in the tail/downhill direction), which should not occur according to Xu et al. (2005). Liu et al. (2010) used Kelvin-Helmholtz instability theory to explain it. K-H instability shows that splashing is attributable to the relative velocity between the spreading droplet and the surrounding gas and they concluded that the air motion caused by the falling droplet should not be neglected.

### 3.3.3 Liquid Properties

As aforementioned, except from its diameter and velocity, a droplet is described by three physical properties: liquid density, viscosity, and liquid–gas surface tension. Their role in splashing is analyzed below.

#### 3.3.3.1 Viscosity

The effect of viscous forces is typically included in Reynolds number, which defines the  $K$  value in equation  $K=We$  (23). The latter has been used to predict splashing at atmospheric conditions:

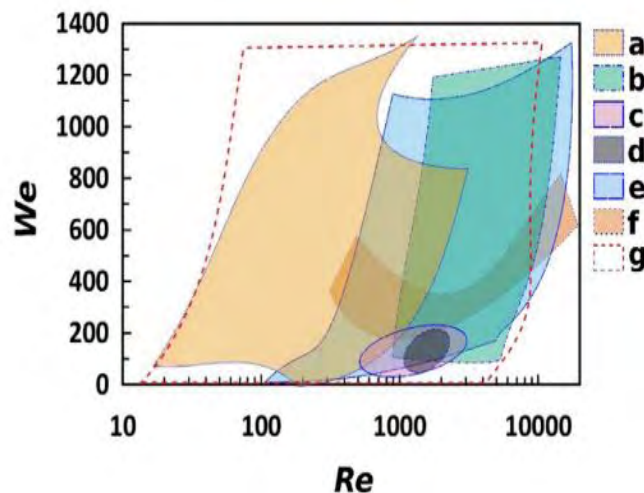
$$K = We \quad (23)$$

where  $a$  denotes the relative importance of inertia, viscous and surface forces for splashing of a drop (Moreira, Moita, & Panão, 2010; Bird et al., 2009; Mundo et al., 1995; Stow & Hadfield, 1981;

Vander Wal, Berger, & Mozes, 2006). Equation (23) predicts that splashing happens, if  $WeRe^a \geq K$ . One can find both positive and negative values for  $a$ . Negative values for  $a$ , indicate that the viscosity promotes the splashing, and a positive value means that the viscosity suppresses the splashing.

There is contradictory information on how liquid viscosity affects the splashing outcome. However, this information comes from researches which consider different ranges of Reynolds number from each other. For  $Re < 800$ , Mundo et al. (1995) found that viscosity increase sets the splashing threshold higher. Vander Wal et al. (2006), stated the opposite for Reynolds number over 2000.

For example, *Mundo et al. (1995)* reported an increase in viscosity results in a higher splashing threshold (covering the splashing-spreading boundary for systems with  $Re < 800$ ) while Vander Wal et al. (2006), concluded the splashing threshold lowers with viscosity increase covering systems with  $Re > 2000$ ). Note that the above-mentioned range for  $Re$  number are the range where splashing threshold was available in the literature, although data for  $Re > 800$  was presented, but in this range, only splashing (not spreading) data were provided.



*Figure 3-8:* The range of the  $We$  and  $Re$  numbers of various studies: (a) (Mundo et al., 1995), (b) (Vander Wal et al., 2006), (c) (Stevens, 2014), (d) (Bird et al., 2009), (e) (Palacios, Hernández, Gómez, Zanzi, & López, 2013), (f) (Riboux & Gordillo, 2014), and (g) (Almohammadi & Amirfazli, 2019). Experimental data of previous studies are not depicted in a single plot as the roughness and wettability of the surfaces differ from one study to another. From Almohammadi et al. 2019.

Recently Almohammadi & Amirfazli (2019) conducted experiments with a large range of liquid surface tensions (17-72 mN/m) and substrates surfaces of various wettabilities. They found a non-

monotonical relation of drop viscosity on splashing threshold. More specifically viscosity increase up to 5 cSt, which translates into  $Re=2000$ , promotes splashing while higher values suppress it.

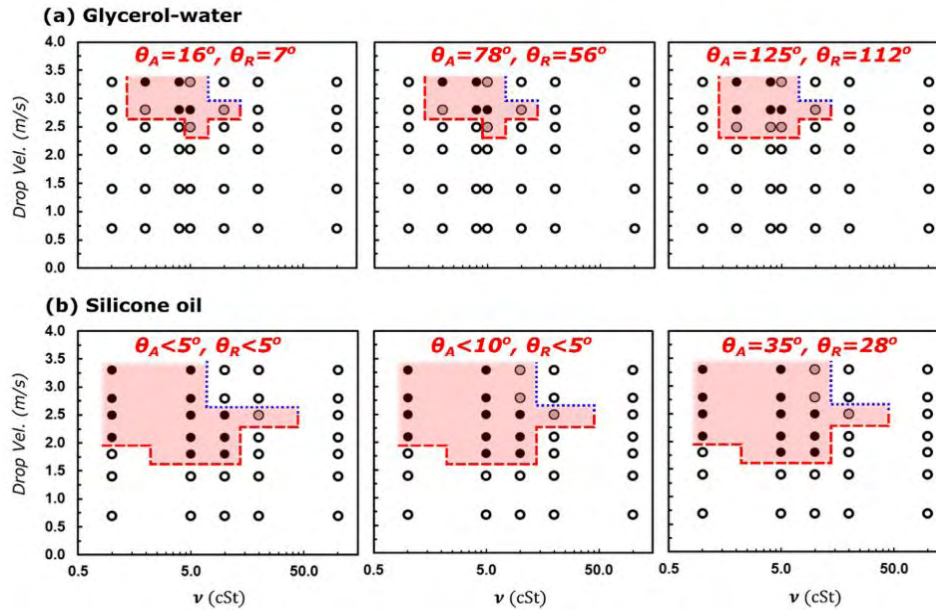


Figure 3-9: Impact outcomes for drops of (a) glycerol-water mixture (high surface tension); (b) silicone oil (low surface tension) onto surfaces with different wettabilities. Open symbols signify spreading; gray and black filled symbols denote prompt and corona splashing, respectively. The shaded region indicates the splashing regions, and the lines denote the splashing boundary to guide the eye. The maximum standard deviation for the droplet velocity is 0.08 m/s, so error bars are not shown. From Almohammadi et al. (2019).

### 3.3.3.2 Surface tension

The effect of surface tension forces on the liquid (droplet) – vapor (surrounding gas) interface are included in Weber number which compares inertial forces, which drive splashing, to surface forces that hold the droplet intact. Splashing occurs at high Weber numbers when the liquid has enough momentum to overcome surface tension forces. As the surface tension of the droplet decreases, the liquid lamella created after the impact is more likely to disintegrate (as fluid extension increases surface area and hence energy). This has been experimentally validated in various researches e.g. Range, 1998 (they also found that surface tension is relevant to the perturbations on the rim); Vander Wal et al., 2006. As surface tension between the liquid and the solid is reduced, the liquid lamella can detach from the wall, resulting in the corona splash scenario. In this case, the drop spreads and creates a crown with a thickened rim which first develops undulations along the rim and then breaks up due to surface tension (Xu et al., 2005). Comparing the results for different impingement conditions, Mundo et al. (1995) found that an increase of the surface tension led to an increase of the size of the generated droplets, and that an increase of the diameter of the primary droplets also led to an increase of the size of the splashed droplets.

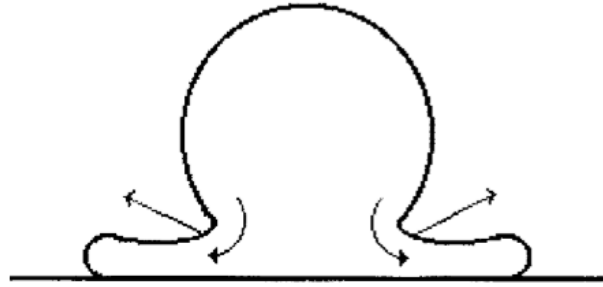


Figure 3-10: Scheme of the radial stream inside a drop during its impact on a solid wall, after Levin and Hobbs. The arrows outside the drop indicate the forces due to surface tension).

### 3.3.4 Substrate Characteristics

Splashing also depends on the characteristics of the impacted substrate such as its topography (roughness and wettability) as well as its temperature and flexibility.

#### 3.3.4.1 Surface Roughness

As very few surfaces are smooth in atomic level (with freshly cleaved mica surfaces being an exception, as shown in Figure 3-11c), several studies have been made in order to investigate the effects of surface roughness on a drop impacting a solid surface.

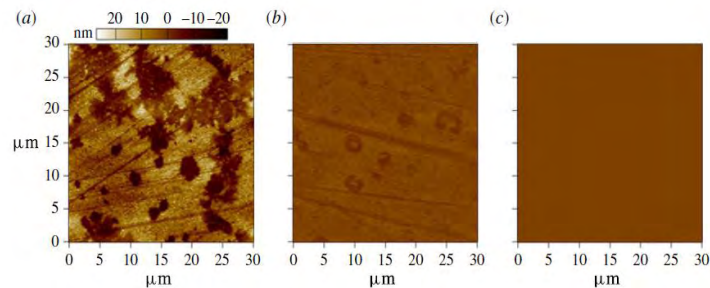


Figure 3-11: The roughness of the glass and mica surfaces: AFM topographic images of 30x30 nm regions of (a) Corning glass, (b) Fisher glass and (c) freshly cleaved mica surface. For the Corning glass, RMS=7.3 nm, max. to min. =49 nm; for the Fisher glass, RMS=1.2 nm, max. to min. =10 nm; for the mica, RMS < 0.5 nm. From Li, Vakarelski, & Thoroddsen (2015).

Generally, it is believed that surface roughness promotes prompt splashing and suppresses corona splashing.

Stow and Hadfield first made this observation in 1981, when conducting experiments with water drops on aluminum surfaces. They also were the first to provide an empirical formula for splashing threshold.

$$\xi(Ra) = Re_c^{0.31} We_c^{0.69} \approx Re_c We_c^2 \quad (24)$$

Dimensionless number  $\xi$ , the critical number for splashing, was considered as function of arithmetic roughness only. The parameters  $Re_c$ ,  $We_c$  are Reynolds and Weber numbers respectively at the critical velocity for splashing. Later Wu (1992) proposed that the weber number is a function of the radius of the falling drop to surface roughness ( $Ra$ ), for small Ohnesorge numbers, at which viscous effects are minimal, improving (24) as

$$We_c = a \log\left(\frac{R_0}{R_a}\right) \quad (25)$$

Where,  $a$  and  $b$  have different values for each combination of liquid-plate. The formula (25) was later experimentally confirmed by Range (1998). They also showed that not only surface roughness influences splash/deposition limit but different materials with similar roughness also lead to different splashing thresholds. Mundo et al. (1995) studied droplets falling on two rotating disks of different roughness and found that corona splash cannot occur when the disk roughness is in range of the droplet size. Romain Rioboo & Marengo (2001), concluded that impacts on rough substrates eventually lead to prompt splash at high velocities as this kind of disintegration occurs in the contact line region where the advancing of the lamella can be inhibited by surface roughness. Using the same explanation, Latka et al. (2012) proposed that prompt splashing is increased and corona splashing suppressed by surface roughness.

Josserand et al. (2005) showed that a splash can be triggered by a small isolated obstacle. Roisman et al. (2015), also found that the impact Weber number and the dimensionless parameter  $R_{pk}/R_{sm}$ , which represents the characteristic slope of the substrate morphology, are the primary factors influencing the splashing. They concluded that the absolute length scales of the substrate roughness don't provide sufficient information to effectively characterize the splashing threshold.

Hao (2017), made experiments with water, alcohol 16,6% ethanol droplets on solid surfaces and found that corona splashing can occur even on substrates of  $Ra=9.16\mu m$  as long as the impact velocity is high enough. They also found that water droplet impacts can result in corona splash at low surface roughness value. Further increase or decrease below that value leads to prompt splash.

### 3.3.5 Surface Wettability

Wettability is a thermodynamic property of the interface solid-liquid-vapor, defined by the  $\gamma_l g \cos\theta = \gamma_s g - \gamma_s l$  (10). It describes the ability of a liquid to spread on a solid in a surrounding gas phase and is specific for a given liquid-gas-solid system.

Despite the numerous studies which are made to determine the effect of surface wettability on splashing, results are still ambiguous. Roisman et al. (2015) as well as Latka et al. (2018), stated wettability does not influence the splashing. In other studies is reported that hydrophobic surfaces trigger drop splashing (Aboud & Kietzig, 2015; Duez, Ybert, Clanet, & Bocquet, 2007). Roisman et

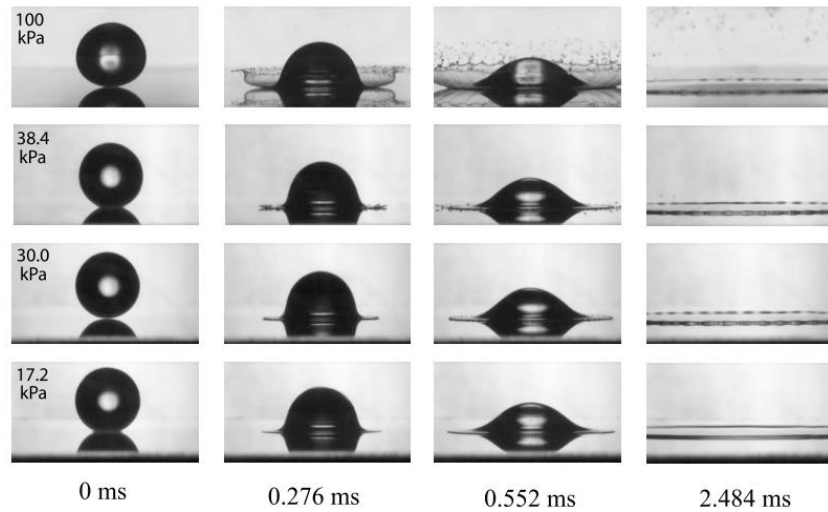


al. (2015) concluded that the splashing is independent of surface wettability. However, despite the large range of surface wettability in their experiments, the roughness of the surfaces which were used ( $R_a$  varying from 0.5 to 111  $\mu\text{m}$ ) is shown to affect the splashing according to Latka et al. (2012). ). In a numerical study of Yokoi, 2011, splashing of water droplet on a dry, flat and smooth surface, was found that a higher level of surface hydrophobicity results in a higher dynamic contact angle at the rim, which triggers prompt splashing. Aboud & Kietzig (2015), found that impact outcome is only affected (promotion of splashing) only when the substrate surface is coarse (not smooth). Moreover, Latka et al. (2018), after conducting experiments with a wettability range from 0 to 90 degrees of contact angle, concluded that for capillary numbers higher than 1, surface wettability is irrelevant to impact outcome. Finally, Almohammadi et al. (2019), stated that the splashing threshold is only affected for very high ( $112^\circ$ ) or very low ( $<5^\circ$ ) contact angle values.

### 3.3.6 Surrounding Gas Characteristics

The role of the ambient gas on drop impact had not been investigated until relatively recent years. Previous factors as drop velocity/size and fluid properties are easy to imagine that would affect the impact outcome, however the surrounding gas is a secondary yet crucial parameter. However, it is still unclear which property of gas affects splashing the most.

Xu et al. (2005) were the first to investigate its effect. At first, they noticed that an alcohol drop falling on a dry surface, at atmospheric pressure, had almost the same corona splash outcome, as a drop hitting a thin liquid layer. In the second case the corona shape is due to the liquid sheet pushing against the spreading drop, making it gain a momentum component in the vertical direction. In order that corona splash can be observed on a dry and smooth surface, there has to be another parameter putting up resistance to the lamella, urging it to lift off the surface. They used only dry smooth substrates, impacting drops of methanol, ethanol, 2-propanol and helium, air, krypton, and SF<sub>6</sub> as gasses of the surrounding atmosphere. The experiments lead to the surprising conclusion that surrounding pressure (they estimated critical suppressing pressures only for high velocity impacts) and gas composition (molecular weight) are essential for splashing to occur on a dry flat substrate. In their paper, Xu et al. gave the example of surface coating (splashing outcome is undesirable), where either a vacuum can be created or the gas can be replaced with one of a lower molecular weight.

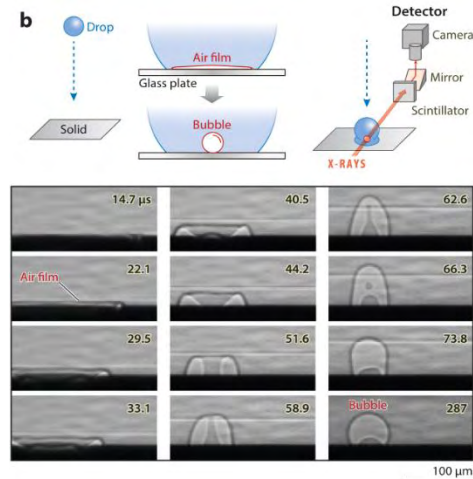


*Figure 3-12: Photographs of a liquid drop hitting a smooth dry substrate. A  $3.4 \pm 0.1$  mm diameter alcohol drop hits a smooth glass substrate at impact velocity  $V_0 = 3.74 \pm 0.02$  m/s. In the top row, with the air atmospheric pressure, the drop splashes. In the second row, with the air just slightly above the threshold pressure,  $P_T = 38.4$  kPa, the drop emits only a few droplets. In the third row, at a pressure of 30.0 kPa, no droplets are emitted and no splashing occurs. However, there is an undulation in the thickness of the rim. In the fourth row, taken at 17.2 kPa, there is no splashing and no apparent undulations in the rim of the drop. From Xu et al. (2005).*

According to Roisman et al. (2015) ambient pressure does not determine splashing for ethanol and water droplets (either when using rough or porous surfaces). Furthermore, Guo et al., (2016) suggested that the gas density is the factor which determines the splashing outcome rather than the gas pressure. In another research by Jian et al. (2018), has been proposed that splashing behavior is affected by the gas viscosity with a small contribution from the gas density. Recently, experiments conducted with droplets impacting on a smooth dry glass surface at high velocities (high  $We$ ,  $Re$  numbers), showed that the surrounding gas is relevant only for predicting the number of secondary droplets and their ejection angle (Burzynski & Bansmer, 2019).

### 3.3.7 Air Entrapment

Under atmospheric conditions, a drop impacting perpendicularly to a surface will always entrap a small amount of air under its center. As the droplet approaches the substrate, the gas between them has to be expelled and its density and viscosity determine how rapidly this occurs (Mandre, Mani, & Brenner, 2009; Mani, Mandre, & Brenner, 2010). Just before this happens, the lubrication pressure in the thin air layer due to the gas viscosity becomes strong enough to create a dimple in the spherical drop. Then the dimple contracts rapidly into a central bubble on the substrate, to minimize its surface energy. This phenomenon was first observed in snapshot photographs of Chandra & Avedisian (1991) and later Thoroddsen et al. (2003) used high-speed video to directly observe the initial air disk and its contraction.



**Figure 3-13:** X-ray imaging setup for the entrapment of an air disc and its contraction into an air bubble, with a subsatellite pinched off at its center (Lee et al.2012).

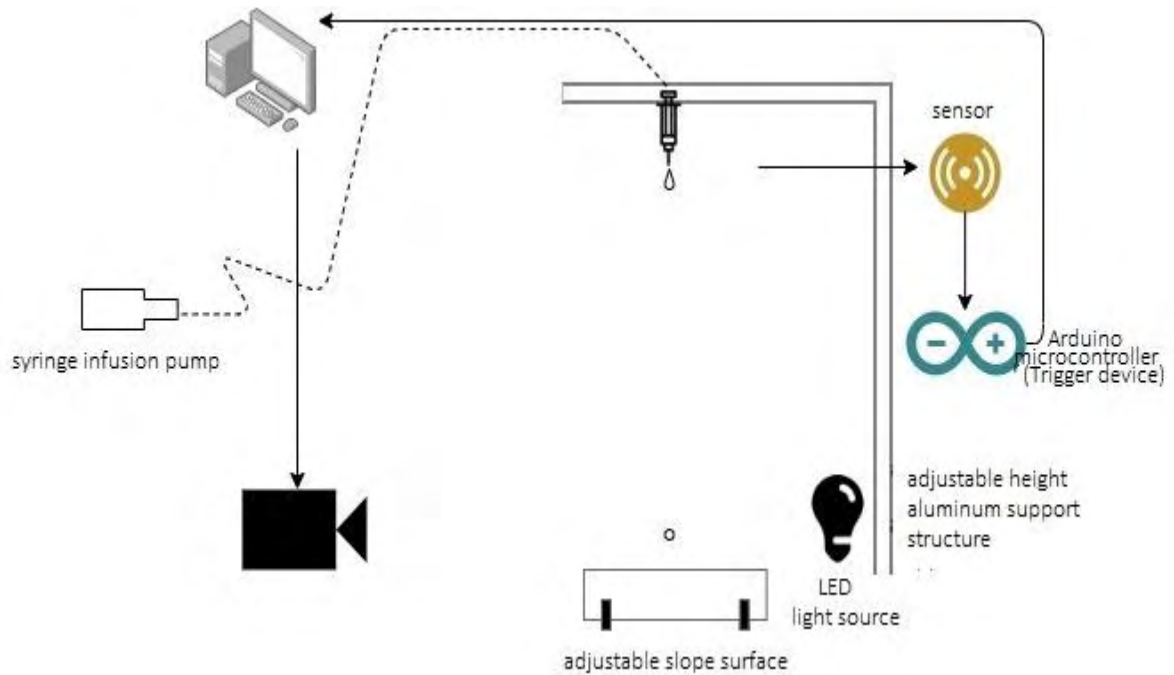
Mandre, Mani, & Brenner (2009) theoretically demonstrated neglecting intermolecular forces between the liquid and the solid, the liquid does not contact the solid, and instead spreads on a very thin air film. With regards to splashing, their computations did not show any indication of splashing and therefore other physical effects (as viscosity of the drop liquid, mean-free path of the gas, and thermal and mass transfer, which were not included) should be taken into consideration to obtain such behavior. However, Driscoll & Nagel (2011) during their experiments ( $\mu$  varying from 8 to 48 MPa\*s), found no trapped air beneath the spreading drop outside the small central bubble and suggested that at the responsible for destabilizing the liquid is the gas flow edge of the spreading drop. This conclusion is consistent with splash experiments in the low-viscosity regime (Xu et al., 2005). Burzynski & Bansmer (2019) conducted experiments with water droplets impacting on smooth glass surfaces, surrounded by different gases at ambient pressure and concluded that gas entrapment is not responsible for splashing at high Reynolds and Weber numbers ( $We \approx 4800$ ,  $Re \approx 35\ 000$ ).

### 3.4 Thesis Aim and Objectives

The present thesis focuses on the outcomes of droplet collision onto a dry solid surface. More specifically the intention is to investigate the regimes of impact, especially deposition and splashing, in relation with the impacting surface properties. Moreover an attempt to define a representative splashing threshold is made. The experiments are conducted using distilled water-methanol mixtures, of differing concentrations, as the impinging liquid in order to evaluate the phenomenon for various values of viscosity, density and surface tension. The solid substrate is placed horizontally and inclined with respect to the x-axis, so as to research the way that different inclinations affect the impact. The experiment is then repeated for a solid substrate of different roughness as a means of including the effect of surface roughness in the investigation. Furthermore the generated drops fall from different heights resulting to different Weber numbers for each height. The parameter of height is inserted in the experiment, in order to achieve an altering impact velocity and thus different impact dynamics. The methods, the results and the conclusions of the thesis are extensively presented in the following chapters.

## 4 Methods

In order to study the outcome of water drops impacting on solid surfaces, we had to design an appropriate experimental configuration in the university's laboratory. The apparatus (*Figure 4-1*) consists of a syringe infusion pump, an aluminum support structure, a CCD camera, an LED DC battery light, a light diffusion milky colored tile, an adjustable slope base, two solid substrates of different roughness and an Arduino microcontroller-motion sensor system. In general, the experimental procedure can be described as follows: the syringe pump is turned on pushing the liquid in the tube until drops start to fall from the orifice of the pipe which is installed on the top of the aluminum structure. These drops before impacting with the substrate, travel through the motion sensor which is connected to the Arduino microcontroller. Then the trigger is sent the computer and after that to the camera which eventually captures the collision. The contribution of the components is further analyzed in the following sections.



*Figure 4-1: Diagram of the experimental apparatus.*

### 4.1 Experimental Setup

### 4.1.1 Support Structure

The aluminum frame composed of Bosch Rexroth 45x45 rectangular profiles bolted on each other which provided solid support for the peripheral parts. The contraption could move in all x-y-z directions, thus providing versatility. The plastic tube from which the liquid was infused, was stabilized by a 3D printed base mounted on a horizontal strut of the frame. The light source and the Arduino console were also fixed on the aluminum frame; however we had the ability to adjust their position horizontally or vertically as shown in Figure 4-2.



**Figure 4-2: Drop impact aluminum support structure.**

### 4.1.2 Arduino

In order to image the drop impact on the solid substrate at any desired moment of their interaction an ARDUINO UNO REV3 microcontroller (circuit board) was used. A 16x2 LCD Keypad module was connected on the board and the device could function as a digital delay pulse generator. The microcontroller was adjusted on a specific time value (capturing delay) that was given within microsecond ( $\mu\text{sec}$ ) accuracy for reasons of better temporal depiction of the phenomenon (**Figure 4-3**). The Arduino was connected with a LTH-301-32 photo interrupter, via a pin connector. The photo-sensor was stabilized on the same 3D printed base with the plastic pipe, right below the point from which the liquid exited (**Figure 4-4**). Photo-interrupters are transmission type photo-sensors and consist of a light emitting and a light receiving element placed facing each other. When the target object i.e. drop comes between those elements the device detects the blockage

of the emitted light, acting as an optical (non-contact) switch. This moment was perceived as time zero during the capturing process. The microcontroller sent signal to the CCD camera to capture a snapshot of the interaction. The capturing delay was the one previously set on the microcontroller in  $\mu\text{sec}$  after time zero. The integration of these devices aided to the procedure of collecting valuable experimental data at known moments of the phenomenon and comparing the temporal evolution when altering the experiment parameters.



Figure 4-3: The Arduino microcontroller-LCD Keypad system showing regulating the wanted capturing delay.



Figure 4-4: Droplets crossing the photo interrupter (black).

### 4.1.3 Liquids

Initially distilled water was used in the experiment, for the avoidance of mineral depositions inside the syringe, the pipe and on the solid substrate. It was supplied via a deionizing column which is installed in the lab (Figure 4-6).



Figure 4-5: The deionizing column.

Later, we decided to include methanol-water(distilled) solutions in the experiment to study the impact of viscosity and surface tension on the splashing. Due to the fact that the liquid properties

do not change linearly with the % w/w proportion of methanol in the mixture (Figure 4-6), we used 6 different solutions of water-methanol in total (0%, 20%, 40%, 60%, 80%, 100%) to achieve proper comparison of the results.

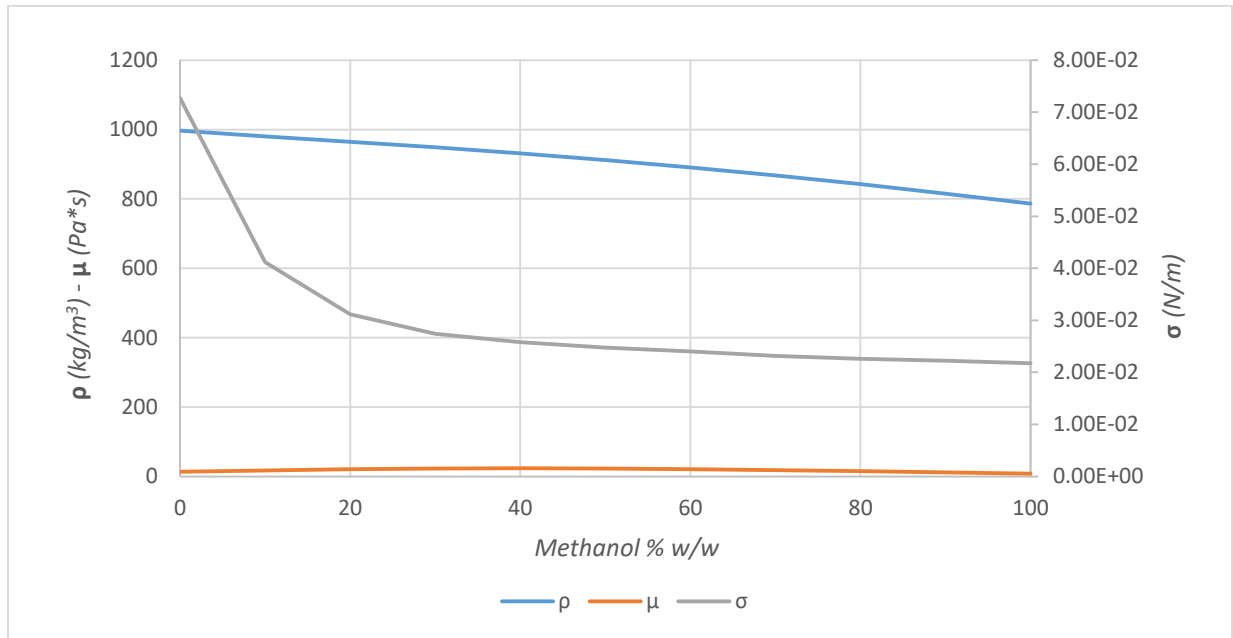


Figure 4-6: Liquid Properties of different % w/w water-methanol solutions. Data taken from 'Densities and Viscosities of Methanol-Water Mixtures' S.Z. MIKHAIL and W.R. KIMEL.

## 4.1.4 Droplets

### 4.1.4.1 Droplet Generation Procedure

Droplet flow was generated from the syringe pump. The Cole-Parmer single syringe infusion pump is a device that regulates a steady liquid flow rate outside of the syringe. A 10mL 21G X 1 1/2" syringe was chosen for the experiment. The full syringe was clamped on the pump device and a piston pushed the liquid outwards at a predetermined flow rate (**Figure 4-7**). The steady flow is of paramount importance, in order to have a relatively stable (accuracy: < 1% error on the selected flow rate) time interval between the successive drops. The desired interval had to be long enough for the manual cleaning of the solid substrate before the impact of the following drop, whereas the flow rate had to be small enough in order for the drops to form and detach under their own weight's effect and avoid jetting behavior of the liquid. According to these specifications an appropriate flow rate was selected for the experiment. The liquid drops detached from the orifice of a plastic pipe that was connected with the syringe. The droplet diameter during the fall was considered separately for each liquid mixture, due to the altering values of the physical parameters involved. By selecting distilled water as a component of the liquid, the avoidance of mineral



depositions inside the syringe, the pipe and on the solid substrate, was achieved. Distilled water was supplied via a deionizing column which is installed in the lab (*Figure 4-8*).



*Figure 4-7: The syringe pump*



*Figure 4-8: The deionizing column.*

Regarding the aluminum support structure, the movement on the vertical  $y$ -axis aimed at the investigation of the impingement phenomenon for a range of different Weber numbers. In that way the impact velocity could change by altering the height of fall. However, there is a critical height for free fall, over which the velocity takes a final and maximum value, known as the terminal velocity. Upon reaching this height there is no point to further increase it, because the outcome of the impact doesn't alter. The calculation of terminal velocity and critical height follow. Assuming an object that is under free fall inside earth's gravitational field, there are two forces that act upon it. The one is the gravitational pull  $W$  from earth's mass that acts in the direction of earth's core. The other is the drag force  $D$  that acts against  $W$  and decelerates the object (*Figure 4-9*). Buoyancy is considered to be insignificant.



*Figure 4-9: Forces acting on a free-falling drop under air resistance effects.*

The gravitational pull is described by the equation:  $W = mg$  (26), where  $m$  is the mass of the object and  $g$  is the gravitational acceleration. Inside earth's gravitational field  $g = 9.81 \text{ m/s}^2$ . In the case of a drop and assuming a nearly spherical shape, mass can be expressed as  $\rho V$  i.e. the product of the density and the volume of the drop. The density of distilled water at atmospheric pressure conditions (25 °C) is  $997.5 \text{ kg/m}^3$ . The drop's volume is expressed as:

$$V = \frac{4\pi r^3}{3} \quad (27)$$

, assuming that the droplet can be approximated as a solid sphere. The drag force appearing on our experiment concerns Reynolds numbers above 0.1 and is thus described by the quadratic drag equation:

$$D = \frac{C_D \rho_a A U^2}{2} \quad (28)$$

In relation  $D = \frac{C_D \rho_a A U^2}{2}$  (28) drag is proportional to the surrounding air density  $\rho_a$  whose value at atmospheric conditions is  $1.2 \text{ kg/m}^3$ , the cross sectional area  $A$  ( $\pi r^2$  for a sphere), the square of the instant velocity  $U$  and the drag coefficient  $C_D$  (0.47 for solid spherical objects), for Re numbers between 2000 and 200000, which for our drops corresponds to velocities between 6 m/s and 602 m/s.

Applying Newton's second law of motion to the free-falling drop for the constant terminal velocity  $V$ , the acceleration is zero. As a result, the ensuing relation is in effect.

$$mg = \frac{C_D \rho_a A U^2}{2} \rightarrow U = \sqrt{\frac{2mg}{C_D \rho_a A}} \quad (29)$$

Replacing the parameters of (29) with their known values, the result for the terminal velocity of the drop is **10.75 m/s**.

In order to determine the minimum height above which the droplet reaches terminal velocity  $V$ , the free fall equations (for zero initial velocity) are applied. These are the following.

$$U = gt \quad (30)$$

$$h = 1/2gt^2 \quad (31)$$

Relation  $U=gt$  (30) gives a time of **1.095 s** until the system reaches terminal  $V$ . Replacing in (31) the critical height derived is **5.88 m**. Thus, the setup of our experiment, is capable of providing different  $We$  numbers in the whole range of its heights ( $h_{max} = 1 \text{ m}$ ).

#### 4.1.4.2 Temporal discrepancies

A problem faced during the early stages of the experiment was the fact of taking impact results for time values, lower than those of free fall from the same height (**Figure 4-10**). The discrepancy

was present for all heights selected. From an aerodynamic aspect these results were rejected. The deviation varies from 31.07ms to 39.93ms, with an average deviation value of 35.29ms as shown in Table 4.1.

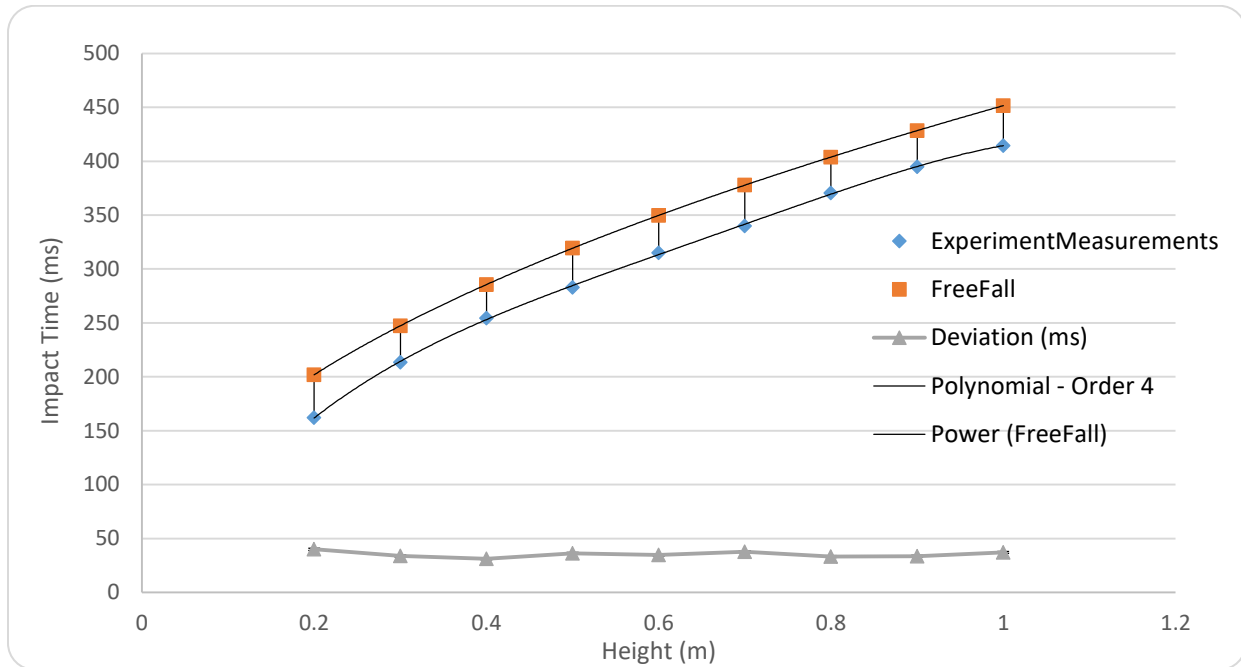


Figure 4-10: Graph depiction of the time values of set delay (blue dots) and free-fall (orange dots).

Height(m)	T <sub>impact</sub> (ms)	H-FreeFall (m)	T-FreeFall (ms)	Deviation (ms)
0.2	162.00	0.13	202	39.93
0.3	213.50	0.22	247	33.81
0.4	254.50	0.32	286	31.07
0.5	283.00	0.39	319	36.28
0.6	315.00	0.49	350	34.75
0.7	340.00	0.57	378	37.77
0.8	370.50	0.67	404	33.36
0.9	394.70	0.76	428	33.65
1	414.50	0.84	452	37.02
			<b>Average:</b>	<b>35.29</b>

Table 4.1: For each height value is shown the Arduino set delay (Time Impact, 2nd column), the height calculated for free-fall corresponding to this time value (3rd column), the calculated time of free-fall for this height (4th column) and the deviation between the 2<sup>nd</sup> and 3<sup>rd</sup> columns

At first a possible time delay on the process of signal sending between the microcontroller, the PC and the CCD camera was assumed. In other words, the actual time of impact was speculated to be the sum of the time set on the microcontroller and this signal delay time. Thus, a mathematical approach, based on the 2<sup>nd</sup> law of Newton was investigated, to confirm or reject this possibility.

The time results of this approach confirmed the experimental ones. As a result, the inaccuracy was not due to a signal delay. Afterwards the possibility of false calculation for the free fall time was investigated. The initial calculation was made considering a free fall with zero initial velocity. However, the drop detached from the lip of the syringe about 1 to 1.5 cm above the photo-

A) Before the photointerrupter (Free fall, zero initial Vo)			B) Free fall with initial Vo after the detection						
Assumed h(m)	Time (s)	V (m/s)	Time of impact for height h:	to.6	to.7	to.8	to.9	t1	
0.01	0.045	0.443		0.308	0.335	0.361	0.386	0.409	
0.011	0.047	0.465		0.306	0.333	0.359	0.384	0.407	
0.012	0.049	0.485		0.304	0.332	0.358	0.382	0.405	
0.013	0.051	0.505		0.302	0.330	0.356	0.380	0.403	
0.014	0.053	0.524		0.300	0.328	0.354	0.378	0.401	
0.015	0.055	0.542		0.299	0.327	0.352	0.377	0.400	
				Impact time from experiments	0.315	0.342	0.369	0.393	0.42
<b>The velocities V from calculation A are used as initial velocities Vo for calculation B</b>									

**Table 4.2: Calculation of impact time for a free-falling drop with initial velocity. Comparison of these values with the experimental ones.**

interrupter. This distance greatly altered the free fall phenomenon, because the photo-interrupter identified a drop with initial velocity. The calculations for a theoretical free fall with initial velocity are the ensuing:

From Table 4.2 it is obvious that a drop with initial velocity in the range of 0.44 and 0.54 m/s, in free fall without air resistance effects, impacts on the solid substrate various milliseconds before the time values taken from the experimental investigation. This time deviation confirms the decelerating effect of drag on a falling object.

#### 4.1.4.3 Calculation of droplet's diameter

The usage of six different liquid mixtures, each having its own physical properties, during the experimental procedure, meant that the droplet size would vary between the mixtures. The diameter of the droplet for each mixture was firstly measured experimentally during the image processing procedure. Consequently a mathematical equation to confirm these results was researched. Three distinctive equations were compared with the experimental values. The first one was based on the Rayleigh-Plateau instability of liquid jets (Ashgriz, 2011) and given by the type  $\lambda = \pi\sqrt{2} D_{RP}\sqrt{(1 + 30h)}$  (32), where  $\lambda$  stands for the critical wavelength that leads to jet breakup into droplets (in our case the length of the exit nozzle from the tube) and  $D_{RP}$  stands for the diameter calculated by relation (32). The second equation was based on a balance between the gravitational force pulling the drop downwards and the surface tension holding the drop attached to the tip of the nozzle,  $(\rho_{liq}\pi D_T^3 g)/6 = \pi D_{nozzle}\sigma$  (33), known as Tate's law (Tate, 1864), where  $D_T$  stands for the diameter calculated by relation (33). The third equation  $G = 3,6\Phi^{2,81}$  (34), derived through dimensional analysis (Yildirim et al., 2005) and  $G$  stands for the dimensionless Bond number, while  $\Phi = R_{nozzle}/V^{1/3}$ . The results from the three relations are

given in Table 4.3. It is clear that relation's (32) values don't conform to the experimental ones. Relation (33) gives a pretty accurate approximation but overestimates the droplet diameter,

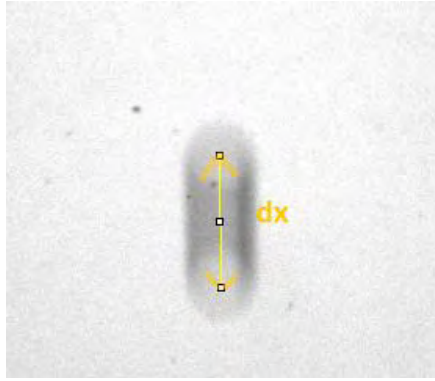
Methanol % w/w	Experimental Diameter(mm)	R-P Diameter(mm)	Tate's Diameter(mm)	Yildirim's Diameter(mm)
0	4.5	1.4	5.1	4.5
20	4	1.4	4.5	3.9
40	3.7	1.4	4.1	3.6
60	3.5	1.4	3.9	3.4
80	3.2	1.4	3.8	3.3
100	3.2	1.4	3.7	3.2

**Table 4.3: Values of diameter measured in the experiment and values of the diameter from Rayleigh-Plateau's instability, Tate's Law and Yildirim's dimensional analysis.**

different from those of the experimental measurement.

#### 4.1.4.4 Calculation of dimensionless numbers

The measurement of droplet velocity upon impact for several heights of the experiment was achieved by increasing the CCD camera exposure time. This increase should be cautious in order to avoid a possible damage of the CCD due to excessive exposure to the illumination source. In that way the shutter speed was reduced, as we needed more light in the photographs, and the camera was not still able to momentarily capture the drop. Using an exposure time of 2 milliseconds the droplet images taken during the fall appeared blurred. The blurriness was attributed to the movement of the droplet during this small time interval. The images showed deformed elongated droplets. On each image the drop appeared as a prolate spheroid due its downward motion. The pictures were then processed at ImageJ. The distance  $dx$  covered by the drop in 2 milliseconds was measured as the distance between the center of the drop at the upper and lower positions (*Figure 4-11*). The very short time interval of 2 milliseconds allowed the consideration of linear motion within these time limits. Therefore, dividing  $dx$  with the given exposure time  $dt$ , the local velocity was found. The process was repeated for several images in order to find the mean velocity for each height, indicative shown (*Table 4.4*) for the pure distilled water case. Moreover the distance  $H_r$  between the prolate spheroids lower point and the solid substrate was deducted from the overall distance. In that way the height of fall responding to each velocity was measured.



Height(m)	Uexposure(m/s)
0,49	2,61
0,59	2,87
0,69	3,19
0,79	3,52
0,89	3,84
0,99	3,96

Figure 4-11: Image capture with exposure at 2000  $\mu$ s. Table 4.4: Measurement of impact velocities for pure water.

After measuring the impact velocity for several heights, all the pertinent parameters for calculation of the dimensionless numbers were known. In order to obtain the appropriate values for the physical properties (density, surface tension and dynamic viscosity) of each liquid mixture, experimental conditions of 20 degrees Celsius at atmospheric pressure of 101.3 kPa were assumed for the pure water case, while conditions of 30 degrees Celsius at 101.3 kPa for the other cases, due to different temperature conditions in the lab during the experiment. The calculations resulted in the ensuing Weber and Reynolds numbers (**Table 4.5**) for the various water-methanol mixtures.

Weber numbers ( $\rho d u^2 / \sigma$ )		Methanol % w/w					
		0	20	40	60	80	100
Height(cm)	0,29	-	-	547	468	555	-
	0,39	-	-	673	706	705	-
	0,49	-	-	736	825	782	-
	0,59	-	-	883	889	940	-
	0,69	-	-	1008	967	994	-
	0,79	766	986	1233	1125	1183	1226
	0,89	909	1125	1391	1295	1322	1352
	0,99	971	1197	1463	1431	1449	1491
Reynolds numbers ( $\rho d u / \mu$ )		Methanol % w/w					
		0	20	40	60	80	100
Height(cm)	0,29	-	-	5945	5269	6736	-
	0,39	-	-	6597	6472	7587	-
	0,49	-	-	6898	6996	7995	-
	0,59	-	-	7555	7261	8764	-
	0,69	-	-	8072	7575	9013	-
	0,79	15840	11020	8931	8168	9832	16207
	0,89	17261	11771	9483	8767	10391	17021
	0,99	17839	12141	9727	9216	10878	17870

Table 4.5: a) Weber and b) Reynolds numbers for the liquid mixtures of the experiment

## 4.1.5 Camera

The camera used was a TSI Powerview plus HS-200 which is an iter frame CCD camera. It has a 2048x2048 pixels resolution and a 12-bit intensity dynamic range. It was placed on a tripod, across the experimental setup, which gave us the ability to adjust the position of the camera (e.g. height, angle). A SIGMA 70-200mm F.2.8 APO, fixed focal length lens was adapted on it. The program used for controlling the camera in the computer is insight 3G. Via this program the immediate review of images and adjustment of camera settings, like exposure, if needed, were feasible. More importantly it allowed the use of the trigger provided by the Arduino to capture the impact at specific times, during droplet impact.



Figure 4-12: TSI Powerview plus HS-200.



Figure 4-13: SIGMA 70-200mm F.2.8 APO zoom lens.

## 4.1.6 Illumination

The illumination source used was a Dekton XW 750 LED light. By using this direct current light, the flickering phenomenon is avoided and thus the images have a good quality. For the sake of lightning uniformity on the image and camera lens protection a light diffusion tile (Plexiglas) was placed between the LED and the camera. Both the light source and the diffusive tile were attached on the aluminum frame.





Figure 4-14: Illumination source.

### 4.1.7 Substrates

The substrates used for the experiment were made of aluminum alloy which is soft and easily formable compared to other metals like steel. This enabled the formation of square substrates with dimensions 5cm×5cm×1cm simply by using a handsaw. Then, in order to roughen the aluminum surface, sandpaper P24 was utilized, with average grain diameter 764μm.




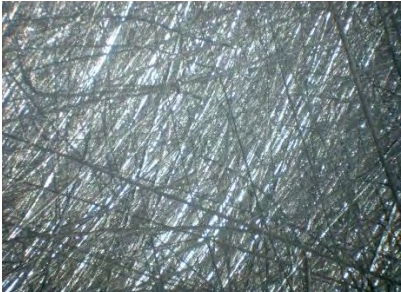
	Smooth Substrate	Substrate made with P24 Grit
Estimated Ra	0.45μm	4.3μm
Camera Images		
Images from stereoscope		

Table 4.6: Resulting surface roughness.



Aluminum is also very resistant against various forms of corrosion, due to its chemical affinity with oxygen. It generates a layer of aluminum oxide, which is a very effective way of preventing further corrosion. As a result, experiments with water droplets did not affect the substrate surfaces.

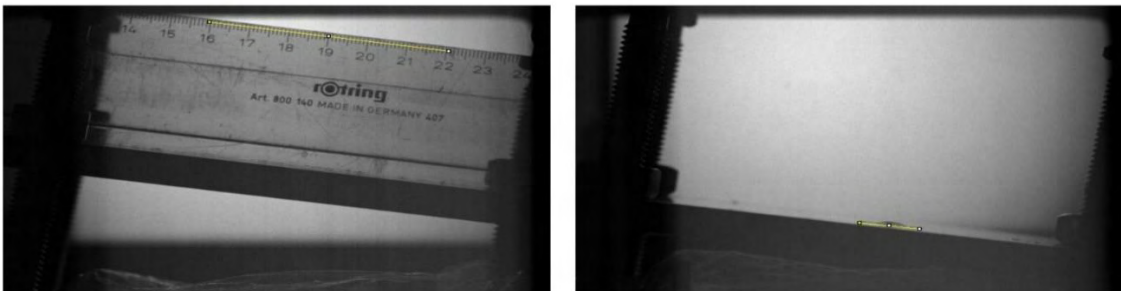
The substrates were placed on a small metal base with three threaded legs, allowing the adjustment of impact angle by screwing or unscrewing them as shown in Figure 4-15.



**Figure 4-15: Metal base for adjusting impact angle.**

## 4.2 Image Processing

Upon completion of the experimental stage, the collected images were processed in order for the data to become ready for interpretation. For this procedure the processing software ImageJ was selected. At the beginning of each batch of experimental measurements a ruler was placed on the solid substrate. The image containing the ruler was used for scaling purposes. A known distance between points of the ruler was selected and given in millimeters (mm) as shown in Figure 4-16. This distance was the equivalent of a number of pixels on the image. Hence an analogy between pixels and mm was saved i.e. number of pixels responding to 1 mm. According to this analogy a stable scale was set for the image batch and on each image the number of pixels selected were automatically converted to millimeters.



**Figure 4-16: Images processed at ImageJ a) Ruler distance selected in order to set a stable scale, b) Measured drop diameter in pixels after the impact. Converted to mm distance after scaling comparison with a.**

## 5 Results and Discussion

Experiments with the aforementioned solutions of water-methanol led to three different results as shown in the pictures below. The first one was simple deposition of the droplet which was the main occurrence when distilled water (0% w/w solution) and pure methanol (100% w/w methanol) were used. The most frequent result was prompt splash especially during impacts on the roughened substrate. However due to the small size of the emerging droplets and the narrow camera focus it was difficult to always determine with certainty their presence. For this reason, in the thesis the occurrence of prompt splash is noted only when the clarity of the photographs allows it. Then there was corona type of splash, where the lamella lifts off the substrate into a bowl-like shape and prompt splash, where tiny droplets emerge from the advancing lamella while it spreads on the substrate.

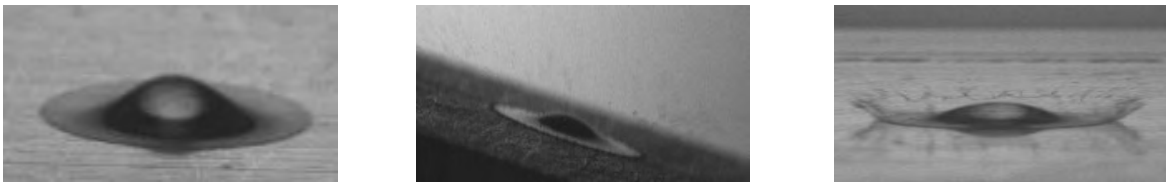


Figure 5-1: (a) deposition (100% solution on smooth flat substrate, drop falling from 88cm,  $u=3.449$  m/s,  $We=1352.28$ ), (b) prompt splash (20% solution on P24 substrate tilted by 10 degrees, drop falling from 99cm,  $u= 3.802$  m/s,  $We= 1197.20$ ), (c) corona splash (60% solution on smooth flat substrate, drop falling from 99cm,  $u=3.678$  m/s,  $We=1431.38$ ).

### 5.1 Vander Wals Criterion for Splashing on Flat Surfaces

In order to find a threshold for the splashing/non splashing (either prompt or corona) boundary on flat surfaces, several algebraic relations based on relations between the dimensionless numbers were tested. The relation that was found to be pertinent with the experimental results is  $OhRe^{0.609} = 0.85$  (18). A relation that was extracted after testing several liquids (Vander Wal et al., 2006) . The data of the experiment were plotted for splashing/non splashing impact conditions (Figure 5-2). The curved black line corresponds to the algebraic threshold. Each symbol shape represents a specific mixture of distilled water and methanol, indicated at the legend of the chart. The red points indicate an expected splashing event according to the experimental data, while the blue points indicate an expected non-splashing event. From an algebraic perspective, points above the curved line represent a splashing event, while points below the curved line represent non-splashing.

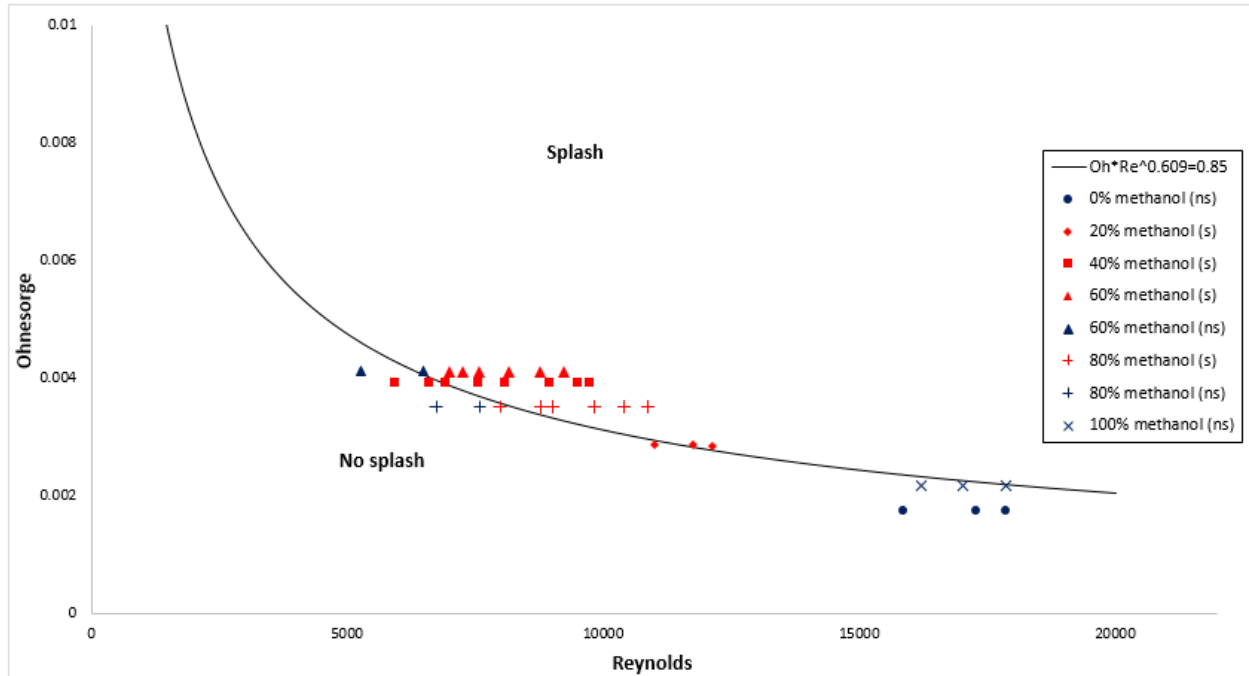


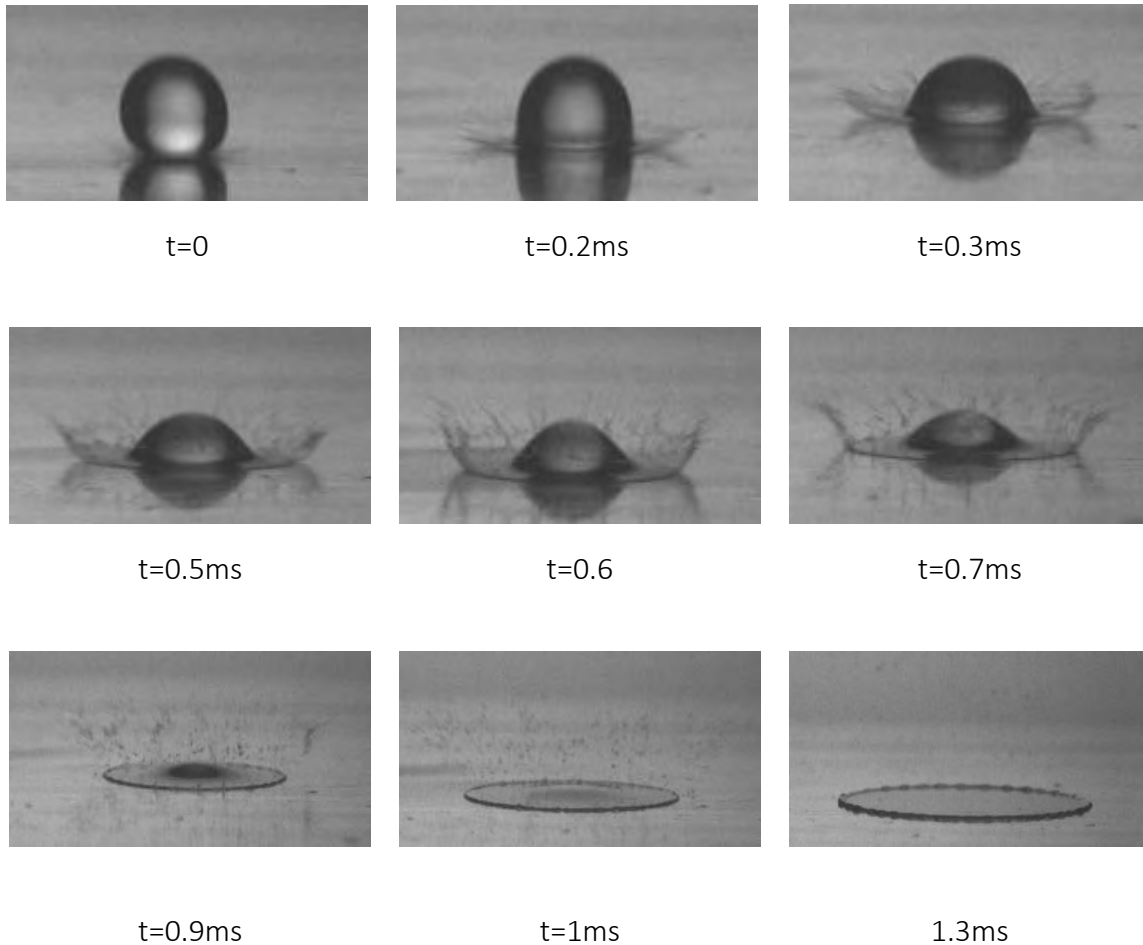
Figure 5-2: Splash behavior of several mixtures of distilled water-methanol, plotted with respect to the dimensionless Reynolds and Ohnesorge numbers. The equation for the border fit line is included on the graph.

The figure shows that the placement for the wide majority of points confirms the experiment and the algebraic relation fits the observed regime accurately. A discrepancy concerning 5 out of the 33 points can be attributed to a small experimental uncertainties. One can observe that as the value of the Ohnesorge number grows, the range of the splashing event tends to grow. For the mixtures of 40%, 60% and 80% methanol w/w, that present the highest Oh numbers, we observe a splashing regime for lower heights in comparison with the other mixtures. Therefore, high ratios between viscosity and surface tension act to promote splashing.

## 5.2 Corona Splash

### 5.2.1 Formation and Disintegration

In all the experiments corona formation emerged and disintegrates in the first 1-1.5 ms counting from the moment the droplet contacts the solid surface ( $t=0$ ). In the beginning (when the impact velocity is high enough for corona splashing) a thin liquid layer lifts off the substrate into a bowl like shape. Then as a bigger part of the droplet liquid volume starts to spread on the surface, corona shape is created and small droplets are expelled radially till it collapses entirely.



**Figure 5-3: Splashing of 40% water-methanol solution, impacting on the smooth substrate from 100cm height.**

Figure 5.3 shows the process of the corona creation from the time it touches the substrate till its breakup and the further advancing of the lamella which follows.

### 5.2.2 Splashing Angles

The ensuing diagrams present how the liquids physical properties and the kinematic conditions affect the impact. Each diagram contains the right and left side angle measurements for the three liquid water-methanol mixtures (40%, 60% and 80% w/w methanol) that provide a corona splash regime. The investigated parameters are presented for the smoothest substrate ( $R_a=0.45\mu\text{m}$ ) placed horizontally and on inclination of  $10^\circ$ ,  $20^\circ$  and  $30^\circ$  with respect to the x-axis. Figure 5-4-Figure 5-7 concern droplet impingement from a fall height of 0.99 m, Figure 5-8-Figure 5-11 from a height of 0.89 m and Figure 5-12-Figure 5-15 from a height of 0.79 m and thus the different Weber numbers for each batch of Figures.

In **Figure 5-4** the parameters are presented for a horizontally placed substrate and a height of 0.99cm. A tendency of the angle on both sides of the droplet to increase with the diameter of the

droplet and thus with time is observed. The right angle of the 80% mixture presents the highest values during the regime, while the right angle of the 40% mixture presents a sudden drop in the angle value during the splashing regime, followed by steep increase to its highest value, before collapsing (referred from now on as tick phenomenon). The initial decreasing behavior can be attributed to the formation of the bowl shaped corona and the increase afterwards to the final stages before the disintegration of the crown, when the lower part of it has already collapsed and only the higher more inclined parts remain detached from the substrate. A tick is also observed for the same mixture at the upslope side of the crown, while for the 80% mixture we observe an initial increase on the angle between  $1.75$  and  $2D_{ND}$  followed by retention of a steady value before collapse. It is also obvious that the splashing regime presents a pretty accurate symmetry between the two sides of the crown. The corona collapse occurs between  $2.5$  and  $3D_{ND}$  for all the mixtures.

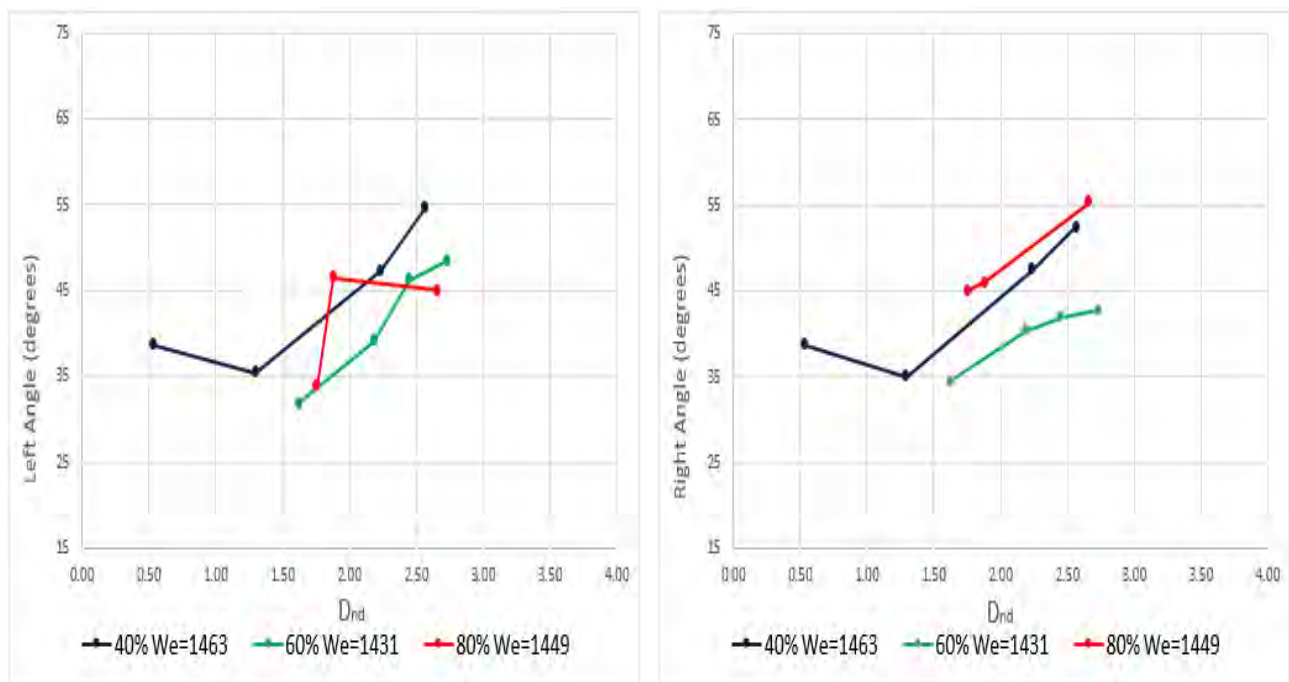


Figure 5-4: Crown angles on the left and right side for horizontal substrate,  $H=0.99m$

Figure 5-5 concerns both side angles for substrate inclination of  $10^\circ$ . The angles on the left (upslope) side present a constant increase, while on the right side the values present fluctuation. The lifetime of the crown appears the greatest on both sides for the 40% mixture which has the greatest Weber number (1463). The crown presents asymmetric behavior between the two sides for all the mixtures. In the 40% both side angles increase until the crown base reaches  $2,2D_{ND}$  when they obtain a value of about 45 degrees but afterwards the left side angle keeps increasing while the right-angle value decreases, before collapsing. It is clear that the 80% mixture presents higher angle values on the right side than on the left one. Similar to Figure 5.4 these values are also the highest between all the mixtures. Moreover, the lifetime of the crown is greater on the

right side where it collapses at about  $3D_{ND}$ . The right-side angle follows the tick phenomenon while the left side follows a straightforward increase.

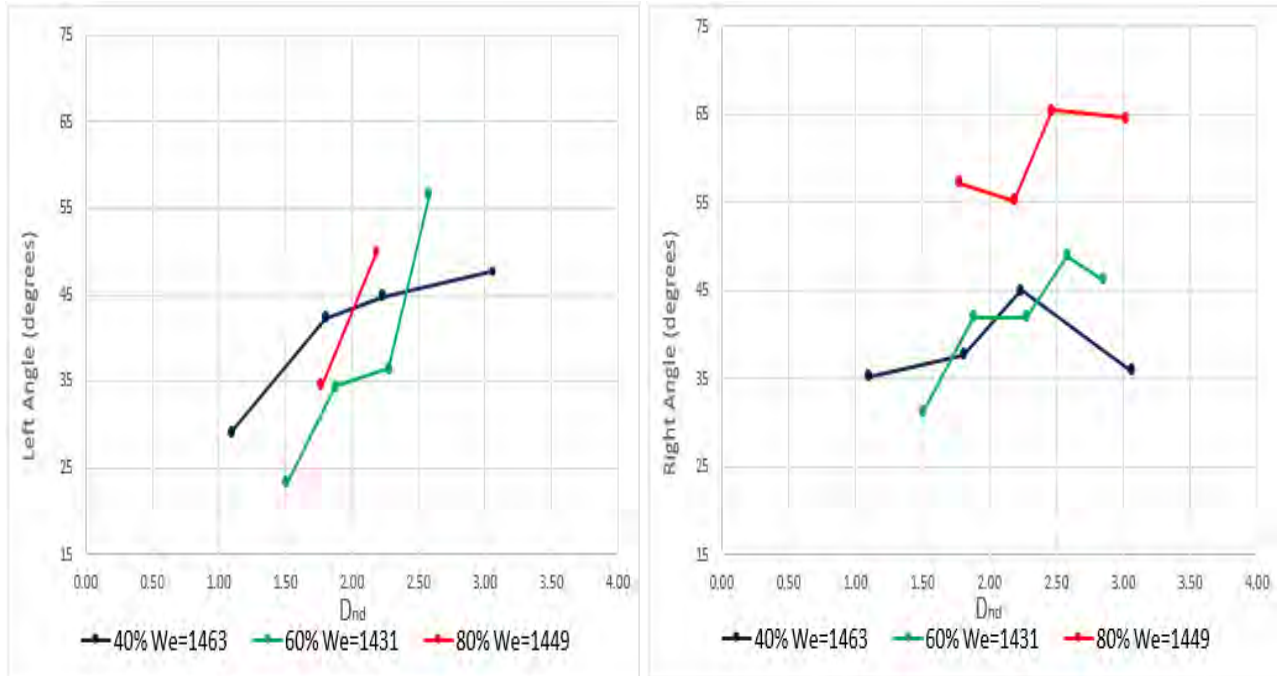


Figure 5-5: Crown angles on the upslope (left) and downslope (right) side for inclination of  $\theta=10^\circ$ ,  $H=0.99m$

In **Figure 5-6**, the asymmetric formation of the crown is observed for impact on  $20^\circ$  slope. For all the mixtures the crown formation seems more vigorous on the downslope side with greater and longer enduring angles. Therefore the inclination seems to have a suppressive effect on the upslope side angle formation. For the 40% mixture from the early stages of crown formation until about  $2D_{ND}$  the behavior and values of both side angles is quite close to each other. Eventually as the diameter increases the right side presents higher durability and increases to 45 degrees before collapsing at about  $3.5D_{ND}$ , while the left angle obtains a stable value of about 25 degrees and collapses at  $2.5D_{ND}$ . The relationship between the angles of the 60% mixture follows a similar trend until about  $2D_{ND}$ . Both angles display an initial decrease on their values, with the left one presenting values about 10 degrees greater. Afterwards the right angle follows a steep value ascent, while the left collapses earlier. It is worth to refer that the right angle seems to decrease again after  $3D_{ND}$  before collapsing at  $3.5D_{ND}$ . The 80% mixture displays crown formation only on the downslope side, with the tick phenomenon taking place.

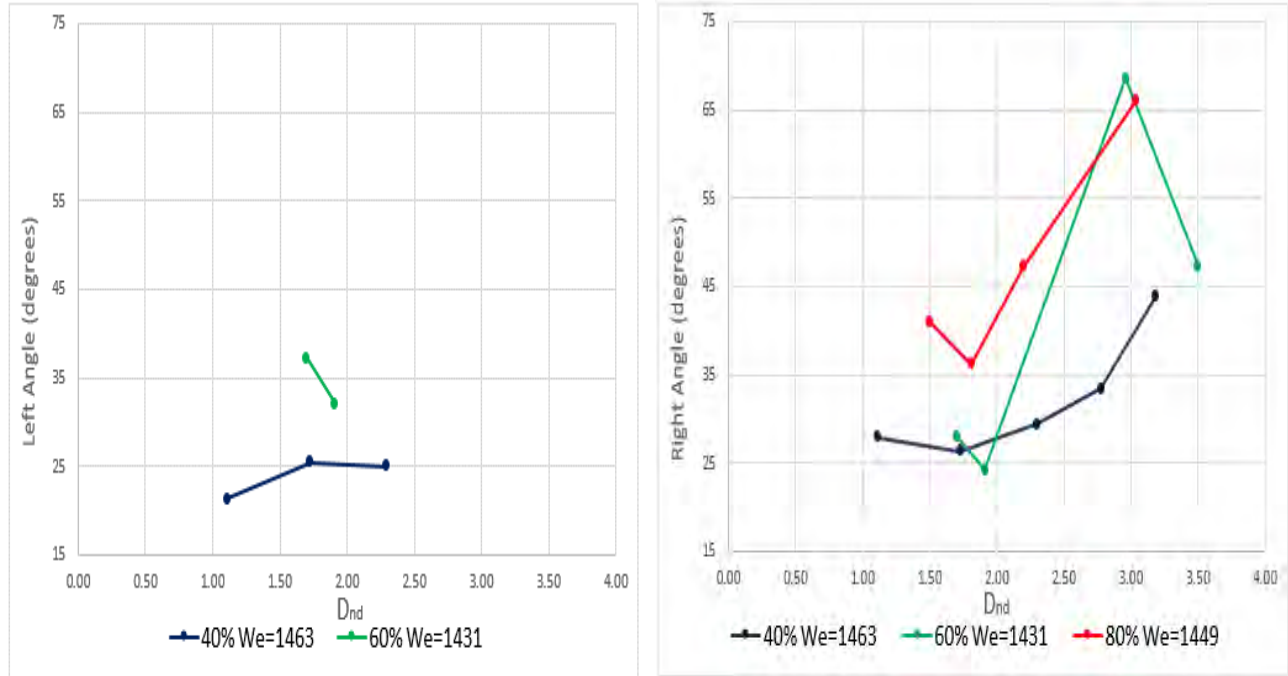


Figure 5-6: Crown angles on the upslope (left) and downslope (right) side for inclination of  $\vartheta=20^\circ$ ,  $H=0.99m$

Figure 5-7 displays the suppressive effect of high inclination on the upslope side's crown formation. Even for the highest Weber numbers examined, no left side splashing is observed for 60 and 80% w/w methanol and the 40% mixture presents a small and short-lived left side crown formation with angle values below 20 degrees. On the contrary, on the right side the corona splashing is more energetic. The angle of the 40% mixture is extremely durable and displays a tick phenomenon resulting in angles of about 60 degrees before collapsing at  $4D_{ND}$ . The other mixtures present an increasing and a decreasing trend on their angles respectively before collapsing at about  $3D_{ND}$ .

In Figure 5-8 the fall height is decreased to 0.89cm and the substrate is horizontal. A symmetry of the crown evolution between the right and left side for all the mixture is observed. On both sides the angle of the 60% mixture has the highest values and the corona splashing regime seems to remain observable at greater  $D_{ND}$  values. On the 40% mixture both side angles obtain their maximum value around  $2D_{ND}$  and then display a steady behavior until collapse. The 80% mixture is the only one that presents a relative asymmetry, because the right side angle presents a steeper value ascent to 45 degrees at about  $1.25D_{ND}$  in comparison with left sides 35 degrees. Finally the corona lifespan appears to be the shortest for this mixture on both sides of the crown.

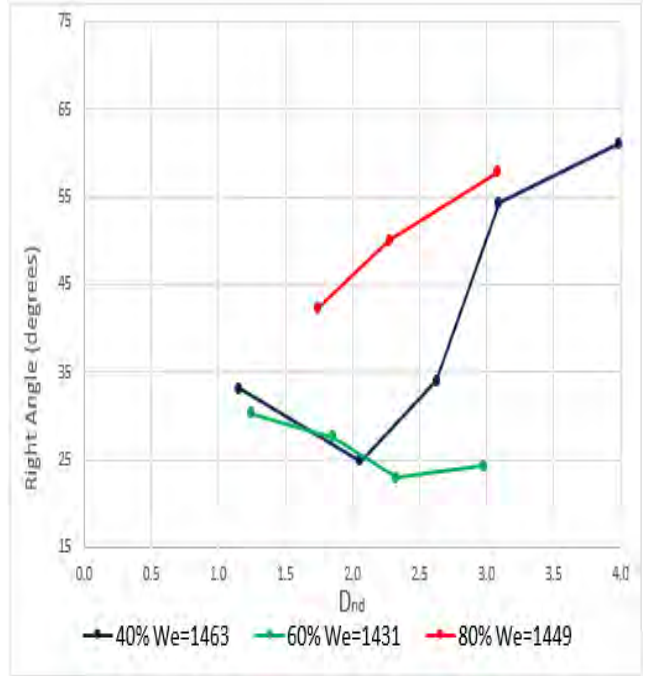
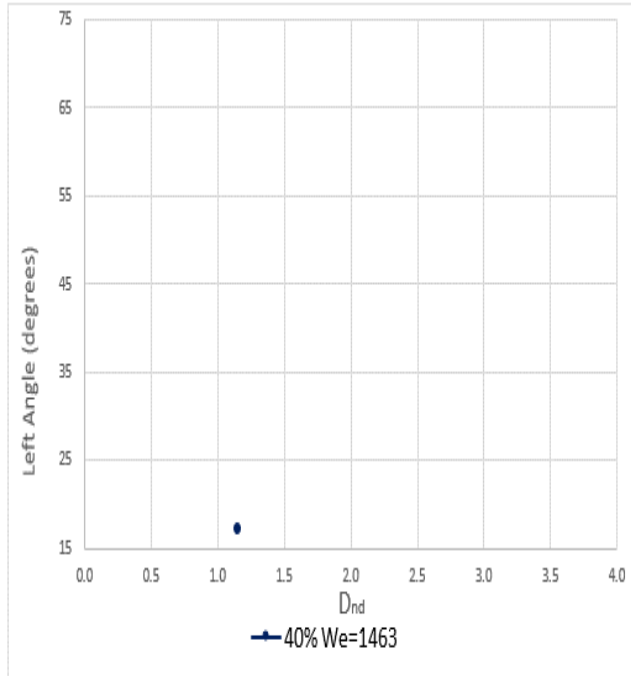


Figure 5-7: Crown angles on the upslope (left) and downslope (right) side for inclination of  $\vartheta=30^\circ$ ,  $H=0.99m$

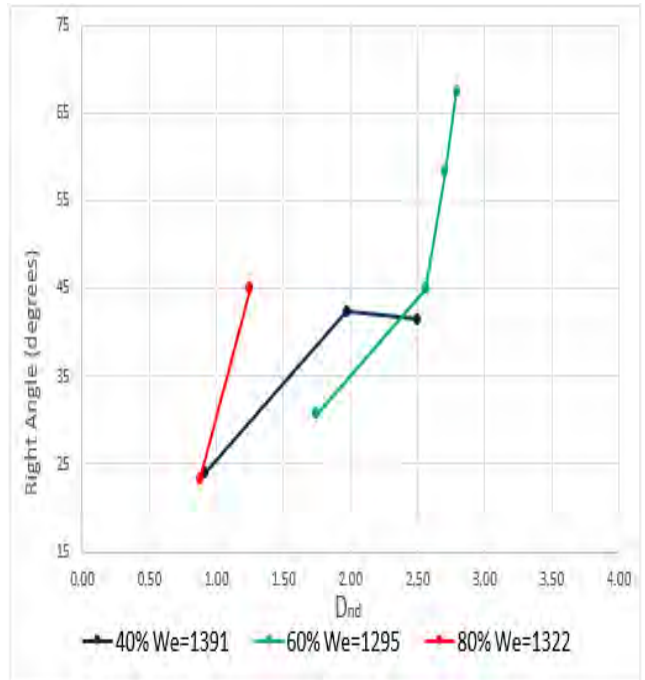
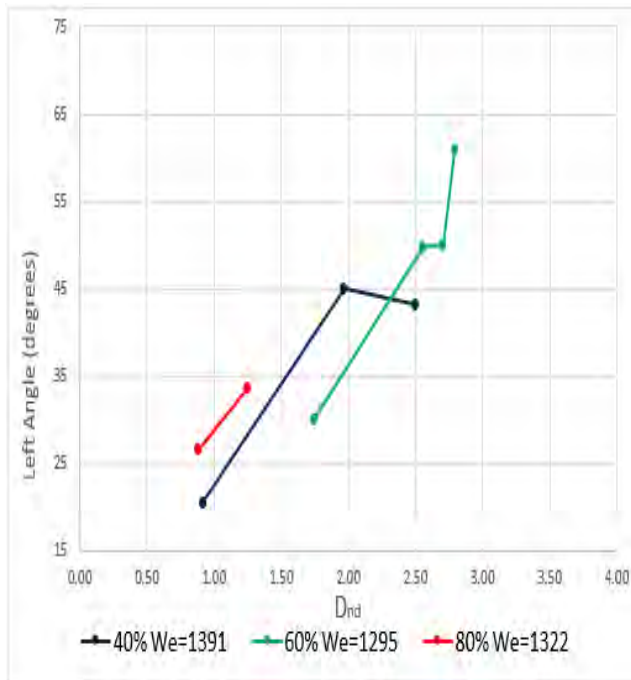
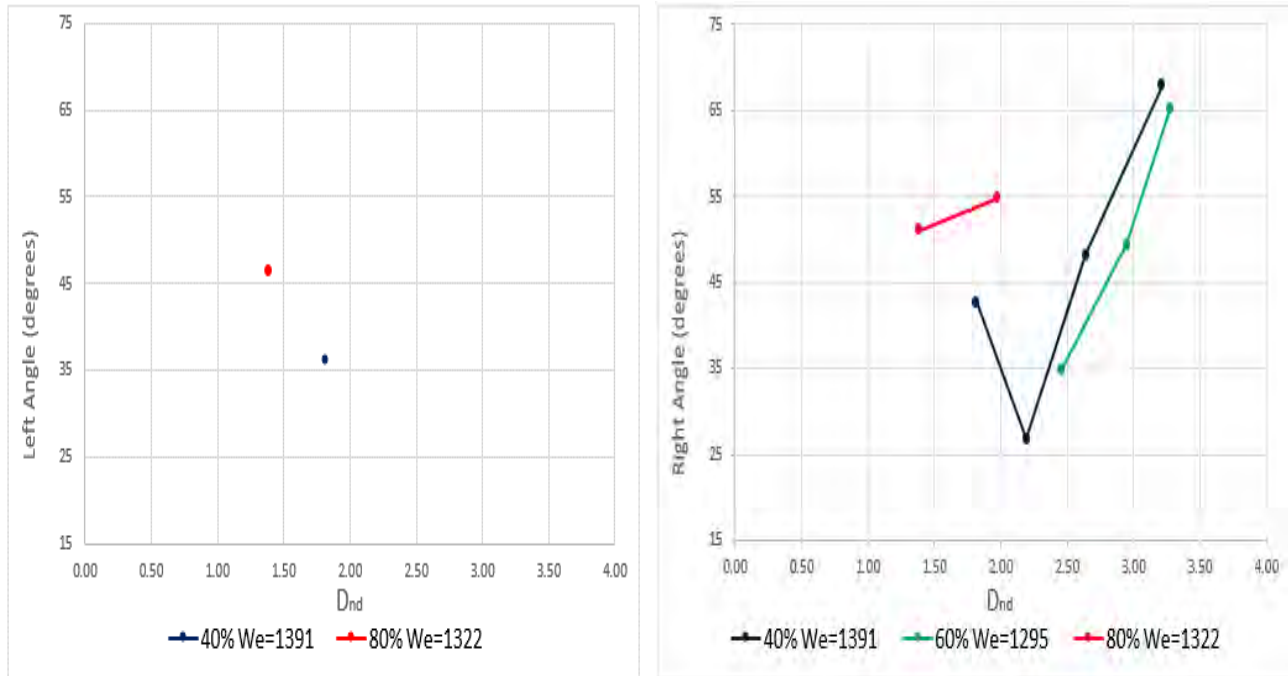


Figure 5-8: Crown angles on the left and right side for horizontal substrate,  $H=0.89m$



From **Figure 5-9** it is obvious that the corona splash is much more vigorous on the right side of the crown than on the left. This may happen due to the inclination of the substrate that provokes a gravitational tendency of the liquid to move on the downslope right side of the crown. Once more the right angle of the 80% mixture tends to have higher values at the initiation of the crown formation, but in the latter stages of the phenomenon the right angles of other mixtures display a steepest increase and obtain larger values. The 80% mixture angle is the briefest. On the left side there is no corona formation for the 60% mixture, which presents the lower Weber number in comparison with the other mixtures, while the phenomenon is short-lived for the other mixtures.



*Figure 5-9: Crown angles on the upslope (left) and downslope (right) side for inclination of  $\vartheta=10^\circ$ ,  $H=0.89m$*

The right angles in **Figure 5-10** display the tick phenomenon with the one of the 80% mixture being the one with the highest values but also the most short-lived. The 40% mixtures angle survives the longest forming at about  $0.5D_{ND}$  and collapsing after  $3D_{ND}$ . For the 60% mixture a left angle is observed something that didn't happen for smaller inclinations at the same Weber number (**Figure 5-9**). Moreover the value of the left 60% mixture angle is greater that the right one. Interestingly enough we observe upslope crown formation for the 80% mixture something that didn't occur for higher Weber number at the same inclination (**Figure 5-6**).

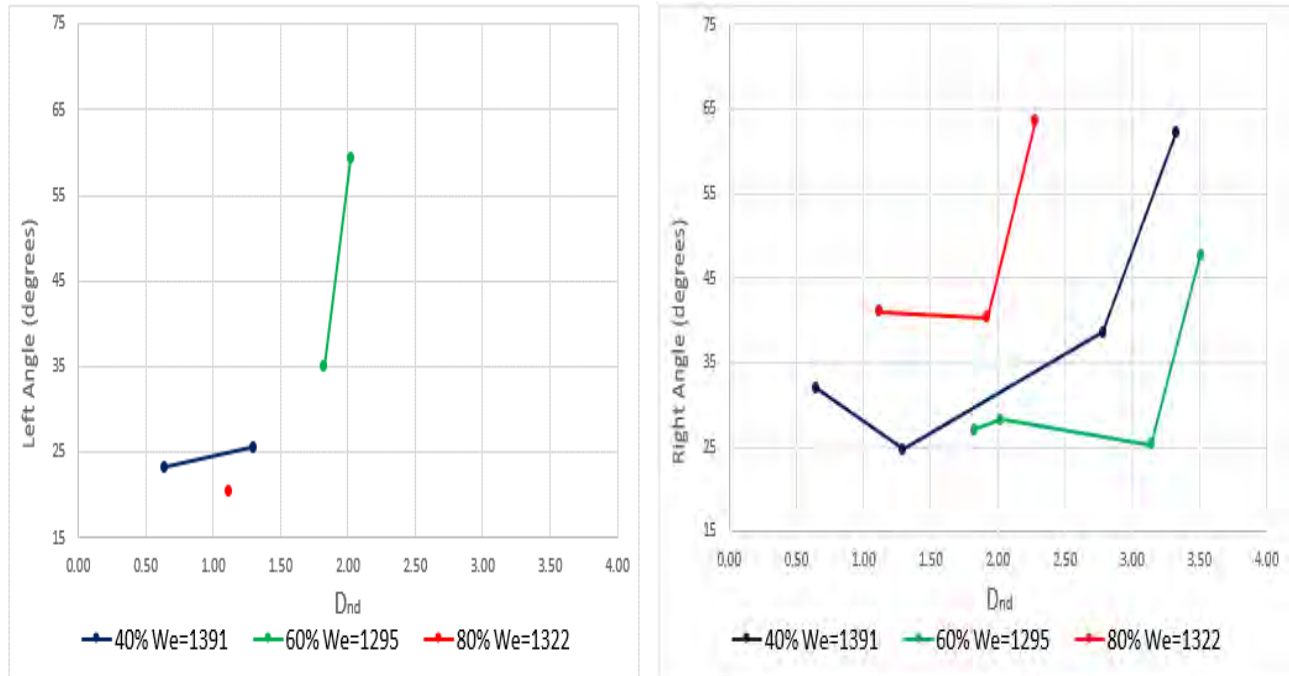


Figure 5-10: Crown angles on the upslope (left) and downslope (right) side for inclination of  $\theta=20^\circ$ ,  $H=0.89\text{m}$

For a  $30^\circ$  slope, on the upslope side the crown is suppressed by gravitational effects and lasts shortly only for the mixtures with the higher Weber numbers (Figure 5-11). On the downslope side the crown is more noticeable. However it appears more short-lived compared to the right crowns of Figure 5-10. The right angle of the 40% mixture takes the highest values and conforms to the tick phenomenon as does the 60% angle. The angle for the 80% mixture appears steady and collapses at an earlier stage.

For the height of 0.79m and a horizontally placed substrate (Figure 5-12), we observe a shorter length of the corona splashing regime in comparison with heights (Figure 5-4, Figure 5-8), that result to higher Weber numbers. Both side angles of the 40% mixture present a similar behavior and almost identical values. This fact ascertains the crown symmetry for horizontal surfaces. Moreover, this mixture is the one that presents the longest timespan between the formation and the collapse of the crown. For the 80% mixture the crown is steep, short-lived and with bidirectional symmetry. However, the 60% mixture angles present a relative asymmetry with the left one being slightly greater at about  $2D_{ND}$ .

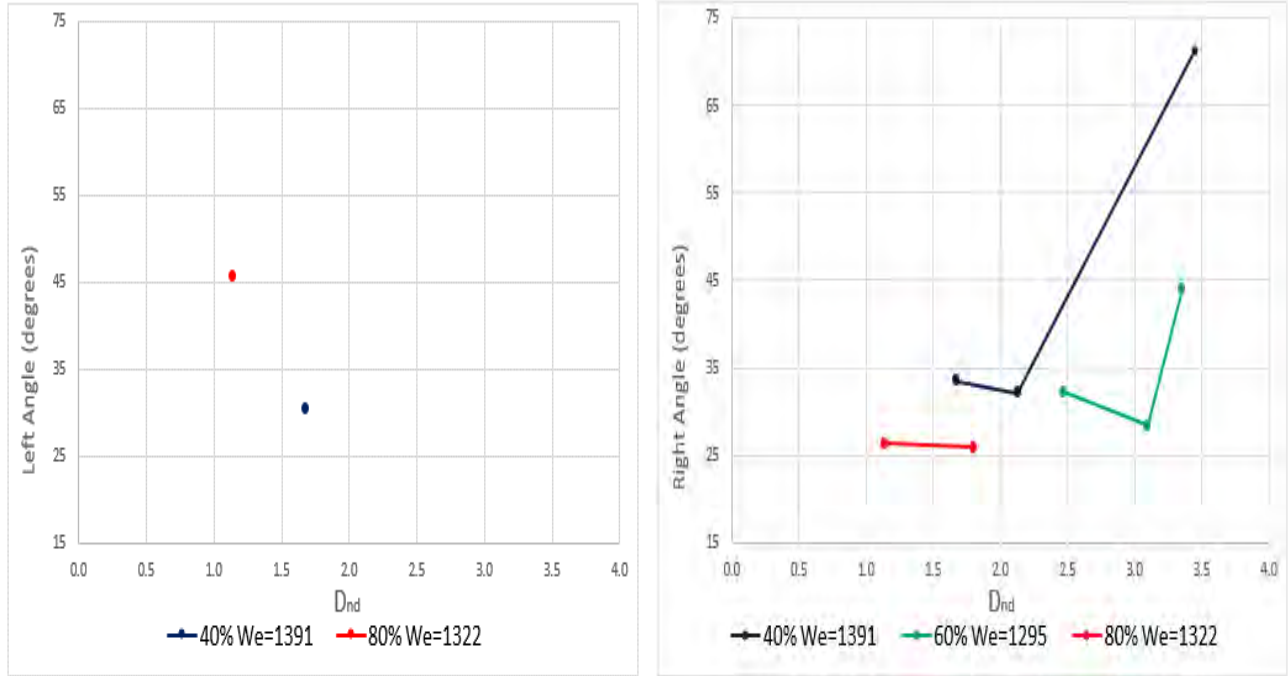


Figure 5-11: Crown angles on the upslope (left) and downslope (right) side of inclination of  $\theta=30^\circ$ ,  $H=0.89\text{m}$

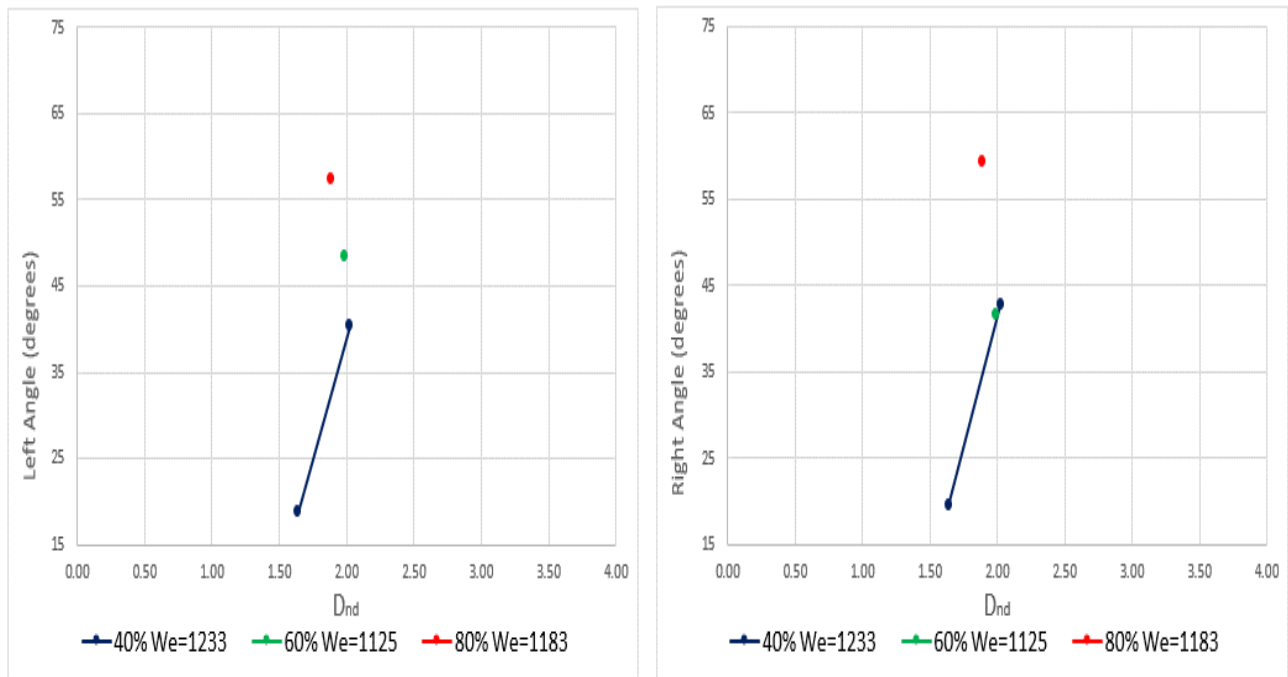
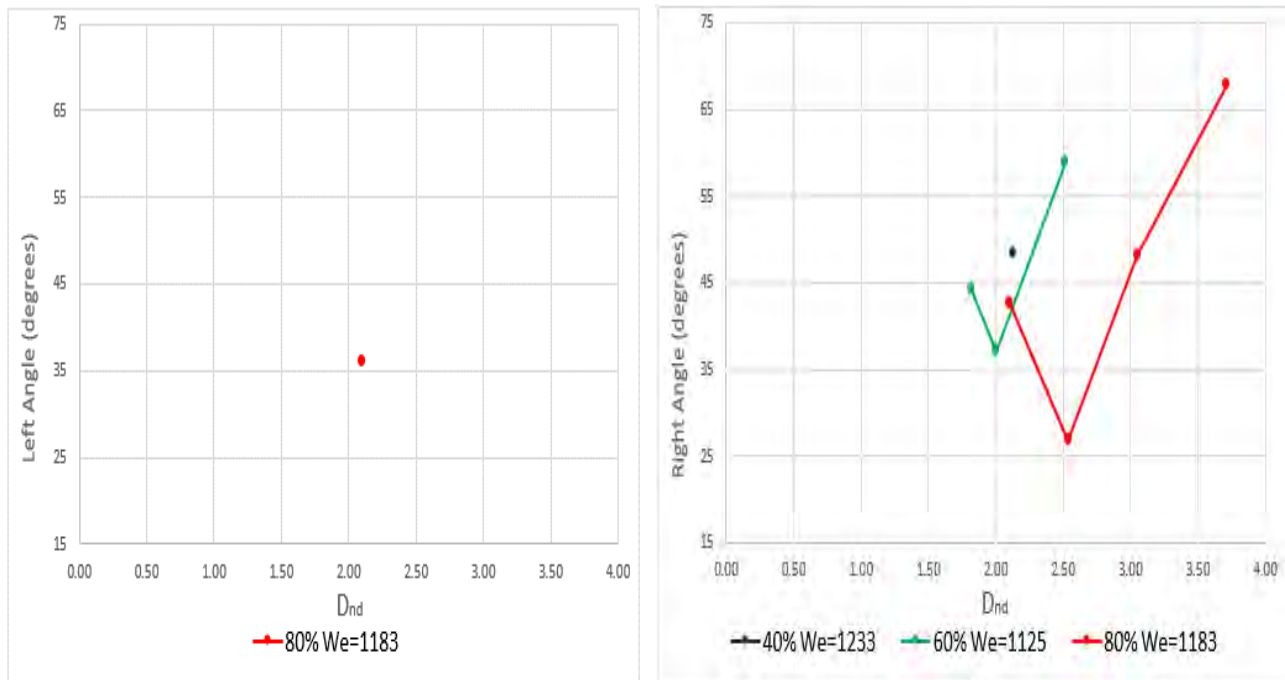


Figure 5-12: Crown angles on the left and right side for horizontal substrate,  $H=0.79\text{m}$

On the left side of **Figure 5-13**, it appears that as the height decreases compared to **Figure 5-9** and as the inclination increases compared to **Figure 5-12** the only mixture with an observable upslope corona splash is the 80%. On the right side the splashing is more prominent for 60 and 80% where we observe the tick phenomenon. This phenomenon begins with a sudden decrease of the angle and a latter steep increase on the highest value obtained, before the collapse. The initial decrease can be attributed to the formation of the bowl shaped corona and the increase afterwards to the final stages before the disintegration of the crown, when the lower part of it has already collapsed and only the higher more inclined parts remain detached form the substrate. In contrary the 40% mixture presents a more abrupt and short-lived right angle.



*Figure 5-13: Crown angles on the upslope (left) and downslope (right) side for inclination of  $\vartheta=10^\circ$ ,  $H=0.79m$*

Similarly to **Figure 5-13**, in **Figure 5-14** the downslope angles obtain greater angle values than the upslope ones and survive for a longer period. The 80% mixture right angle displays a straightforward increase, while the tick phenomenon is witnessed for the other mixtures. The lifetime of the crown for all the mixtures appears to be similar (about  $1D_{ND}$  from formation till collapse). On the left side the only mixture that displays a crown and angle formation, however short-lived, is the 80%.

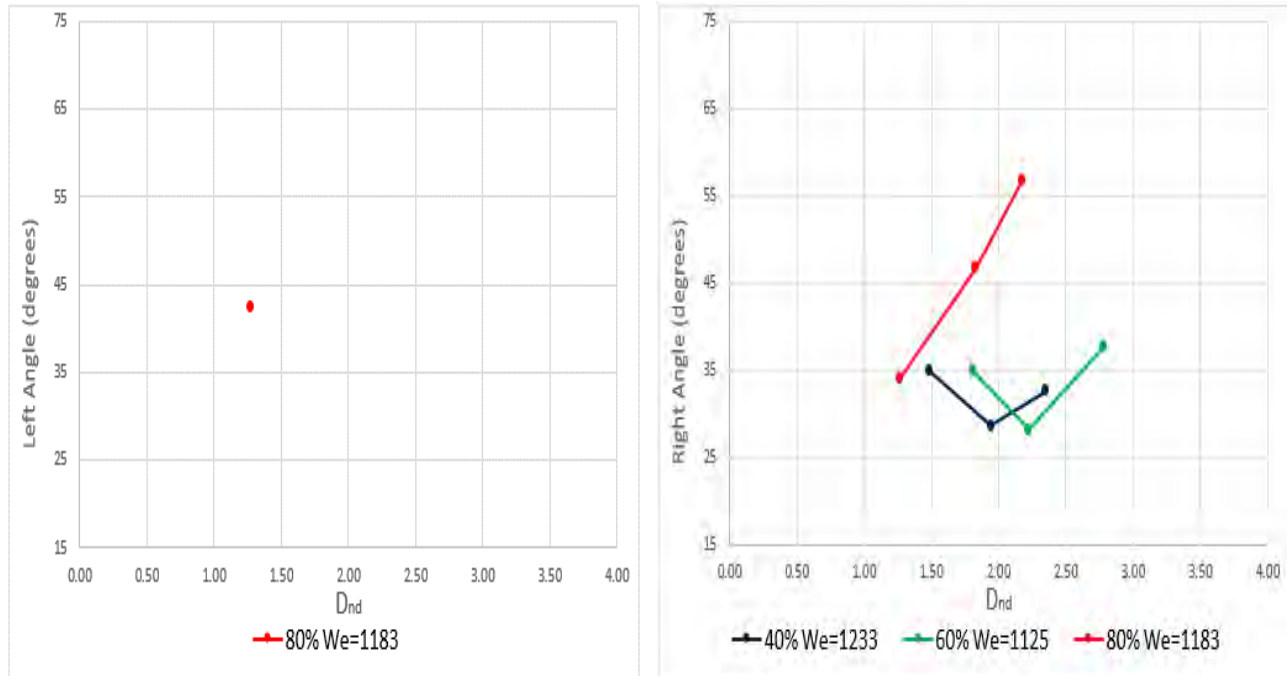
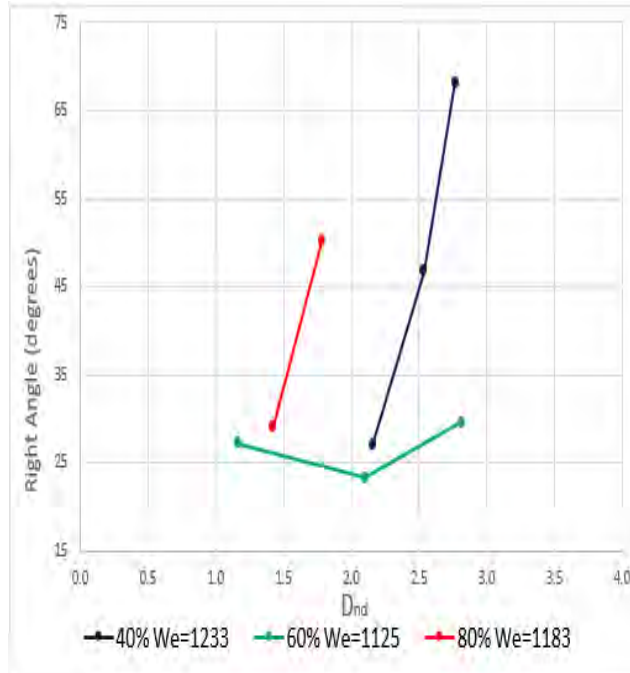


Figure 5-14: Crown angles on the upslope (left) and downslope (right) side for inclination of  $\vartheta=20^\circ$ ,  $H=0.79m$

**Figure 5-15** represents the lowest height of experimental measurements and the highest inclination of the substrate. Only the right angles of the crown are illustrated because no mixture forms a crown on the upslope side. This happens firstly due to the gravitational pull of the liquid to the downslope side which is at its maximum for an inclination of  $30^\circ$ , accompanied by the decreasing value of the Weber number for 0.79m. On the right side the 60% mixture displays an almost steady angle value throughout the crown life. However the angle behavior for other two mixtures, that present higher Weber numbers, is characterized by a steep increase on their values before collapse.

In general the impingement on a horizontal substrate leads to a crown formation that is symmetrical on both sides. On the contrary, the impact on inclined substrates leads to an asymmetrical crown formation. This asymmetry tends to become even more obvious as the inclination increases gradually from  $10^\circ$  to  $30^\circ$ . The downslope side displays a more energetic crown formation with greater lifespan in comparison with upslope side where the crown tends to disappear for  $30^\circ$ .



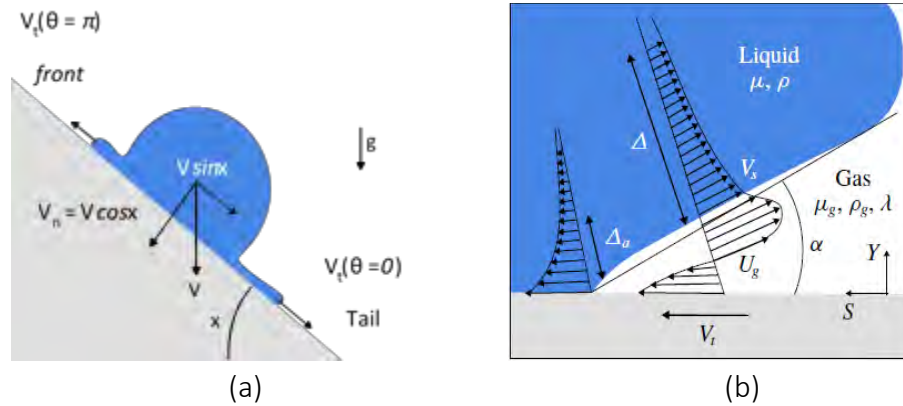
**Figure 5-15: Crown angle on the downslope (right) side for inclination of  $\theta=30^\circ$ ,  $H=0.79m$**

The general trend in most cases is an increase on the value of the angle from the formation stage till the collapse stage. The tick phenomenon is displayed mainly on the right side angle during impingement on inclined substrate. While the corona formation begins and the bowl shaped crown forms, a slight decrease on the angle is noticed. This decrease is more obvious for downslope angles because the gravitational forces push the liquid downwards. Afterwards as a portion of the crown attaches to the substrate, the angle increases.

The mixtures with 40% and 80% w/w methanol that present the higher Weber numbers form more durable crowns than the 60% mixture, as the impingement height decreases and the inclination of the substrate increases. The mixture that presents the greatest crown lifetime in most cases is the one with 40% w/w methanol which endures at average between 1.5 and  $2D_{ND}$ .

### 5.2.3 Riboux-Gordillo Criterion – Inclined Surfaces

After observing splashing behavior of the six water-methanol solutions, on flat smooth surfaces, corona splashing formation was also anticipated empirically for the 40%, 60% and 80% solutions, on smooth surfaces with inclination. Based on our photograph results, we tried to make use of two different splashing criteria one given by Bird et Al. (2009) and the other by Riboux and Gordillo (2019). In both formulas the tangential velocity of the upslope side was taken equal (with opposite sign) to the downslope velocity as it was not possible via the images taken to determine the difference between the upward and downward spread of the lamella. However, the first criterion which considers both prompt and corona formations to determine the splashing threshold could not be applicable in our results due to the background blurring of some images, which made separation of deposition from prompt splash uncertain. As a result, we only calculated the Riboux-Gordillo (RG) threshold to crosscheck the outcome of our experiments.



Caption: a) Sketch showing a drop falling at a velocity  $V$  onto a substrate inclined at an angle  $x$  with respect to the horizontal direction and some of the different variables used in the analysis, with  $\theta$  indicating the angular position on the impact plane. b) Sketch of the flow at the edge of the liquid sheet and at the lubrication gas layer in a frame of reference moving at  $Vt$ ; here,  $U_g$  indicates the gas velocity field and  $V_s$  is the liquid velocity at the gas–liquid interface. Wedge angle is  $\alpha$ .  $\Delta$  is the width of the viscous boundary layer induced by gas shear stresses and  $\Delta\alpha=R\delta$  proportional to  $R(Re^{0.5} t_e)$ , is the thickness of the liquid boundary layer developing at the wall. The material properties of the two fluids involved are also indicated in this figure.

In their paper in 2019 (Gordillo & Riboux, 2019), they came up with a formula which determines the critical velocity for an impacting drop to break up into smaller droplets. Neglecting gravitational effects ( $Fr(Vn) \gg 1$ ), working with low viscosity liquids and droplets with diameters up to 4mm the following formulas are applicable:

$$t_e = 1.05We^{-2/3} \quad (35)$$

$$K_l = \ln \left[ A \left( \frac{\mu_g}{\mu} \right)^{3/4} Oh^{-1/4} We^{-1} \frac{R}{\lambda} \right] \quad (36)$$

$$K_l \frac{\mu_g}{\mu} OhWe^{5/6} \left[ 1 + 2 \frac{t_e^{1/2}}{\sqrt{3}} \tan(x) \cos(\varphi) \right] = K \cong 0.0034 \quad (37)$$

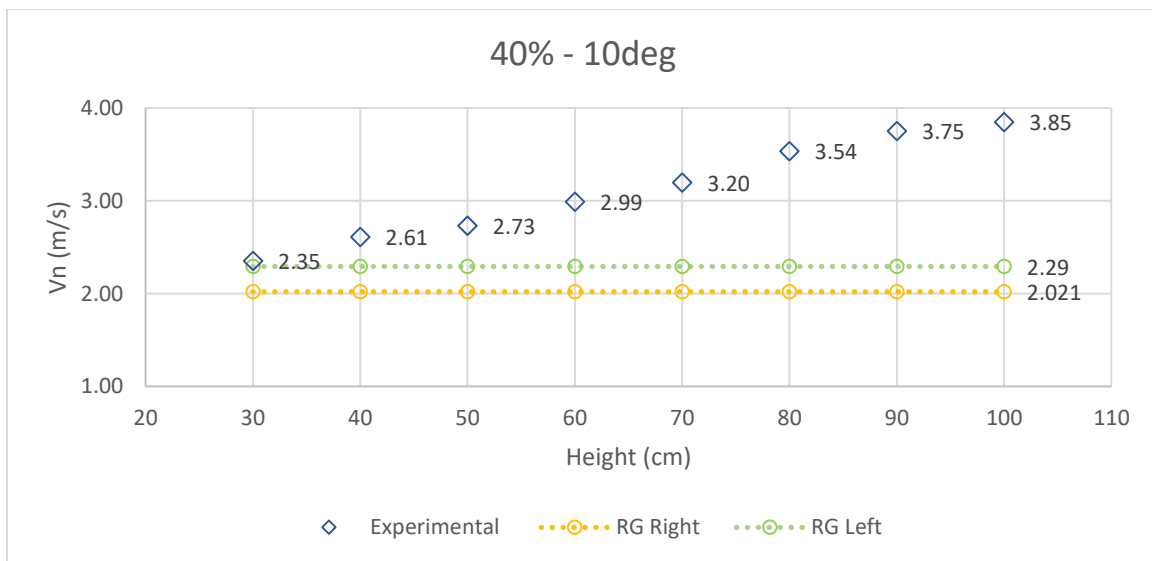
Where  $\lambda$  is the mean free path of the gas molecules (at 25°C and 1 atm, for air  $\lambda=6.7 \times 10^{-8}$  m, taken from Jennings, 1988 and a fitting constant for wedge angle  $\alpha \approx 60^\circ$ ). For the calculation of  $We$  and

Re numbers is used the velocity  $V_n$ , normal to the surface. The equations were solved numerically in excel as the only unknown value is the threshold velocity  $V_n$ .

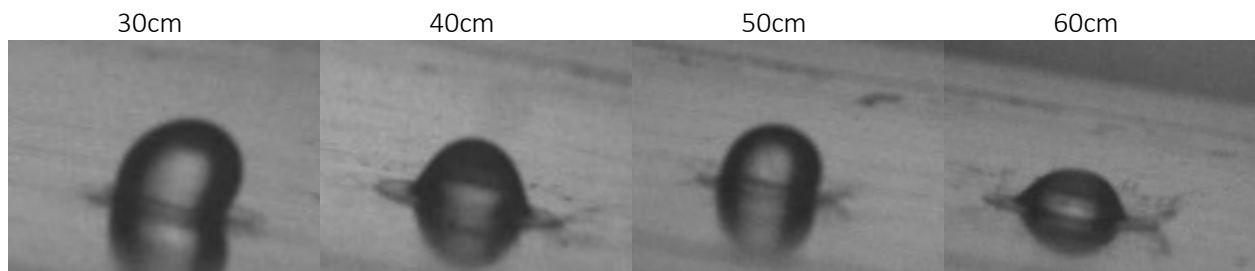
Generally, via the RG criterion is observed that the threshold velocity for the downslope side is always lower than the one in the upslope. Furthermore, as the inclination increases the threshold velocity for the downslope side decreases. This is also mathematically reasonable as the tangential velocity contains the sine of inclination angle  $\alpha$  which is an increasing function in  $[0, 90^\circ]$  and as it has been known greater values of velocity favor splashing. On the other hand, the value of the upslope side threshold velocity decreases going from 10 to 30 degrees.

In the following diagrams the calculated downslope ( $\phi=0$ ) and upslope ( $\phi=180^\circ$ ) side threshold velocity are drawn in yellow and green dots respectively. Triangles are used to express experimental downslope splashing (according to the laboratory images) and rhombuses for symmetrical (both side) splashing. Circles indicate no splashing.

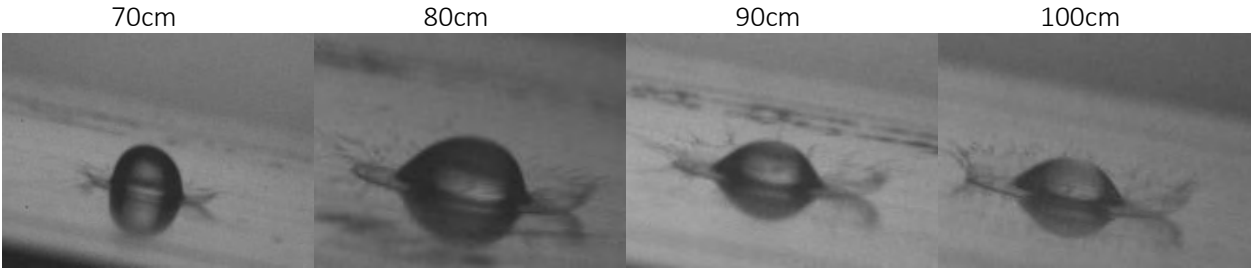
By the term deviation is marked, at each case, the maximum numerical difference between the splashing threshold occurring from the RG criterion and the velocity estimated from the images taken (**Figure 4-11**). In other word how much lower is the former from the latter.



**Figure 5-16: Riboux-Gordillo velocity thresholds for 40% water-methanol solution at 10 degrees tilt angle.**

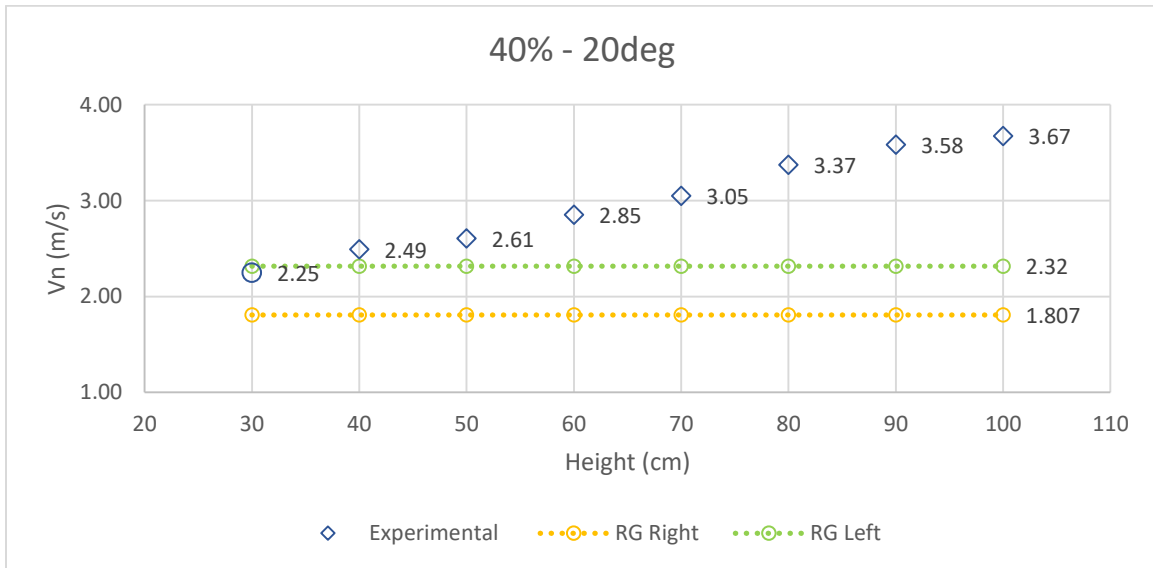






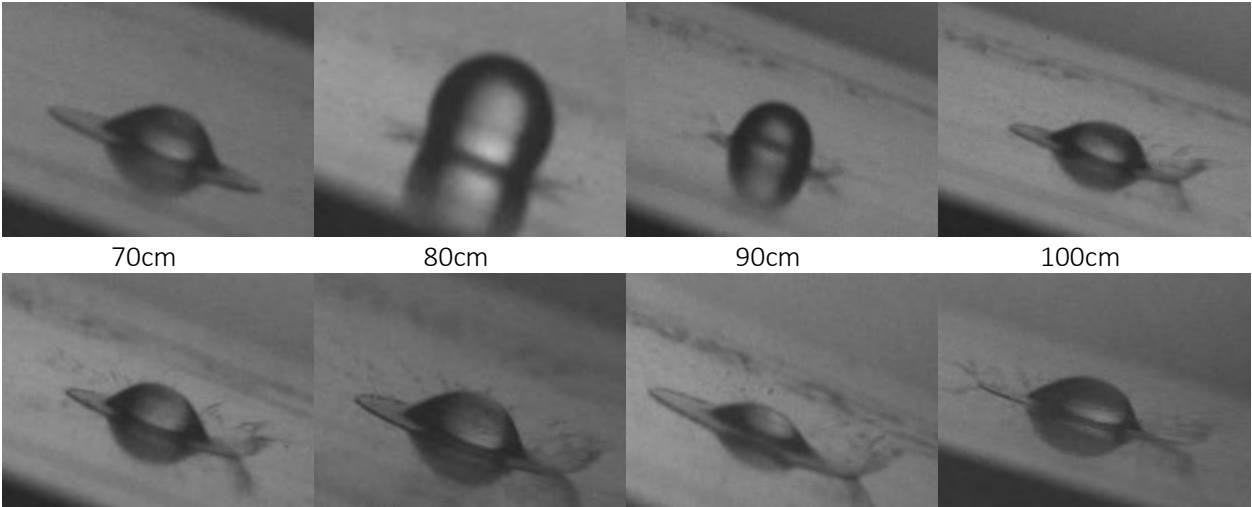
**Figure 5-17: 40% w/w methanol solution at 10 degrees tilt angle**

According to RG model, for 40% w/w water-methanol solution and 10degrees inclination, corona splashing should occur above 2.29m/s (at the upslope) and 2.021m/s (at the downslope). Lowest measured velocity during the experiments for this solution is 2.35m/s when the falling distance is set at 30cm. Indeed, from the captured photographs corona splash is the case. However, it has to be noted that on the left side its formation is much smaller in size its disintegration happens quicker than the disintegration on the right side of the substrate (downslope). Corona formation also appears “weaker” as the falling height decreases as it can be clearly seen, comparing the images which correspond at 30cm and 100cm.



**Figure 5-18: Riboux-Gordillo velocity thresholds for 40% water-methanol solution at 20 degrees tilt angle.**

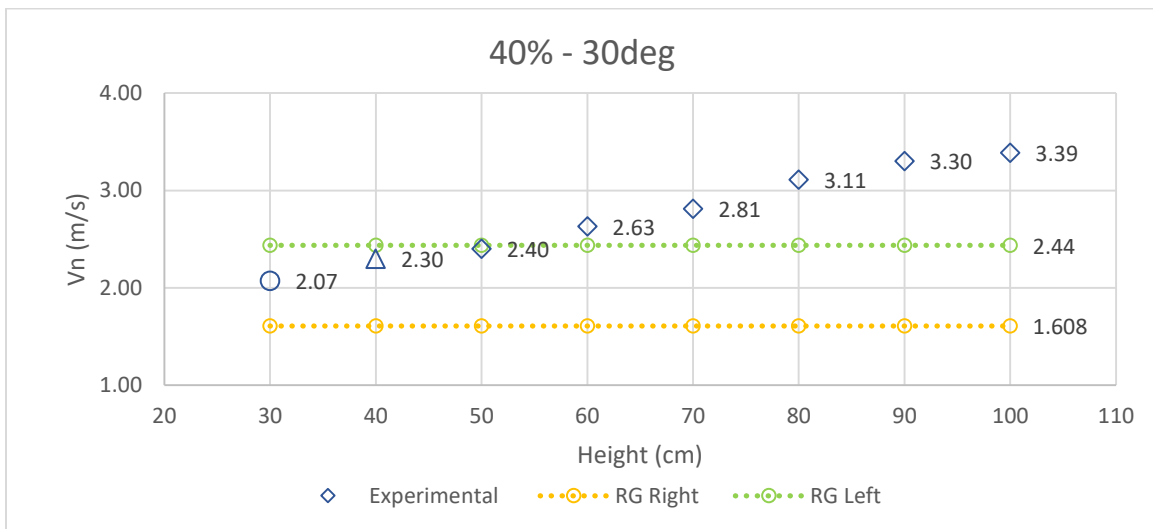
30cm                                      40cm                                      50cm                                      60cm



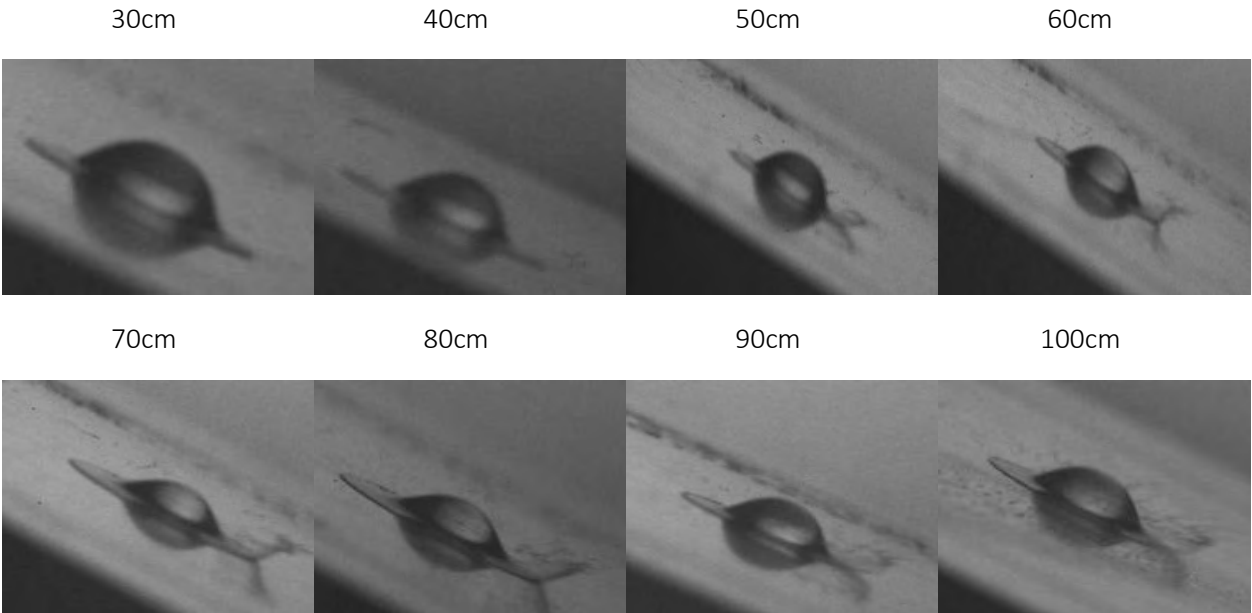
**Figure 5-19: 40% w/w methanol solution at 20 degrees tilt angle**

At 20degrees inclination, threshold velocities are 2.32m/s and 1.087m/s at the upslope and at the downslope side respectively. Lowest measured velocity for this solution is 2.25m/s (at 30cm height), which predicts corona splashing on the downslope side. However, the fact that, in the laboratory image for 30cm, in the moment captured, we estimate from the spreading of the lamella that the breakup stage should be at its end and the blurring in the background, does not allow us to determine splashing occurrence with certainty.

Moreover, the effect of weaker formation and faster breakup of the corona on the left side is even more visible as we go backwards from 100cm to 30cm than in 10 deg inclination which is quite reasonable as mentioned in the beginning of the paragraph. In addition, the splashing on the right side keeps its size till 60cm while at 10 degrees it begun to shrink from 80 cm and below.



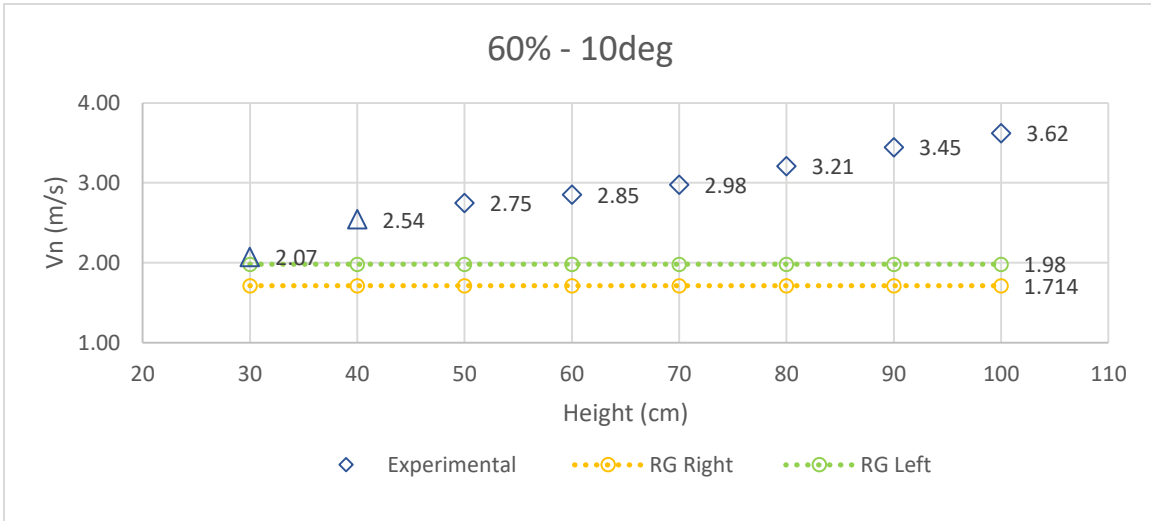
**Figure 5-20: Riboux-Gordillo velocity thresholds for 40% water-methanol solution at 30 degrees tilt angle.**



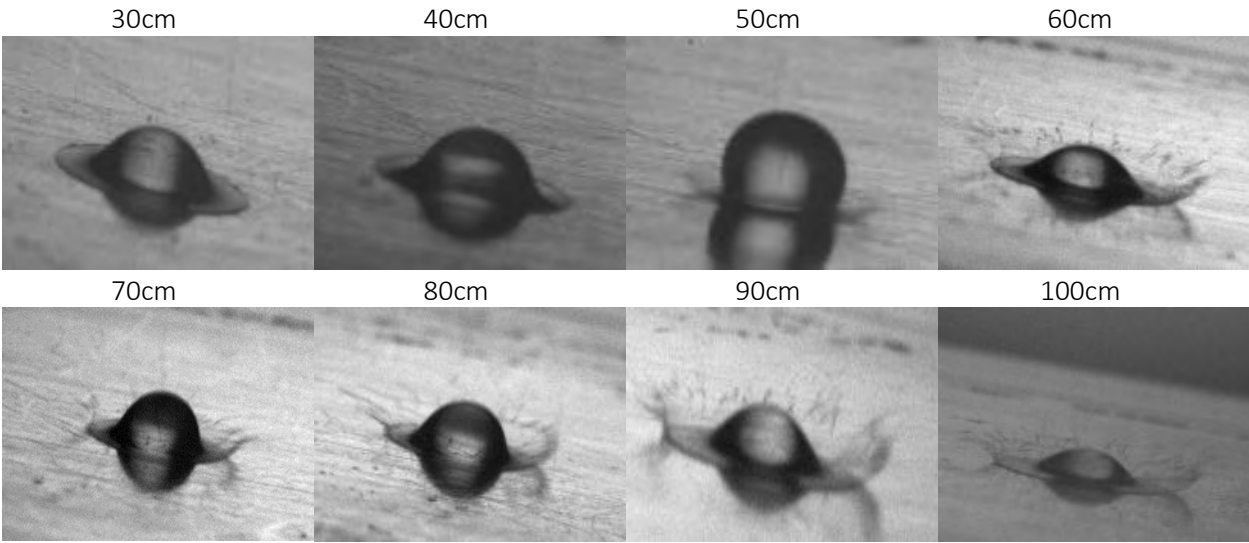
**Figure 5-21: 40% w/w methanol solution at 30 degrees tilt angle**

At 30degrees inclination, threshold velocities are 2.44m/s and 1.608m/s at the upslope and at the downslope side respectively. Lowest measured velocity for this solution is 2.07m/s (at 30cm height), which falls between the two thresholds, so corona splashing on the downslope side is anticipated. However, the fact that, in both laboratory images for 30 and 40cm, apply what was mentioned for 20degrees and 30cm (breakup stage should be at its end and background blurring prevent the accurate determination of splashing). However, for 40cm, remains of the corona can be distinguished. In this case we have the first notable deviation (0.37m/s) at downslope splashing threshold and the photograph result at 30cm. Moreover, at 50cm there is a neglectable deviation of 0.04 m/s between the threshold velocity for left side splashing and the one measured ( $<u,thr$ ).

The effect of weaker formation and faster breakup of the corona on the left side is even more visible as we go backwards from 100cm to 30cm than in 10 deg and 20degrees inclination as the left side splashing is not captured in any image, only its remains. Furthermore, the splashing on the right side keeps its size till 70-60cm.



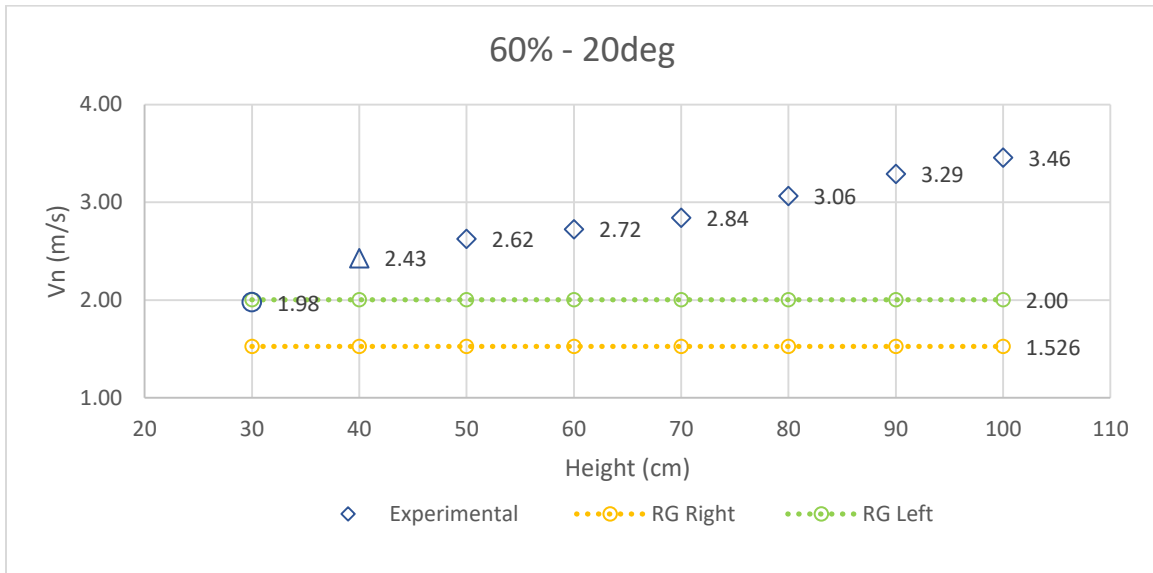
**Figure 5-22: Riboux-Gordillo velocity thresholds for 60% water-methanol solution at 10 degrees tilt angle.**



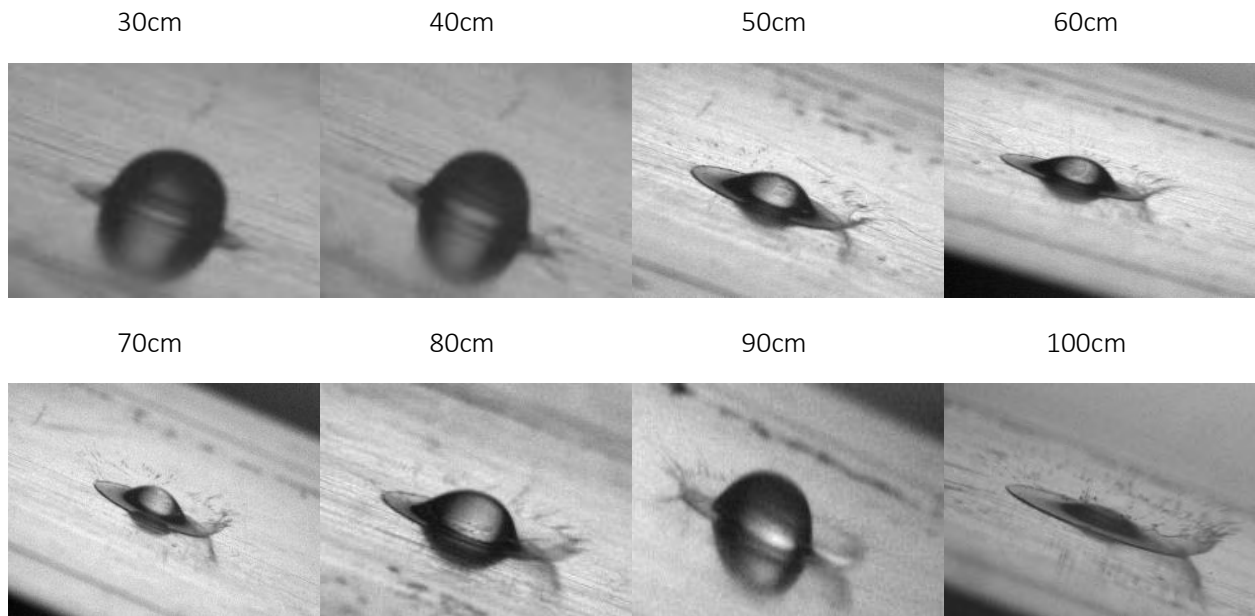
**Figure 5-23: 60% w/w methanol solution at 10 degrees tilt angle**

According to RG model, for 60% w/w water-methanol solution and 10degrees inclination, corona splashing should occur above 1.98m/s (upslope) and 1.714m/s (downslope). Lowest measured velocity during the experiments for this solution is 2.07m/s when the falling distance is set at 30cm and corona splashing is expected at both sides at all times. In the photo for 30cm height we can distinguish corona splashing during its late breakup and so we can assume that right side splashing is also the case for 40cm. However, concerning left side splashing, photographic material indicates

its disappearance from 40 cm and below. As a result, we get a deviation of 0.56 m/s at 40 cm and a neglectable 0.09m/s at 30 cm.



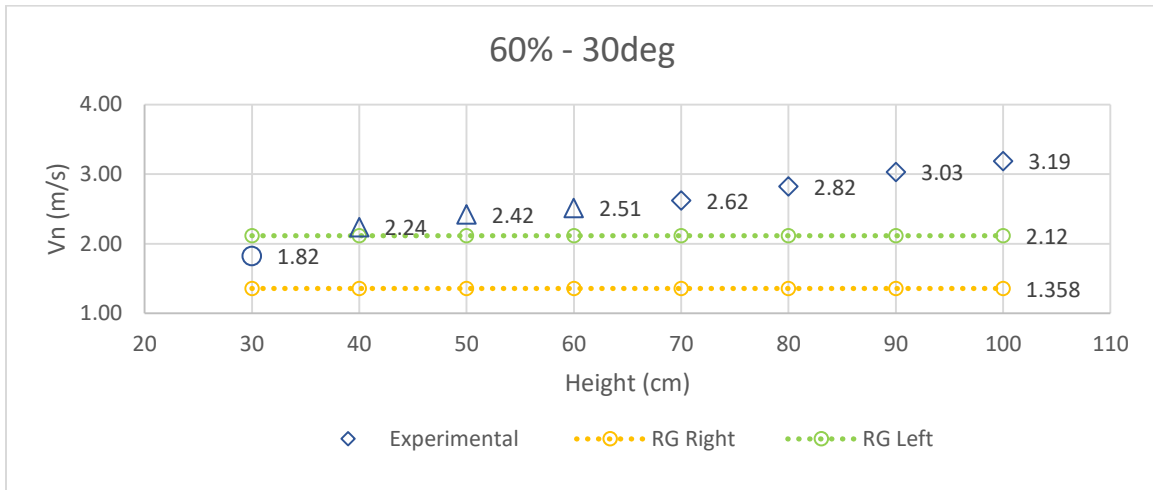
**Figure 5-24: Riboux-Gordillo velocity thresholds for 60% water-methanol solution at 20 degrees tilt angle.**



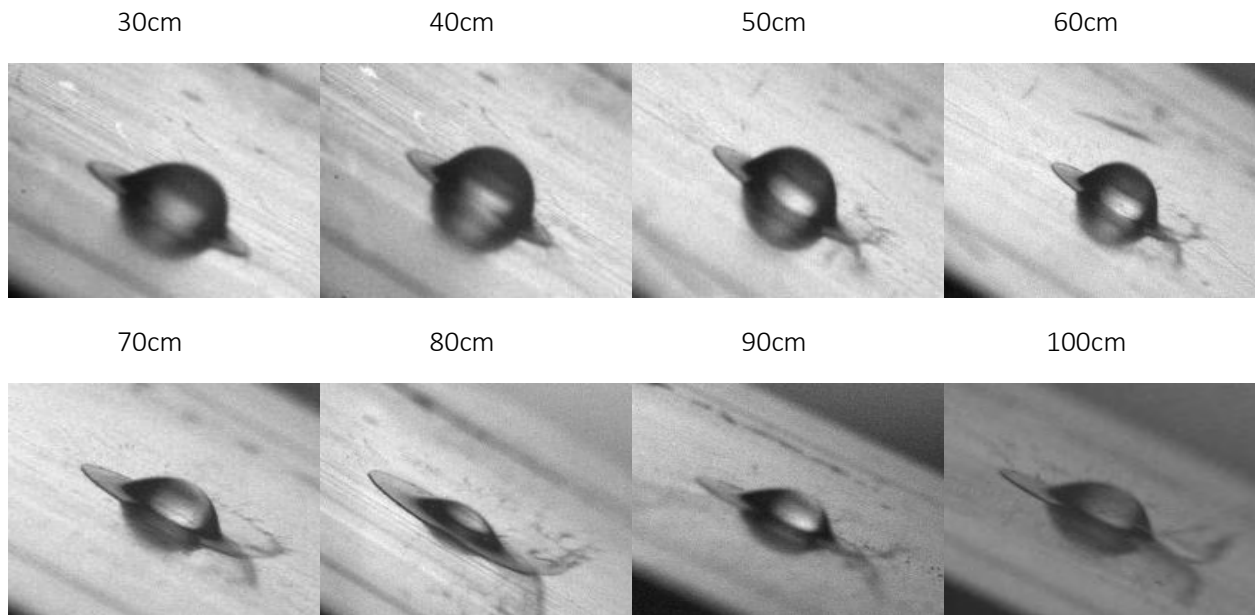
**Figure 5-25: 60% w/w methanol solution at 20 degrees tilt angle**

At 20 degrees inclination, threshold velocities are 2m/s and 1.526m/s at the upslope and at the downslope side respectively. Lowest measured velocity for this solution is 1.98m/s (at 30cm height), which falls between the two thresholds, so corona splashing on the downslope side is anticipated. Indeed, splashing remains can be distinguished at all cases on the right side, so there is no mismatching at this case. However, splashing is also predicted via the RG criterion on the left

side at 40cm height which is contradictory to the experimental image. The deviation in this case is 0.43m/s.



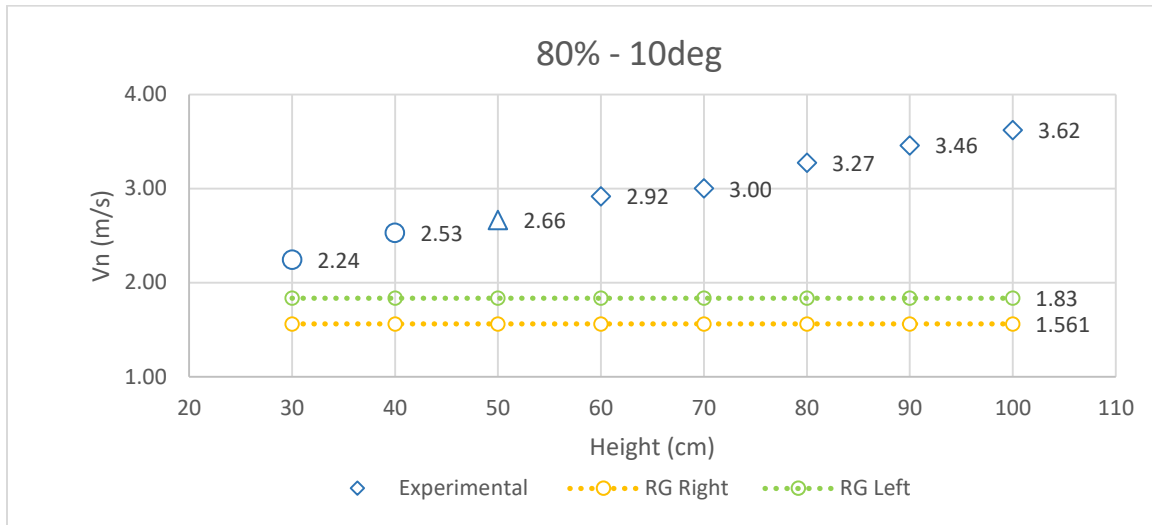
**Figure 5-26: Riboux-Gordillo velocity thresholds for 60% water-methanol solution at 30 degrees tilt angle.**



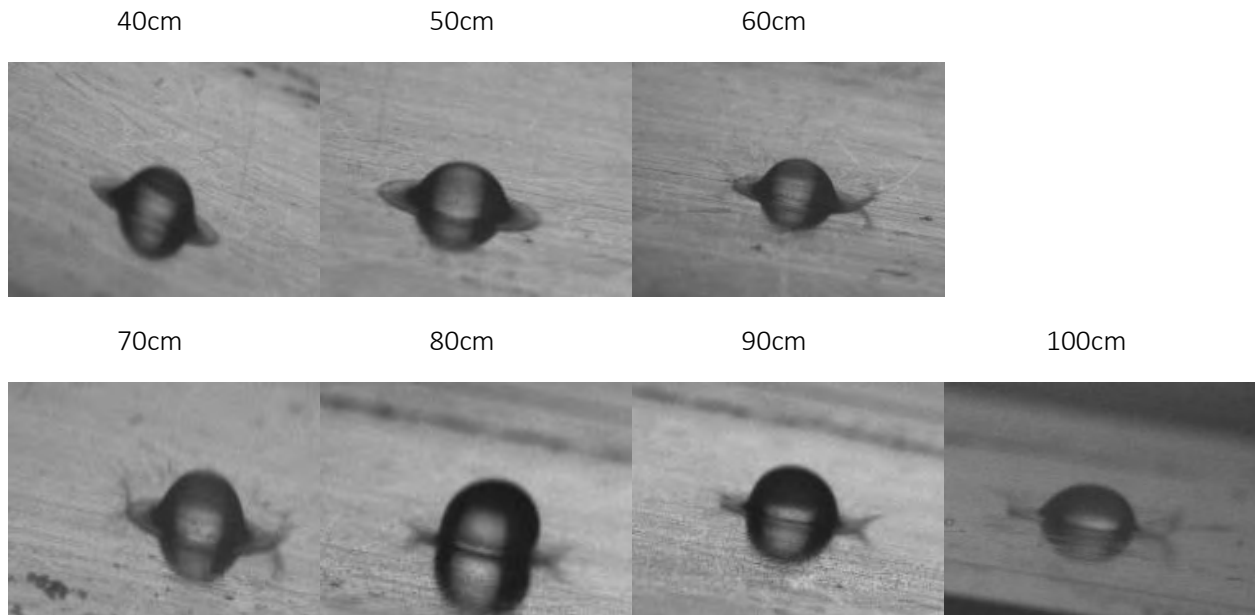
**Figure 5-27: 60% w/w methanol solution at 30 degrees tilt angle**

At 30degrees inclination, threshold velocities are 2.12m/s and 1.358m/s at the upslope and at the downslope side respectively. Lowest measured velocity for this solution is 1.82m/s (at 30cm height), which falls between the two thresholds, so corona splashing on the downslope side is anticipated. In the experimental image for 30cm, no splashing is visible which leaves us with 0.3m/s deviation. Furthermore, due to very bright lighting, left side splashing is hardly visible from 60cm and below, so we also assume no splashing for these heights. As a result, maximum deviation, equal to 0.39m/s, occurs (for upslope side splashing) at 60cm.

For the duration and the size of the splashing is applicable the trend which was met at 40% solution.



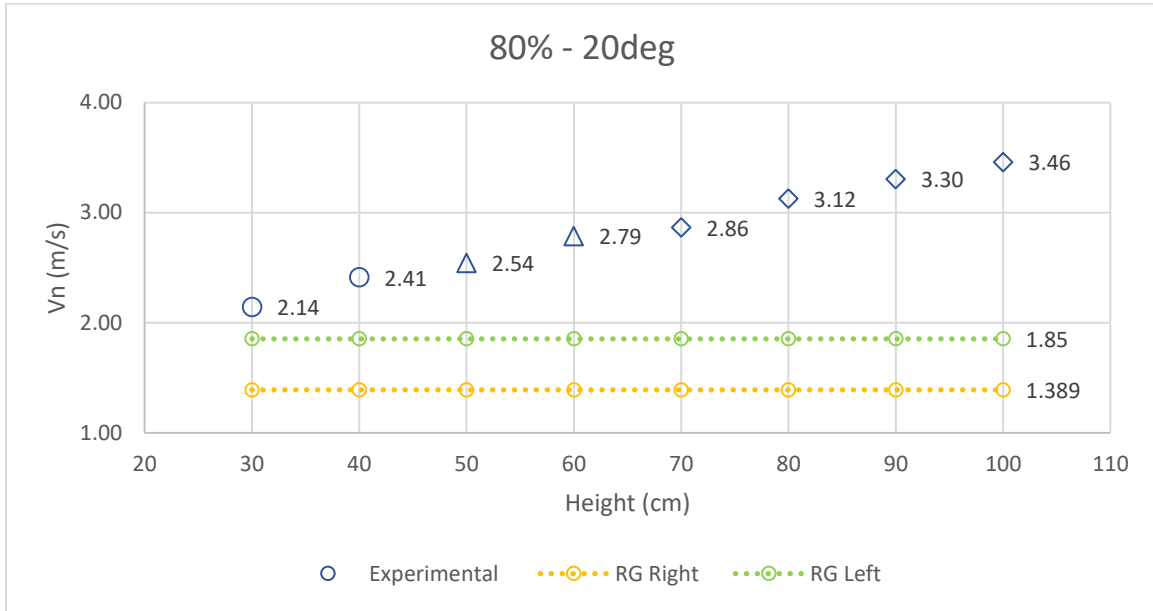
**Figure 5-28: Riboux-Gordillo velocity thresholds for 80% water-methanol solution at 10 degrees tilt angle.**



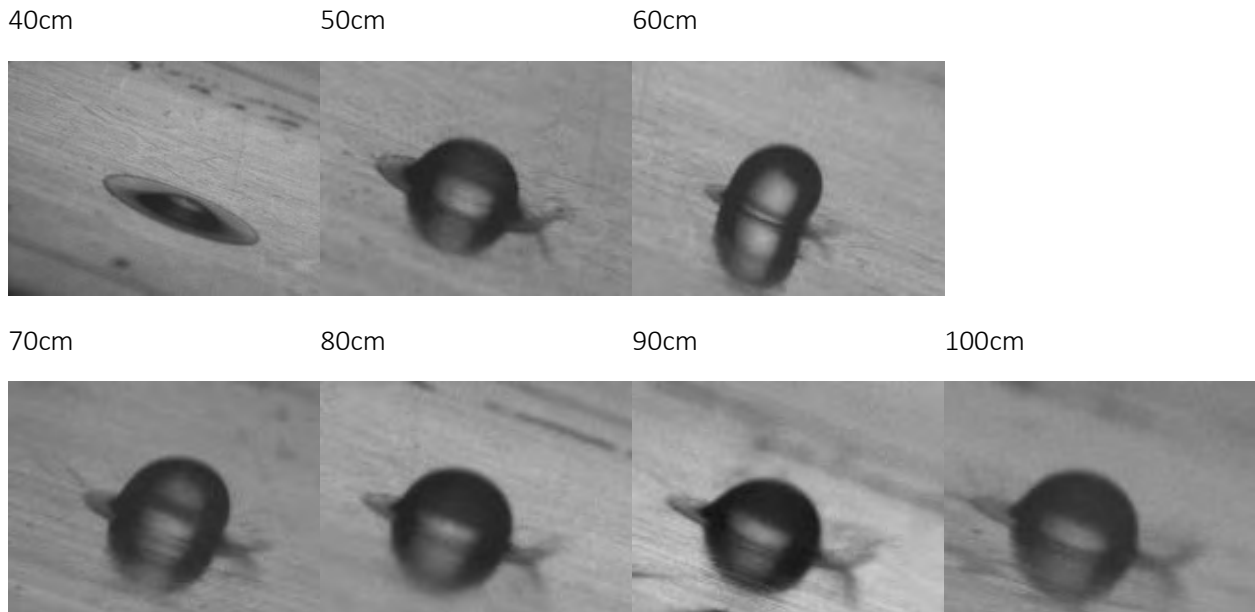
**Figure 5-29: 80% w/w methanol solution at 10 degrees tilt angle**

According to RG model, for 80% w/w water-methanol solution and 10 degrees inclination, corona splashing should occur above 1.83m/s (at the upslope) and 1.561m/s (downslope). Lowest measured velocity during the experiments for this solution is 2.24m/s when the falling distance is set at 30cm, so corona splashing is expected on both sides for all the measured heights. Firstly, when referring to downslope splashing, photograph for 50cm is the last in which we can distinguish some remains of the thin sheet. At 40cm no splashing is visible. This leads to a notable

deviation of almost 1m/s (0.97m/s). Left side splashing stops being visible from 50 cm and below which also results to a 0.83 m/s deviation.



**Figure 5-30: Riboux-Gordillo velocity thresholds for 80% water-methanol solution at 20 degrees tilt angle.**

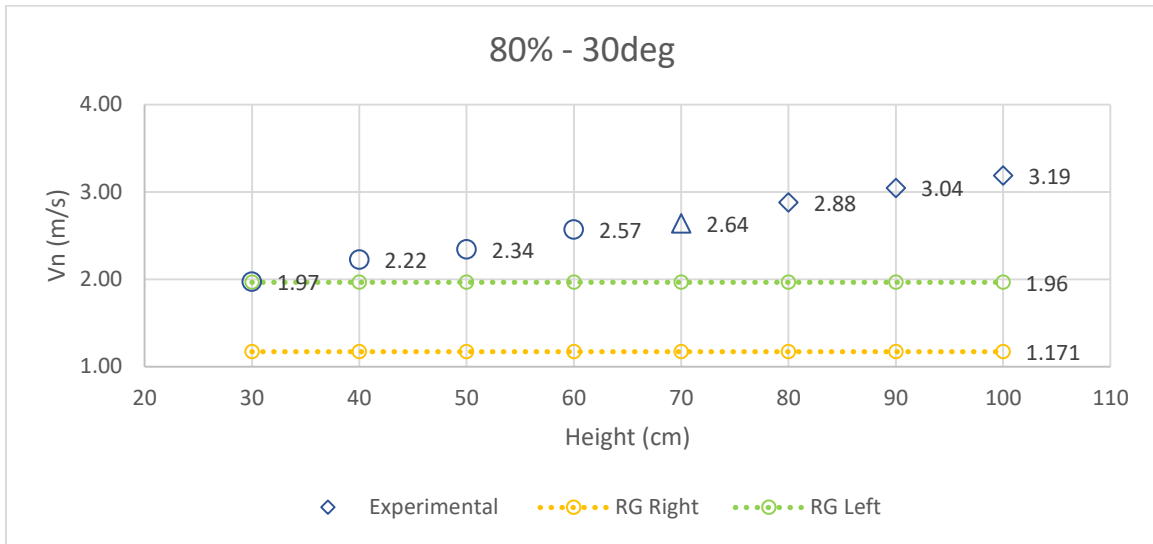


**Figure 5-31: 80% w/w methanol solution at 20 degrees tilt angle**

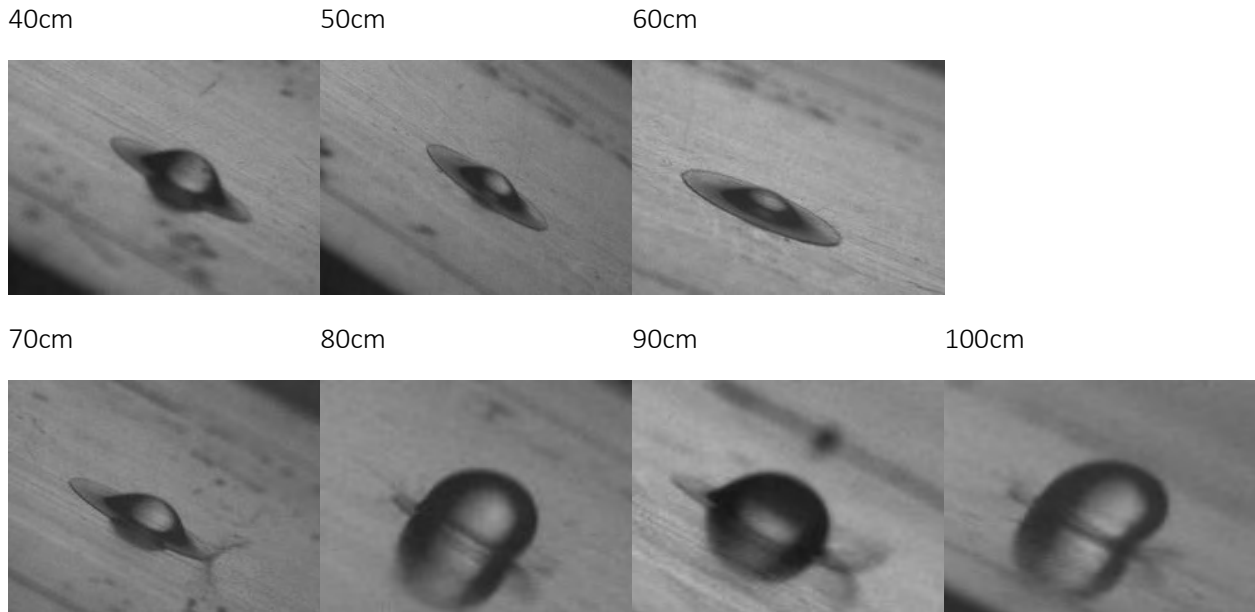
At 20deg inclination threshold velocities are equal to 1.85 and 1.389m/s for the upslope and the downslope side respectively. The lower measured velocity at 30 cm is 2.14 m/s. So, RG criterion proposes splashing on both sides at all times. In the experimental photographs upslope(left) side splashing stops being visible at 50cm and right side splashing at 40cm (the screenshot at 40cm is



taken at a later stage where the lamella has spread too much, so we can not assume no splashing with confidence). The occurring deviations are 0.94m/s for the left side and 1m/s for right side.



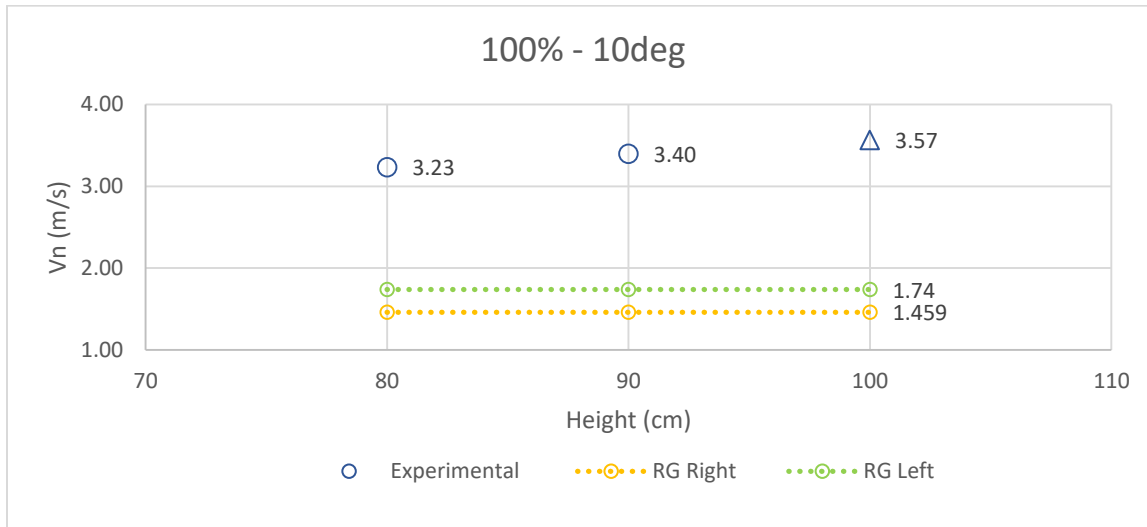
**Figure 5-32: Riboux-Gordillo velocity thresholds for 80% water-methanol solution at 30 degrees tilt angle.**



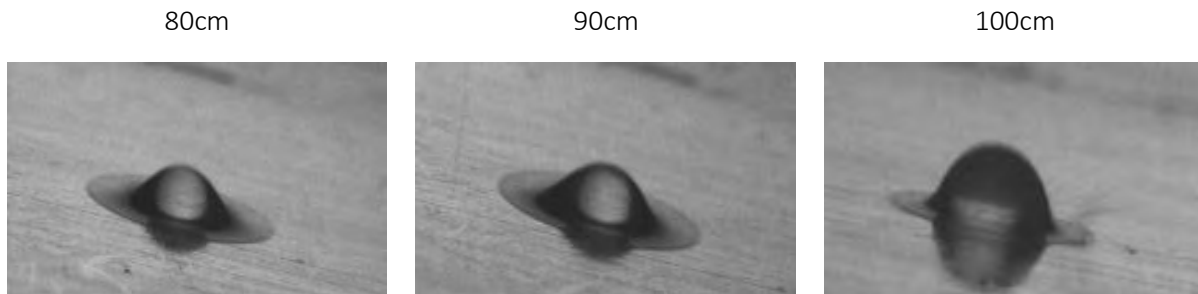
**Figure 5-33: 80% w/w methanol solution at 30 degrees tilt angle**

Finally, at 30 degrees thresholds are 1.96m/s (upslope) and 1.171 (downslope). Lower measured velocity is 1.97 m/s which is borderline for splashing on both sides. In this case according to the photographic material upslope side splashing stops at 70cm (0.68m/s deviation) and downslope splashing at 60 cm (1.4 m/s deviation). Here, it is noted that the available screenshots (40-60cm)

are also taken at a later spreading stage, as in the previous case of 20degrees, and knowing that corona splashing weakens with the decrease of the velocity, its presence is maybe ignored.

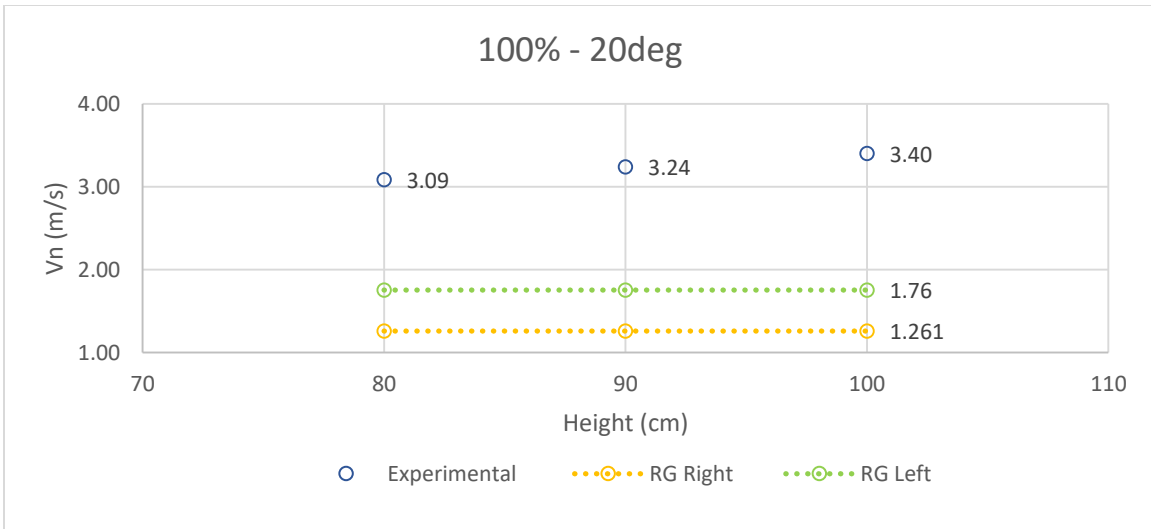


**Figure 5-34: Riboux-Gordillo velocity thresholds for 100% water-methanol solution at 10 degrees tilt angle.**

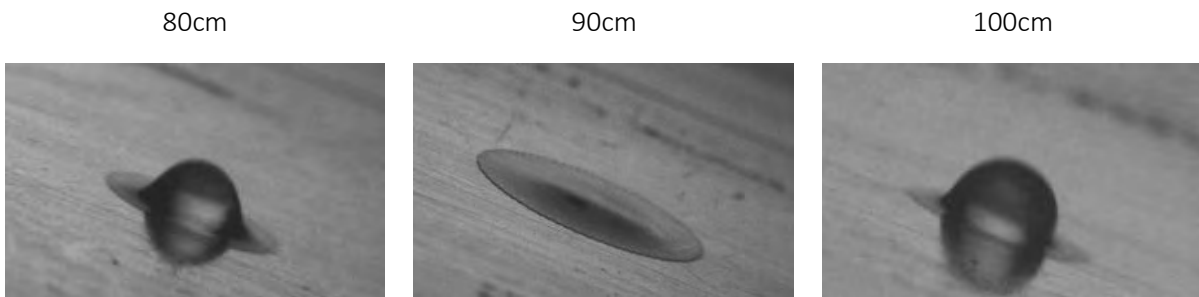


**Figure 5-35: 100% w/w methanol solution at 10 degrees tilt angle**

According to RG model, for 100% w/w water-methanol solution and 10degrees inclination, corona splashing should occur above 1.74m/s (upslope) and 1.459m/s (downslope). Lowest measured velocity during the experiments for this solution is 3.23m/s when the falling distance is set at 30cm and corona splashing is expected at both sides at all times. However, in this case the background of the images is quite blurry and the shooting angle not the best for distinguishing the splashing. As a result, we have a 1.94m/s deviation for the downslope side and a 1.83m/s for the upslope.

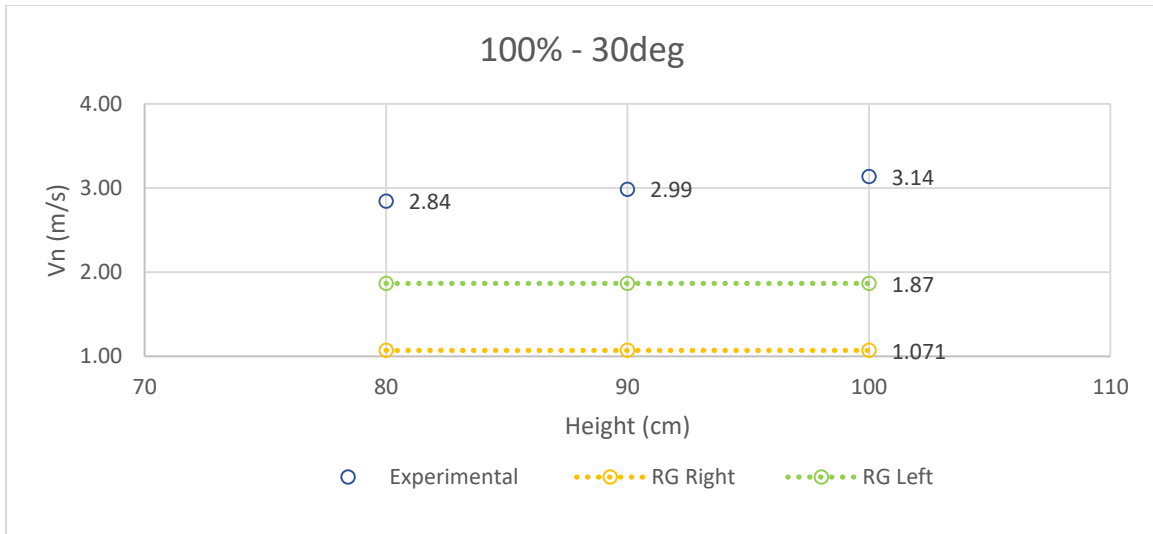


**Figure 5-36: Riboux-Gordillo velocity thresholds for 100% water-methanol solution at 20 degrees tilt angle.**

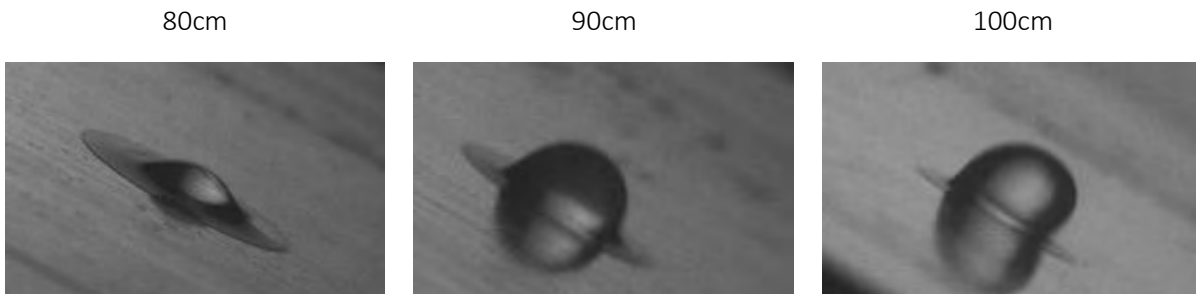


**Figure 5-37: 100% w/w methanol solution at 20 degrees tilt angle**

At 20 degrees also no splashing is visible via the available screenshots and furthermore at 90cm the droplet has already spread; earlier image capture is needed.

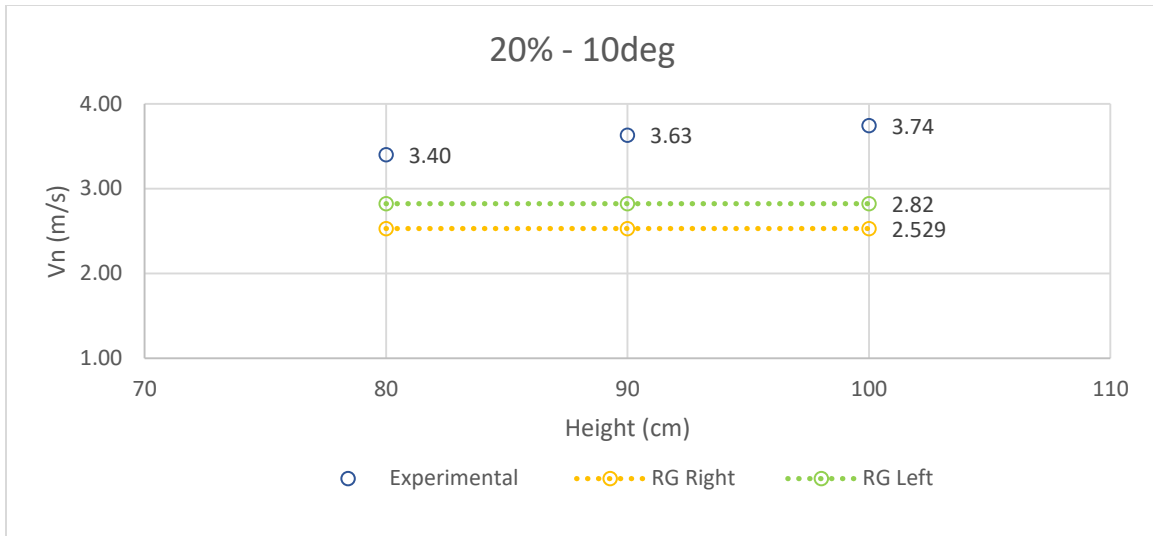


**Figure 5-38: Riboux-Gordillo velocity thresholds for 100% water-methanol solution at 30 degrees tilt angle.**

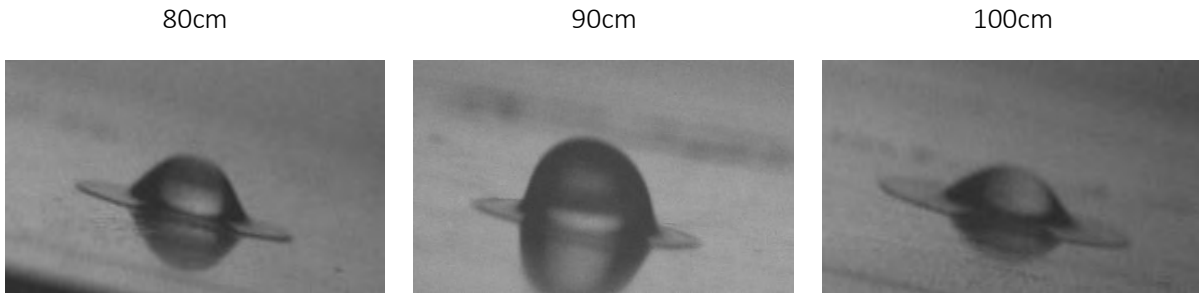


**Figure 5-39: 100% w/w methanol solution at 20 degrees tilt angle**

After examining all three inclinations for the 100% water-methanol solution, we can conclude that is the one with the biggest discrepancies concerning corona splash prediction according the RG model. Experimental velocities were measured from 2.85 to 3.57m/s while the highest threshold (for upslope side splashing) was 1.87m/s at 30degrees inclination.

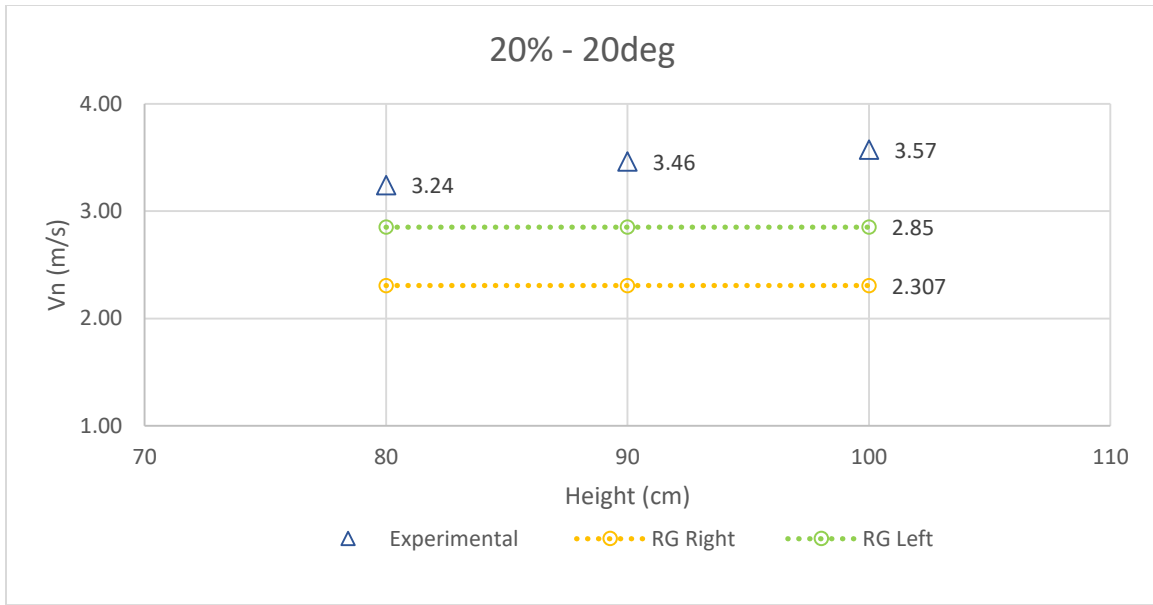


**Figure 5-40: Riboux-Gordillo velocity thresholds for 20% water-methanol solution at 10 degrees tilt angle.**

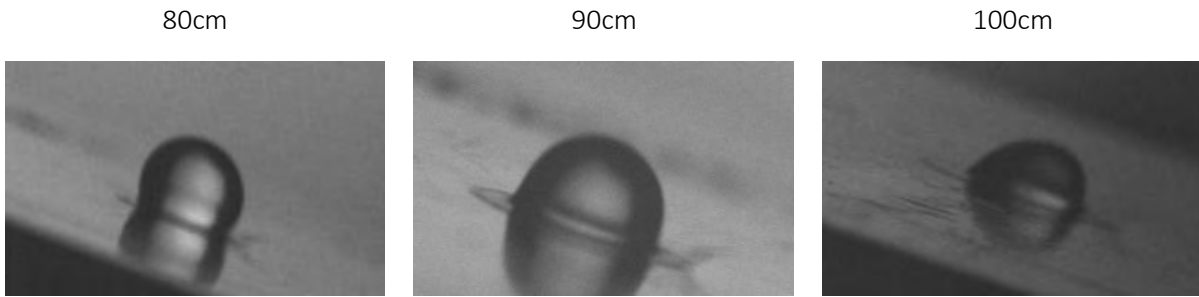


**Figure 5-41: 20% w/w methanol solution at 10 degrees tilt angle**

According to RG model, for 20% w/w water-methanol solution and 10degrees inclination, corona splashing should occur above 2.82m/s (upslope) and 2.53m/s (downslope). Lowest measured velocity during the experiments for this solution is 3.4m/s when the falling distance is set at 80cm and corona splashing is expected at both sides at all times. However, the experimental images prevent the determination of corona splashing remains. Even if corona was formed, it would be much smaller in scale than the one at 40 and 60% solutions. As a result, we have a 1.21m/s deviation for the downslope side and a 0.82m/s for the upslope.

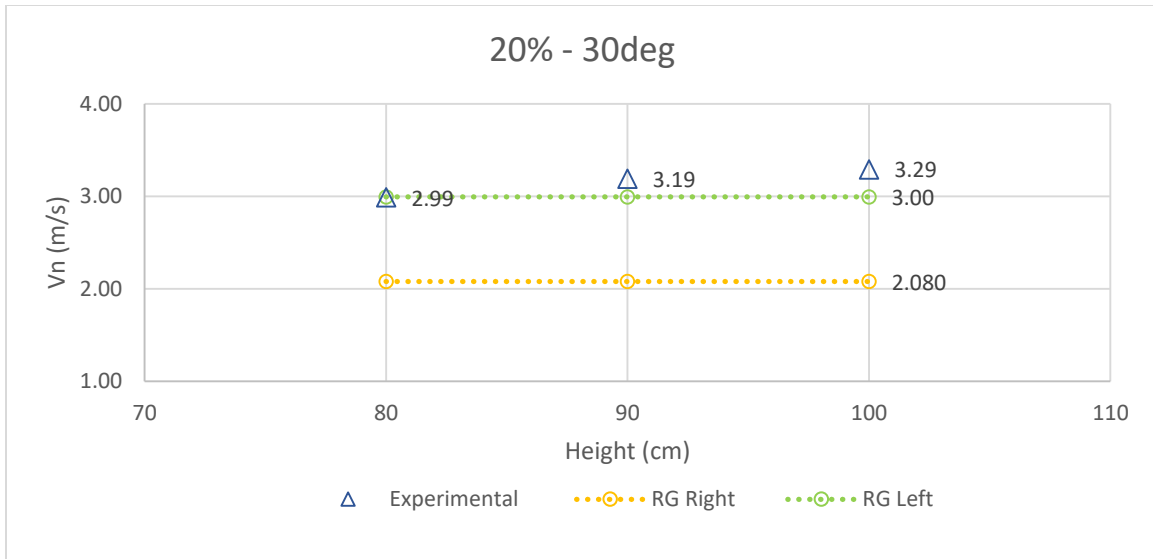


**Figure 5-42: Riboux-Gordillo velocity thresholds for 20% water-methanol solution at 20 degrees tilt angle.**

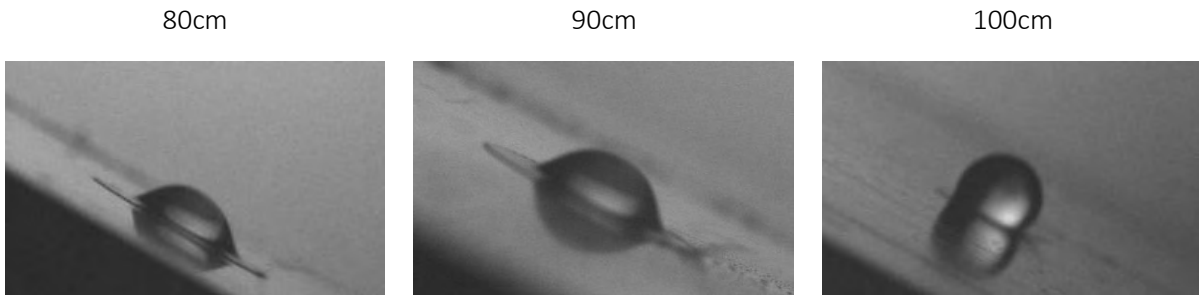


**Figure 5-43: 20% w/w methanol solution at 20 degrees tilt angle**

At 20 degrees inclination triggers splashing on the downslope side. Indeed, RG threshold for the downslope is 2.31m/s and the lowest velocity, at 80cm, is 3.57m/s. Although upslope side threshold (2.85m/s) is also exceeded, in the photographs no splashing is visible which leads to a 0.72m/s deviation.

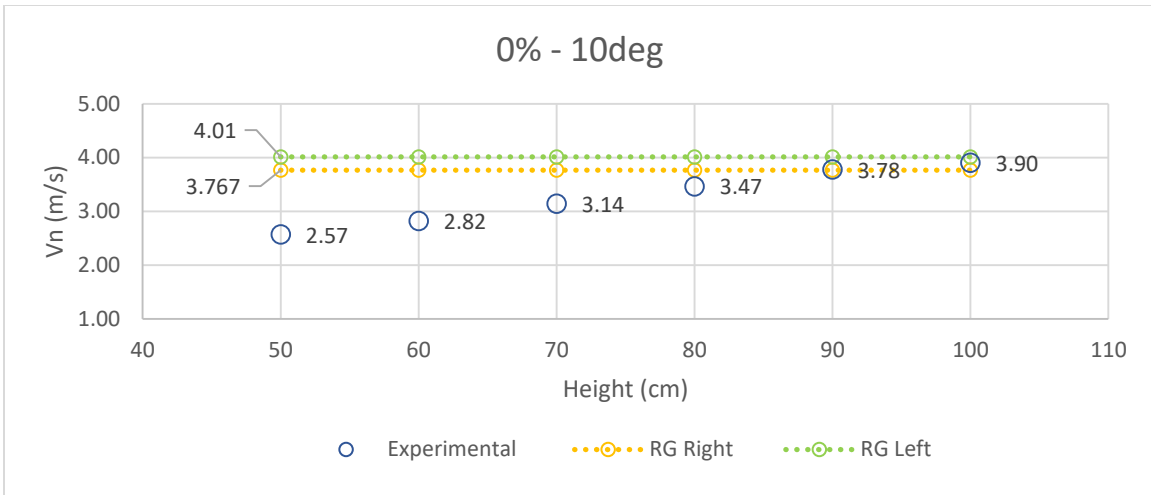


**Figure 5-44: Riboux-Gordillo velocity thresholds for 20% water-methanol solution at 30 degrees tilt angle.**

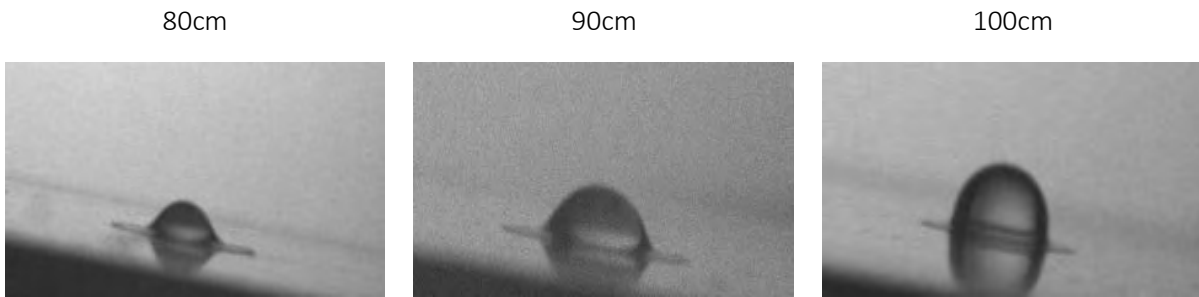


**Figure 5-45: 20% w/w methanol solution at 30 degrees tilt angle**

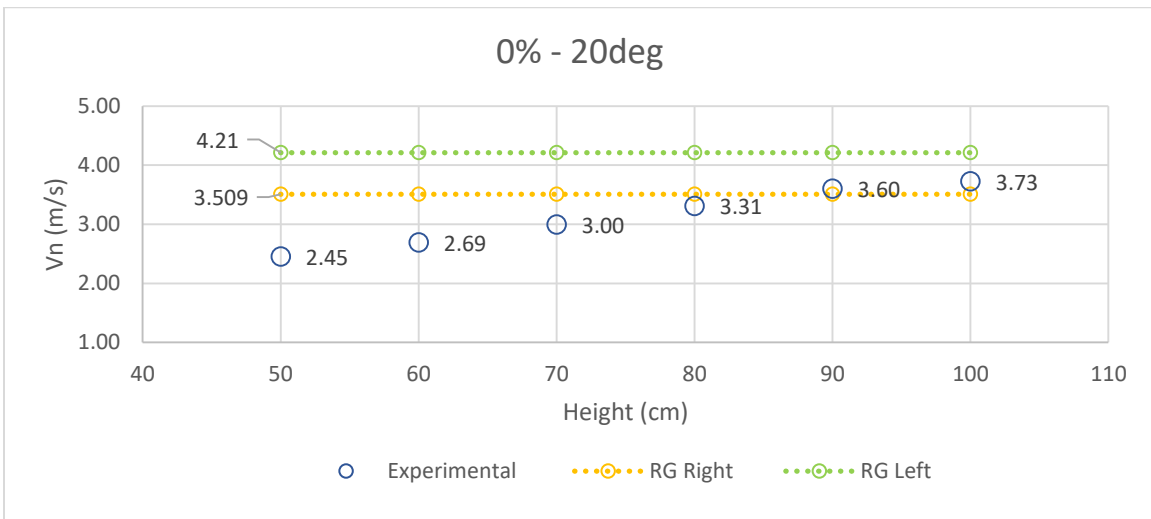
Finally, at 30degrees we can see that the splashing on the right side is further promoted as we can distinguish remains when the drop is half spread on the substrate, not only in the first moments of the impact. The results for left side splashing are similar to 20degrees however with a smaller deviation (0.29m/s).



**Figure 5-46: Riboux-Gordillo velocity thresholds for 0% water-methanol solution at 10 degrees tilt angle.**



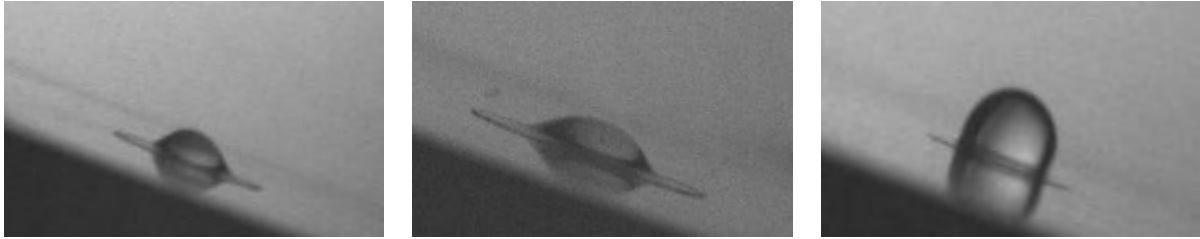
**Figure 5-47: Pure water at 10 degrees tilt angle**



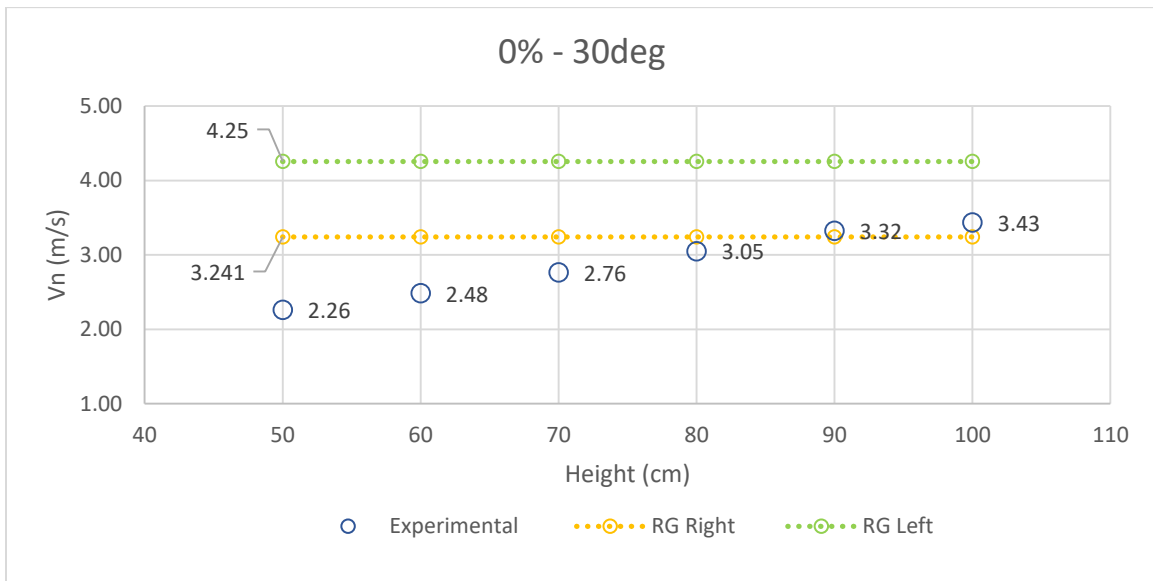
**Figure 5-48: Riboux-Gordillo velocity thresholds for 0% water-methanol solution at 20 degrees tilt angle.**

80cm                      90cm                      100cm

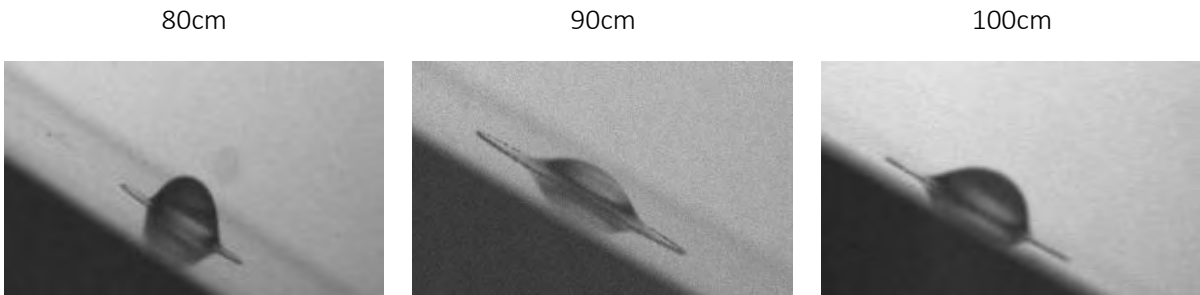




**Figure 5-49: Pure water at 20 degrees tilt angle**



**Figure 5-50: Riboux-Gordillo velocity thresholds for 0% water-methanol solution at 30 degrees tilt angle.**



**Figure 5-51: Pure water at 30 degrees tilt angle**

Distilled water is the liquid which has the most consistent behavior to RG criterion. It is also the only solution which is not supposed to splash. Its terminal velocities at all angles are indeed on borderline of right-side threshold. Water drops are more likely to result in prompt splashing at high velocities.

<i>Right/Downslope Side Splashing Maximum Deviations (%)</i>			
m/s deviation % deviation	10 degrees	20 degrees	30 degrees
0%	0.13 3%	0.22 6%	0.19 5.8%
20%	1.21 48%	0 0	0 0
40%	0 0	0.94 52%	0.46 28.4%
60%	0 0	0.45 29.4%	0.46 33.8%
80%	0.97 62%	1.02 73%	0.8 47%
100%	1.94 133%	2.14 170%	2.07 193%

Table 5.1: Right side velocity deviations in m/s and percentage  $(=(V_{exp}-V_{thr}) * 100 / V_{thr})$ .

<i>Left/Upslope Side Splashing Maximum Deviations (%)</i>			
m/s deviation % deviation	10 degrees	20 degrees	30 degrees
0%	0 0	0 0	0 0
20%	0.92 32.6%	0.72 25%	0.29 9%
40%	0 0	0 0	0 0

<b>60%</b>	0.56 28.3%	0.43 21.5%	0.12 5.6%
<b>80%</b>	0.83 45.4%	0.94 50.8%	0.68 34.7%
<b>100%</b>	1.73 94%	1.64 93.1%	1.27 68%

*Table 5.2: Left side velocity deviations in m/s and percentage  $(=(V_{exp}-V_{thr}) * 100 / V_{thr})$ .*

In summary, the most notable deviations are met at 100% and the 80% solutions, distilled water complies best with the criterion while 20, 40, 60% solutions show approximately 30% deviations. We have to keep in mind that the deviation percentages appear quite major due to the fact that velocities are not very high, that is why in the above tables we also cite the deviation in m/s. In addition, left side results were closer than the ones for the right side. These discrepancies can be related to following reasons:

1. The RG model cannot be 100% accurate,
2. There is experimental uncertainty concerning the identification of the corona thin liquid sheet,
3. There is also some uncertainty concerning the measured drop velocity.

As a result, we can conclude that critical velocity criterion of Riboux and Gordillo for oblique surfaces can be compatible with our experimental results for water splashing and with some exemptions for 20, 40 and 60% solutions. However, the predictions were not compatible with our measurements for 80% solution and pure methanol.

## 5.3 Spreading Lamella

In this section the investigated parameter is the spreading diameter of the droplet, upon impacting on the substrate.

### 5.3.1 Temporal evolution for different solutions and inclinations

Firstly, we compared the results for a fixed height (99cm, 89cm, and 79cm), tilt angle (0, 10, 20 and 30 degrees) and surface roughness (smooth, coarse) in order to determine whether the spreading lamella behavior varies from each water-methanol solution to another. The diagrams display the diameter, in terms of the non-dimensional one  $D_{ND} = D_t/D_0$ , plotted with normal time. Placed in groups of four, concerning separately each substrate and each height for the different inclinations of the substrate. Kinematic viscosity  $\nu$  was used as a further measure of comparison of the mixtures ( **Table 5.3**). The evolution of the diameter is illustrated for each liquid mixture, the general trends and differences between them are evidenced and the maximum spreading diameter  $\beta$  is determined.

Kinematic viscosity ( $=\mu/\rho$ ) [m <sup>2</sup> /s]	
0%	0.0000010
20%	0.0000013
40%	0.0000015
60%	0.0000014
80%	0.0000011
100%	0.0000006

**Table 5.3: Kinematic viscosity for the solutions**

#### A. Smooth Aluminum Substrate (0.45 $\mu$ m)

##### o 99cm (Flat,10, 20, 30 degrees)

A relation between spreading diameter and dynamic viscosity can be identified. The present trend (**Figure 5-52, Figure 5-53**) is that the pure methanol mixture which has the lowest dynamic viscosity and surface tension values of all mixtures is the one with the highest spreading diameter. Pure water and 80% that present also relatively small viscosity values follow up pure methanol in diameter values. In contrary, the 40% methanol mixture whose viscosity value is the highest, is the one that spreads the less. Mixtures with in-between viscosity values are in the middle of the spreading diameter scale. This phenomenon can be further explained by comparing the kinematic viscosity for all the mixtures. The one with the lowest  $\nu$  and highest Re number is pure methanol which spreads the most, independently of inclination, while the 20%, 40% and 60% mixtures that spread the least, present higher  $\nu$  values compared to 80% methanol. The only mixture whose behavior doesn't apply to this trend is the pure water. Its  $\nu$  values is one of the lowest but for

inclined substrates, its spreading appears to become smaller, especially at 30 degrees where the spreading diameter is on the level of the 20%, 40% and 60% mixtures.

Considering the inclination of the substrate, the pure methanol liquid exhibits the greatest spreading for all the cases. As the inclination gets bigger the spreading diameter tends to increase. The mixtures display their highest spreading for the 30° tilted surface. For example the 80% w/w methanol mixture reaches  $D_{nd} = 6$  for inclination of 0 and 10 degrees,  $D_{nd} = 6.2$  for 20 degrees and  $D_{nd} = 6.7$  for 30 degrees. The exception in this behavior is pure water (0%) in which as the inclination increases the spreading appears to decrease ( $D_{nd} = 6.6$  for horizontal substrate and  $D_{nd} = 5.8$  for 30 degrees inclined).

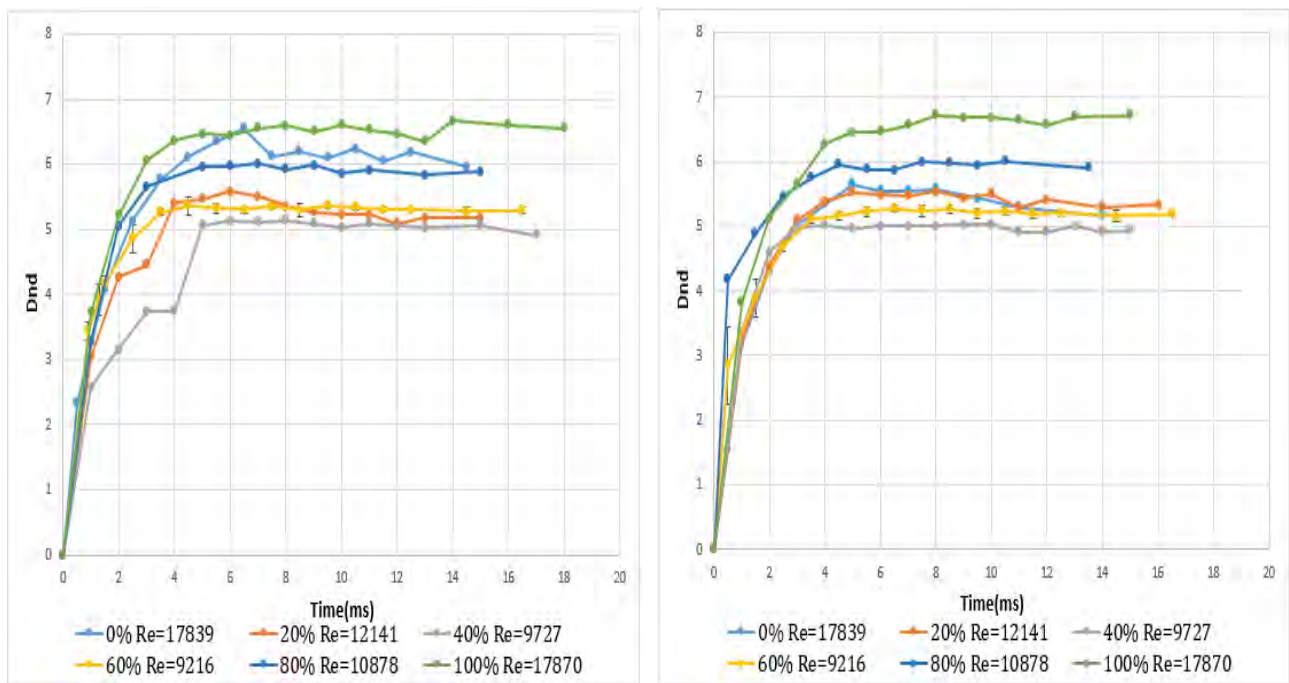


Figure 5-52: Spreading diameter evolution for horizontal and 10° inclined substrate,  $H=0.99m$ ,  $Ra=0.45\mu m$

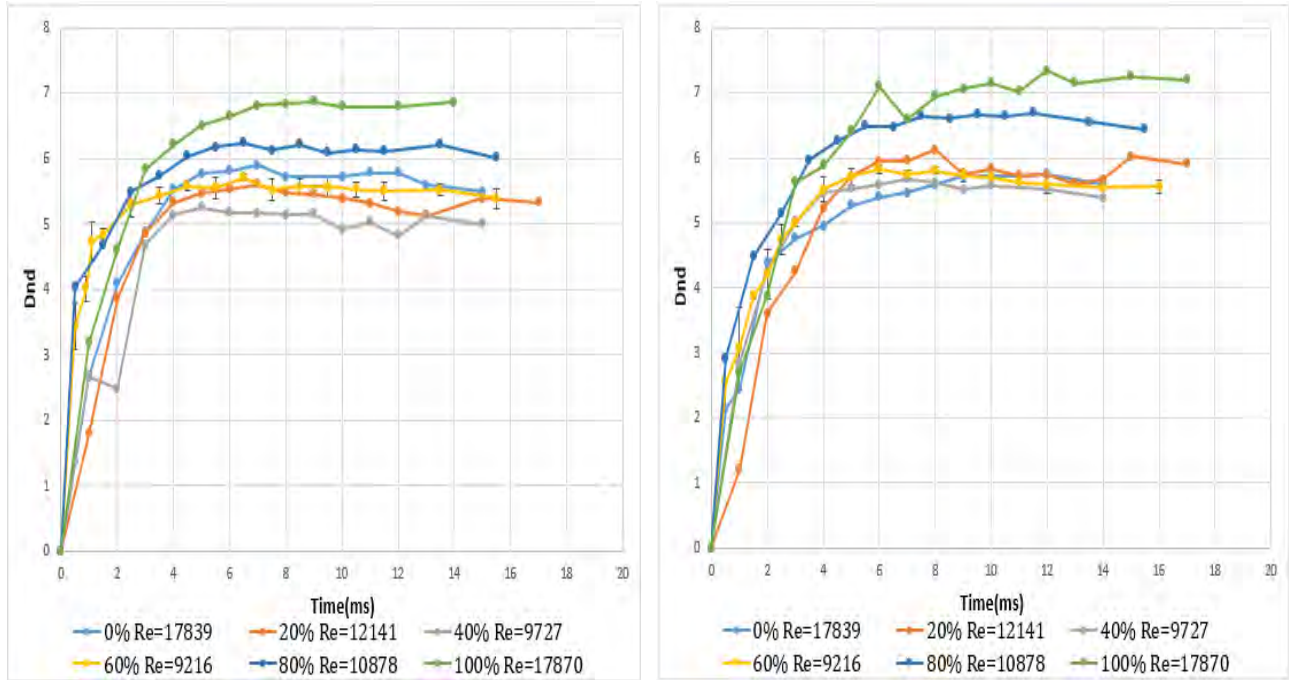


Figure 5-53: Spreading diameter evolution for 20° and 30° inclined substrate,  $H=0.99m$ ,  $Ra=0.45\mu m$

o 89cm (Flat,10, 20, 30 degrees)

The relation between the spreading diameter and the kinematic viscosity remains dominant and independent of the substrate inclination also for these Weber numbers (Figure 5-54, Figure 5-55). The mixture with the lowest kinematic viscosity (pure methanol), ( Table 5.3) spreads the most and the mixture with the greatest (40% methanol) spreads the least. In this case pure water appears to confirm the kinematic viscosity hypothesis.

As the substrate inclination increases the spreading tends to become greater for all the mixtures including this time the pure water ( $Dnd=6.1$  for horizontal,  $Dnd=6.2$  at 10 degrees and 20degrees and  $Dnd=6.4$  at 30 degrees).

Pure water (0%) appears to spread faster with respect to time compared with the other mixtures and also presents a recoiling tendency for the horizontal and 10 degrees inclined substrate after about 8 msec. The recoiling doesn't appear for the other mixtures that attain their maximum spreading diameter  $\beta$  and then present relative stability.

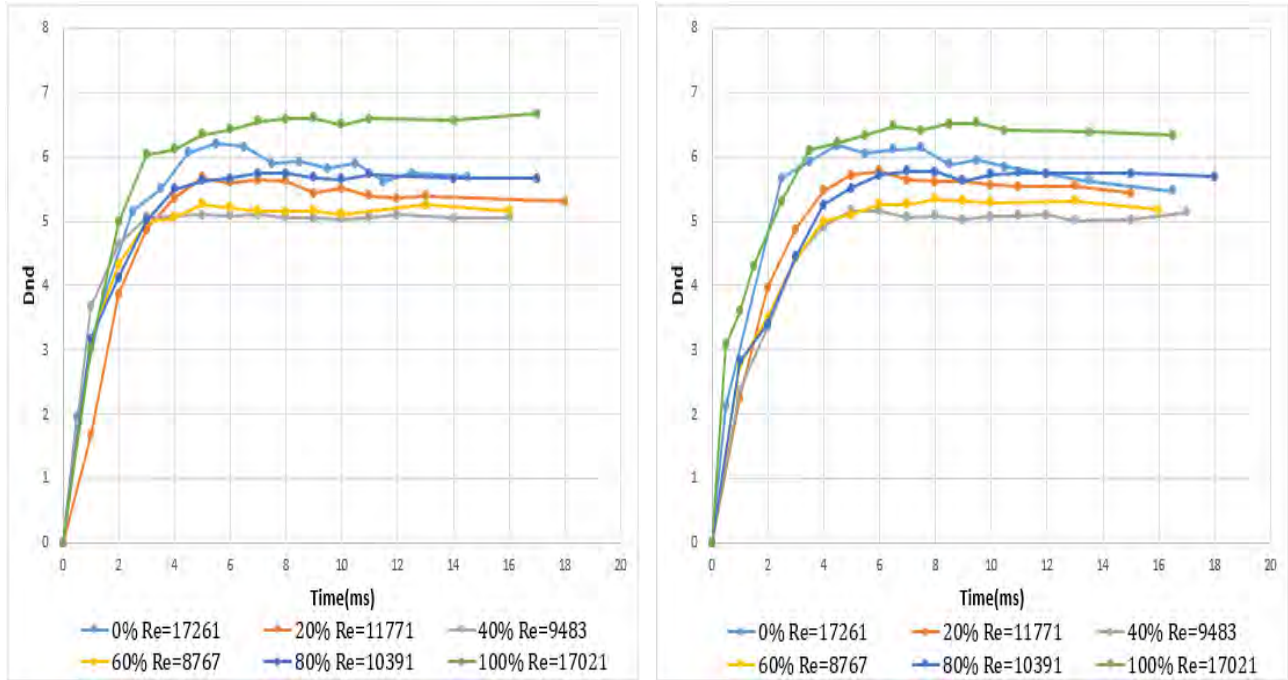


Figure 5-54: Spreading diameter evolution for horizontal and 10° inclined substrate,  $H=0.89m$ ,  $Ra=0.45\mu m$

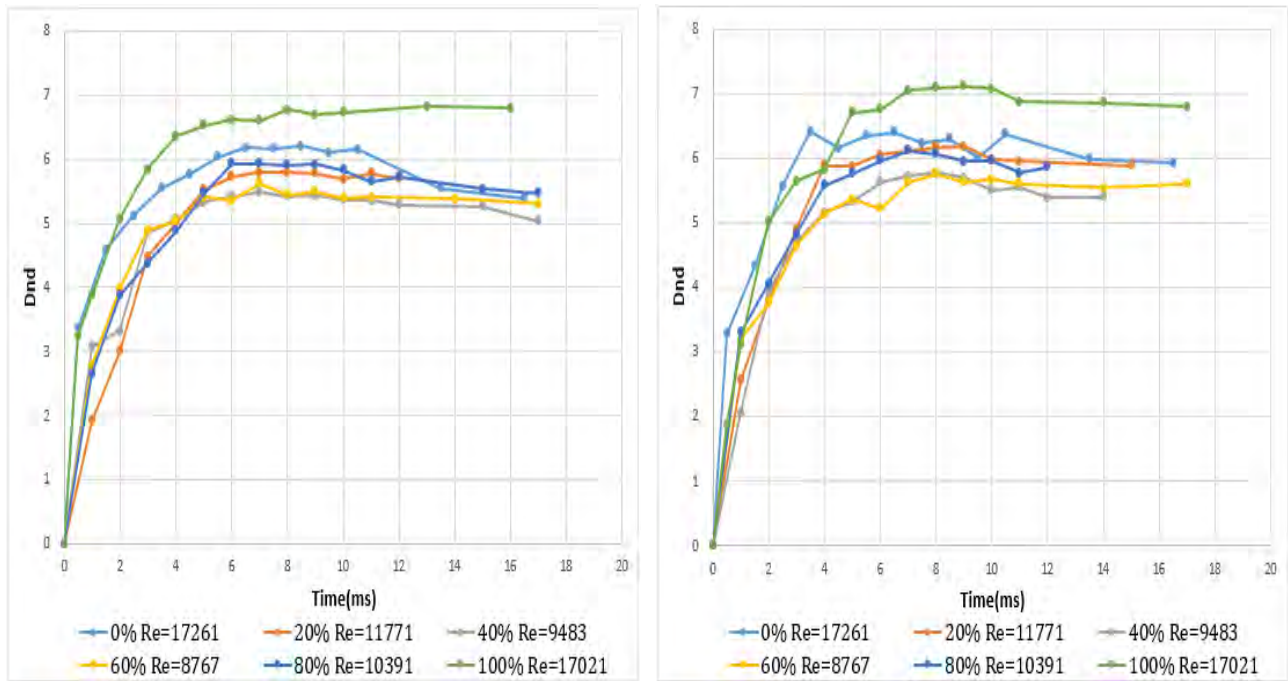
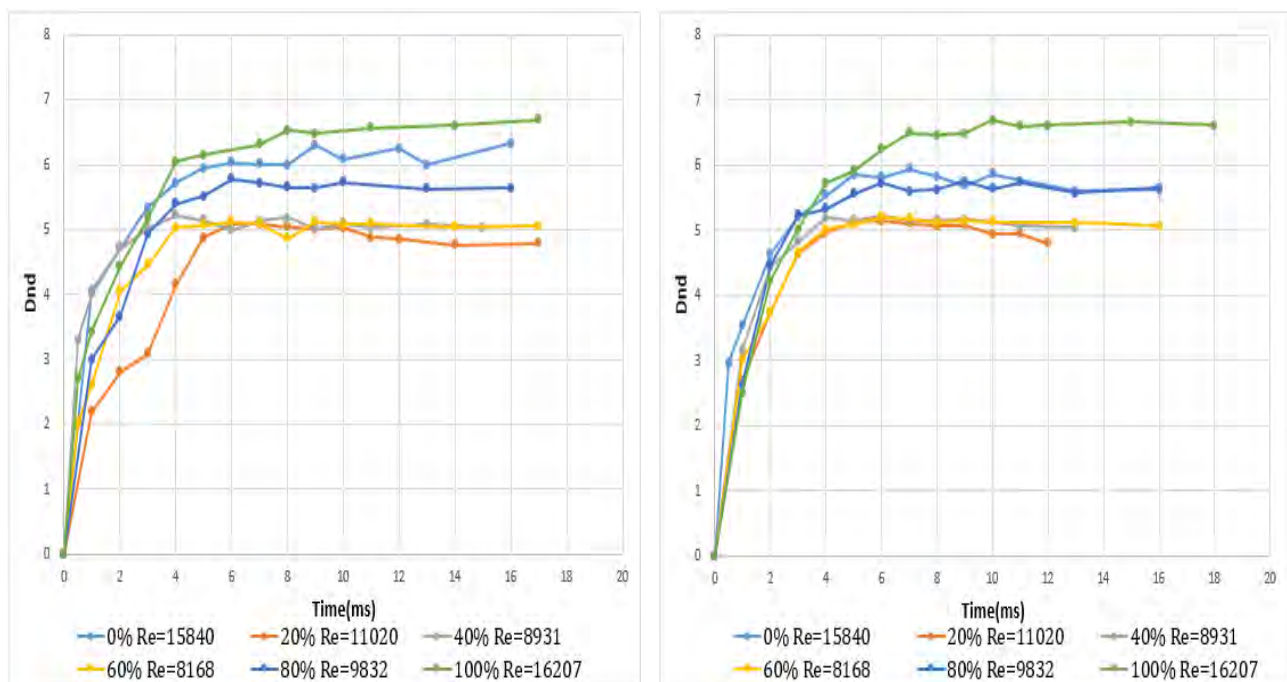


Figure 5-55: Spreading diameter evolution for 20° and 30° inclined substrate,  $H=0.89m$ ,  $Ra=0.45\mu m$

- 79cm (Flat, 10, 20, 30 degrees)

For these Re numbers, ( **Figure 5-56,Figure 5-57**) the 20% mixture is the one that displays the lowest diameter values, while the pure methanol is the one that spreads the most, followed by pure water and 80% w/w methanol. The fact that 80% mixture spreads more than the 20% although having a lower Re number is compensated by the fact that the droplets diameter for 80% is lower than for 20%, although  $\nu$  is lower.

Higher inclination results in higher spreading values for all the mixtures except pure water (0%). For example, at 30 degrees the pure methanol attains a  $\beta$  of 7.1 Dnd, at 20 degree a  $\beta$  of 6.8 Dnd at 10 and 0 degrees of about 6.7 Dnd. Likewise, the 20% methanol mixture attains  $\beta$  of 5.3 Dnd, 5.2 Dnd, 5.1 Dnd and 5.1 Dnd for 30, 20, 10 and 0 degrees respectively. This trend is not dominant in pure water where  $\beta$  is 6.3Dnd for horizontal substrate, a value that exceeds the  $\beta$  at 10, 20 and 30 degrees.



**Figure 5-56: Spreading diameter evolution for horizontal and 10° inclined substrate,  $H=0.79m$ ,  $Ra=0.45\mu m$**



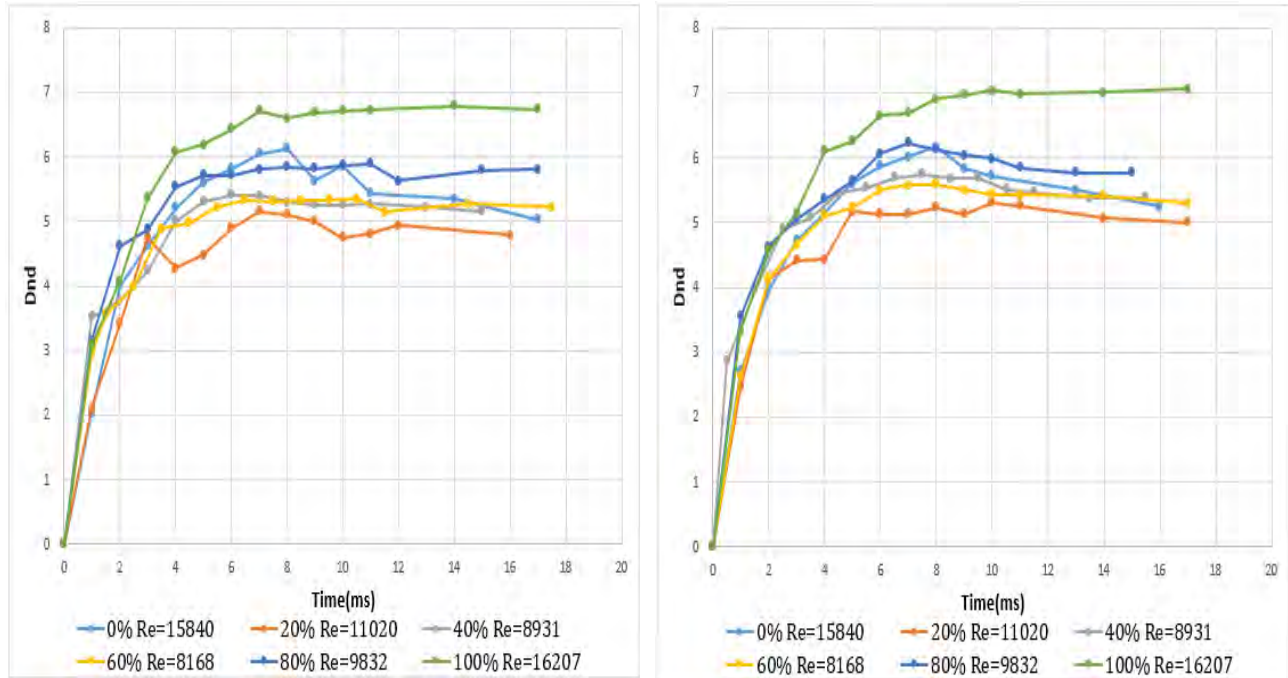


Figure 5-57: Spreading diameter evolution for 20° and 30° inclined substrate,  $H=0.79m$ ,  $Ra=0.45\mu m$

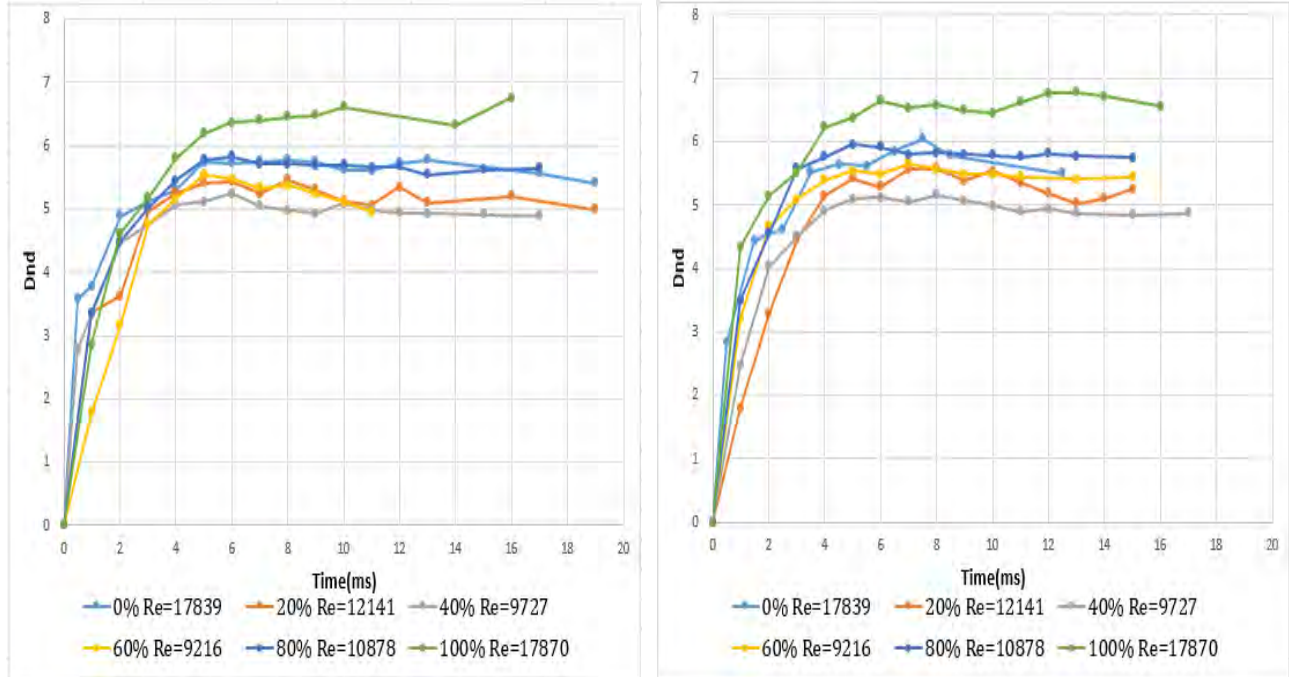
In conclusion, the general trends we can obtain for all the height cases is that as the kinematic viscosity  $\nu$  decreases or the substrate inclination increases the spreading diameter displays an increase. The only liquid that sometimes deviates from this behavior is pure water.

## B. P24 Substrate ( $Ra=4.3\mu m$ )

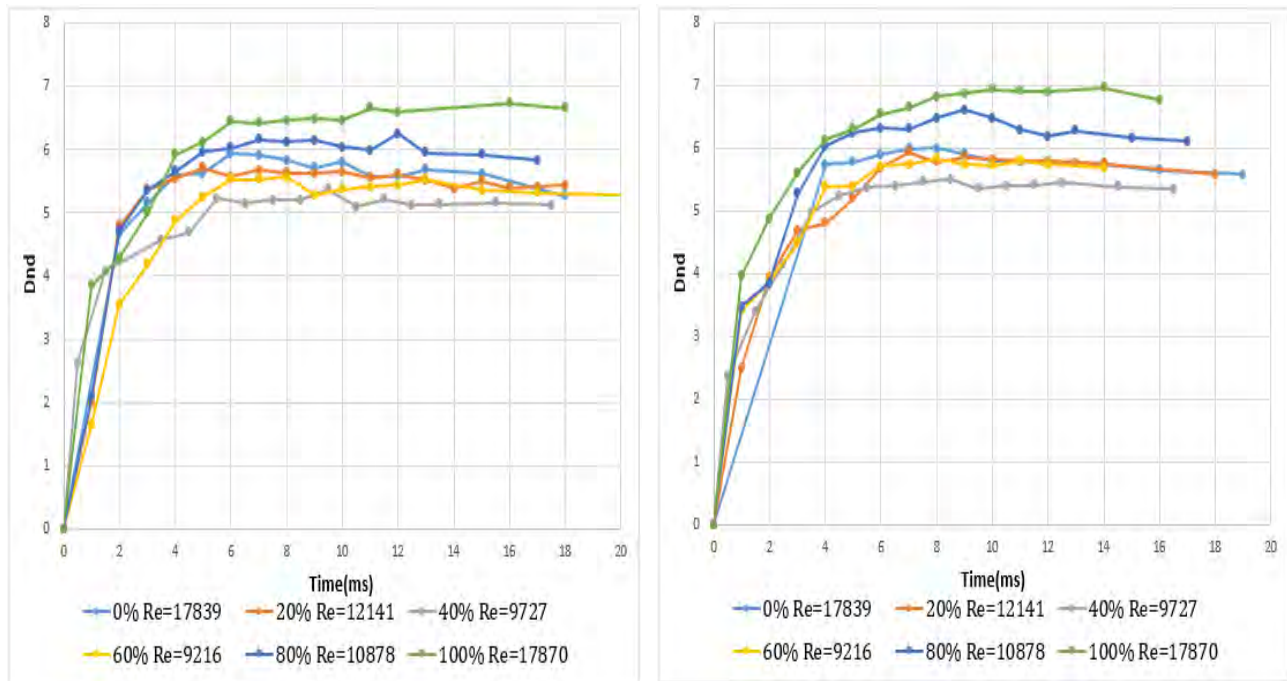
### o 99cm(Flat,10, 20, 30 degrees)

Pure methanol displays the highest values for the case of impact on the rough surface from a height of 99cm. This observation is valid independently of the substrate inclination. This liquid is the one that presents the lowest  $\nu$  values out of all ( **Table 5.3**). On the other side, the solution of 40% w/w methanol which has the highest  $\nu$ , is the one that attains the lowest spreading values. In general as the kinematic viscosity increases, the spreading tends to decrease. Concerning the substrate inclination the advancing lamella appears to spread more with respect to higher substrate angles. All the liquids attain their highest  $\beta$  value at the 30 degrees case. However the advance of  $\beta$  with inclination can be more (80%) or less energetic (40%, 60%). For example the 80% w/w methanol solution has  $\beta$  values of 5.8, 6, 6.2 and 6.5 for a flat, 10, 20 and 30 degrees inclined substrate respectively. This increase is lower for the 60% solution where the  $\beta$  values for flat, 10, 20 and 30 degrees are 5.6, 5.7, 5.6 and 5.8 respectively. About 6 ms after impact the majority of mixture-substrate interactions seem to reach a diameter value that doesn't change greatly for the next ms of the experiment. Therefore some cases present a recoiling tendency. For example pure water for 10 degrees inclination attains its  $\beta=6$  at 7.5ms

and then at 12.5 ms the  $D_{nd}$  recedes to 5.5. The recoiling possibly has to do with the effects of surface tension. Surface tension, which for pure water is about 0.0728 N/m and greater than for the other solutions, tends to affect the spreading phenomenon at its latter stage (R Rioboo et al., 2002).



**Figure 5-58: Spreading diameter evolution for horizontal and 10° inclined substrate,  $H=0.99m$ ,  $Ra=4.3\mu m$**



**Figure 5-59: Spreading diameter evolution for 20° and 30° inclined substrate,  $H=0.99m$ ,  $Ra=4.3\mu m$**

o 89cm(Flat,10, 20, 30 degrees)

For this height and substrate the solution that spreads the most (greatest  $\beta$  value) is pure methanol for all the inclinations and the one that spreads the least is 60% for flat, 10 and 20 degrees and pure water for 30 degrees. While the behaviour of the 60% w/w methanol is accepted based on the kinematic viscosity hypothesis, the behaviour of pure water deviates. Although its  $\nu$  is the second lower after pure methanol, its spreading diameter is placed on the range of 20%,40% and 60% solutions that present a much higher  $\nu$  values. The inclination effect on the spreading diameter appears weakening. Most mixtures present their highest  $\beta$  at 30 degrees but the behaviour for the other substrate placements doesn't display a specific trend. The general trend for all the solutions is that they attain their  $\beta$  in between 5 and 7 ms after impact. Exceptions are pure methanol and 80% w/w that in most cases continue growing up until 9 and 10msec after impact. Afterwards the recoiling phase initiates in most cases. The Dnd has dropped at an average of 0.3 to 0.4 at the last measurement in comparison with  $\beta$  value.

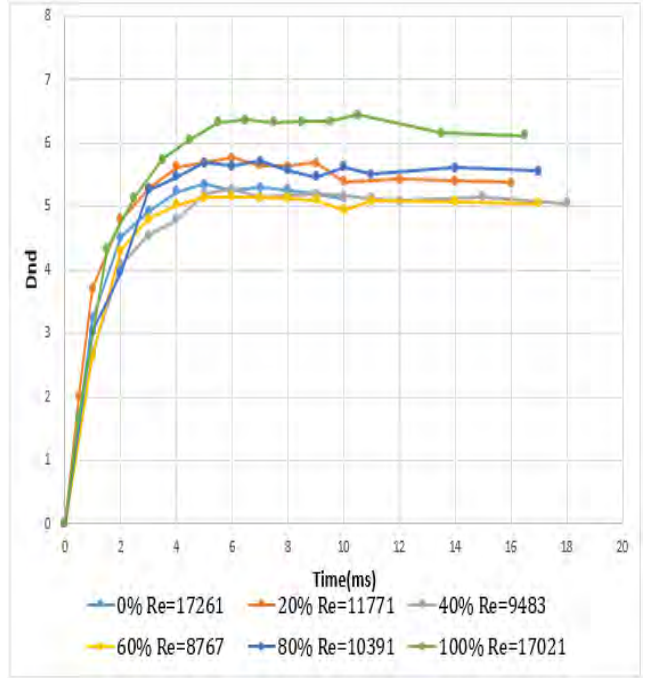
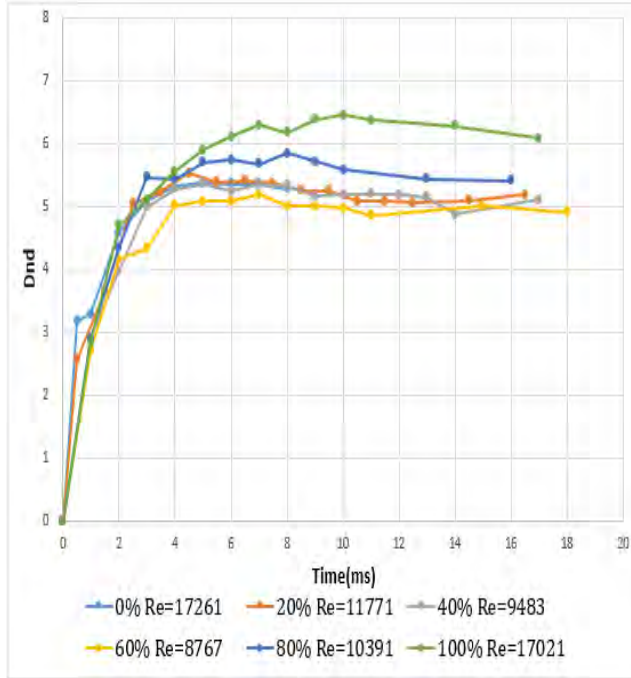


Figure 5-60: Spreading diameter evolution for horizontal and 10° inclined substrate,  $H=0.89m$ ,  $Ra=4.3\mu m$

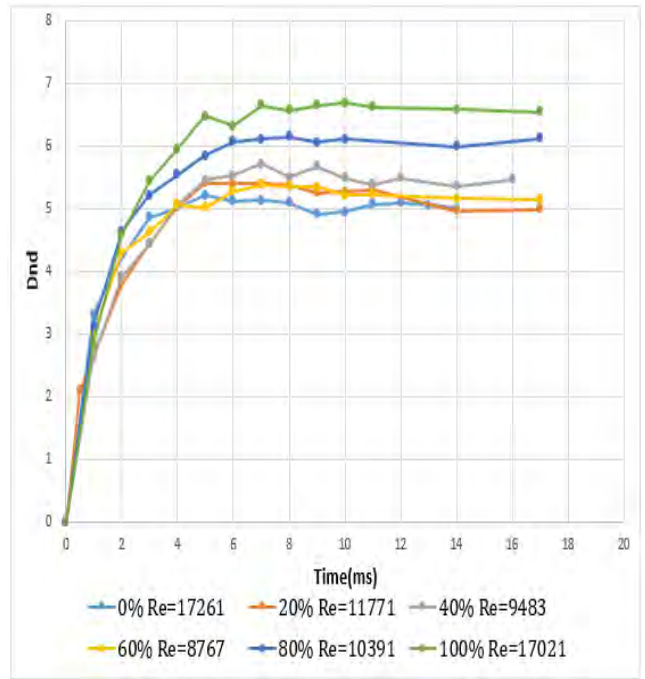
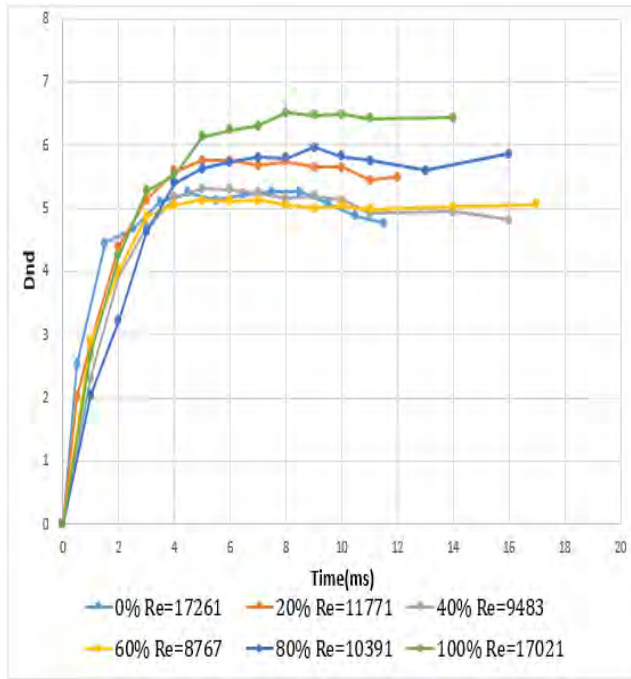


Figure 5-61: Spreading diameter evolution for 20° and 30° inclined substrate,  $H=0.89m$ ,  $Ra=4.3\mu m$

o 79cm(Flat,10, 20, 30 degrees)

Pure methanol and 80% are the ones that display the greatest diameter values and are set apart from the remaining solutions that behave similarly to each other. The effect of advancing substrate inclination on the spreading diameter presents a clear increasing trend for pure methanol with  $\beta$  values of 6.2, 6.4, 6.5 and 7.1 for flat,10,20,30 degrees inclined substrate respectively (**Figure 5-62,Figure 5-63**). A similar trend applies for 80% w/w methanol. The 20% and 40% w/w methanol solutions display higher spreading values only for 30 degrees. In contrary the behaviour of the spreading diameter for pure water and 60% methanol is stable.

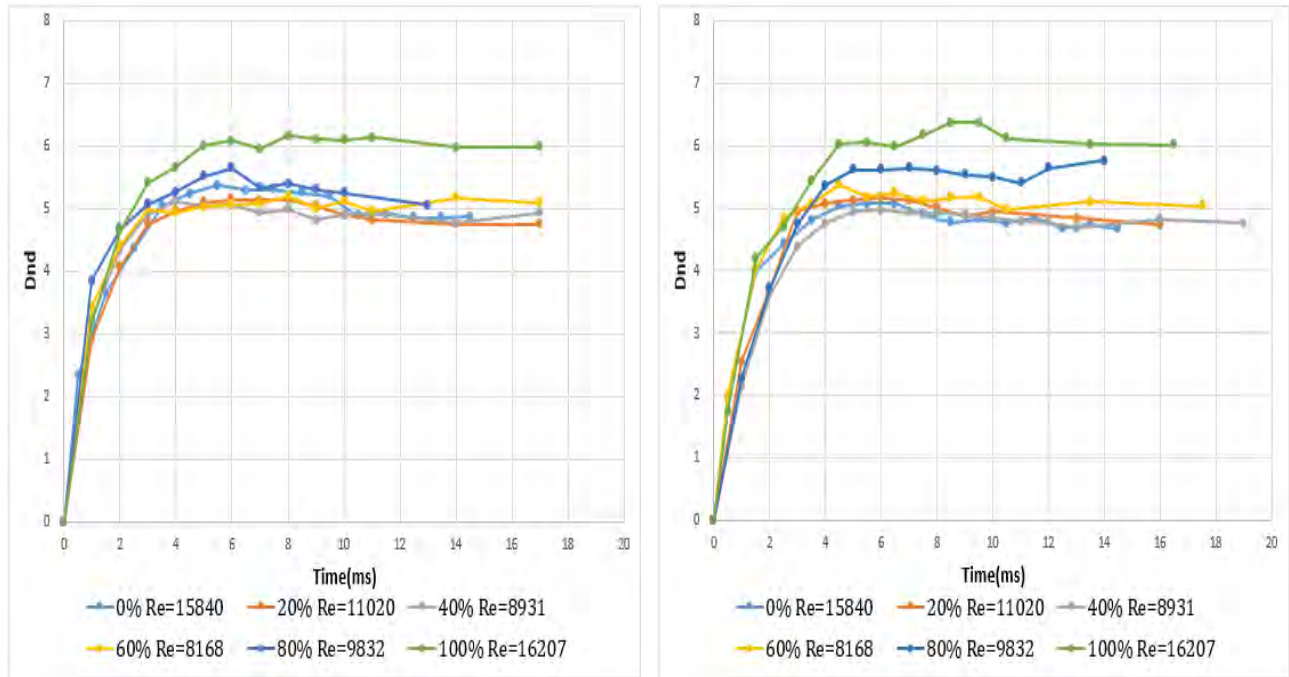


Figure 5-62: Spreading diameter evolution for horizontal and 10° inclined substrate,  $H=0.79m$ ,  $Ra=4.3\mu m$



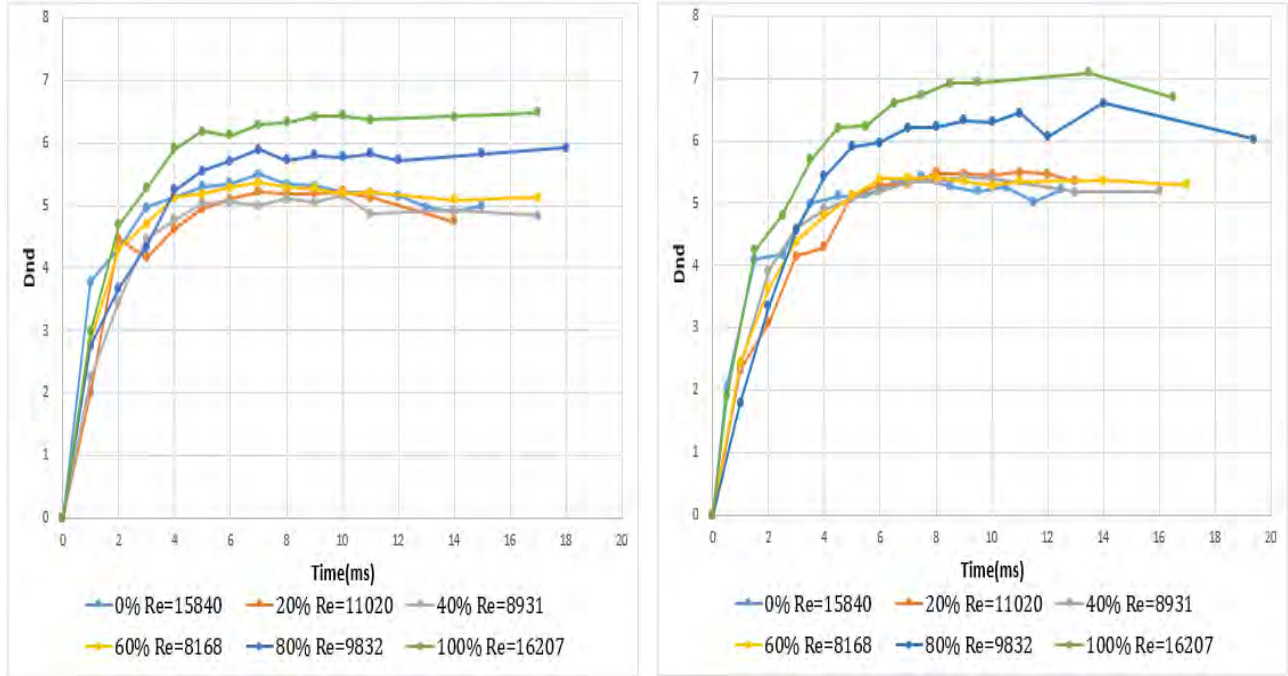


Figure 5-63: Spreading diameter evolution for 20° and 30° inclined substrate,  $H=0.79m$ ,  $Ra=4.3\mu m$

### 5.3.2 Surface Roughness

Secondly, we compared the results for a given water-methanol solution (0%, 20%, 40%, 60%, 80%, 100%) and tilt angle (0, 10, 20 and 30 degrees) in order to determine whether the behavior of the spreading lamella is affected from the surface roughness and the falling distance (the velocity of the impacting drop).

#### A. 0% w/w methanol (distilled water)

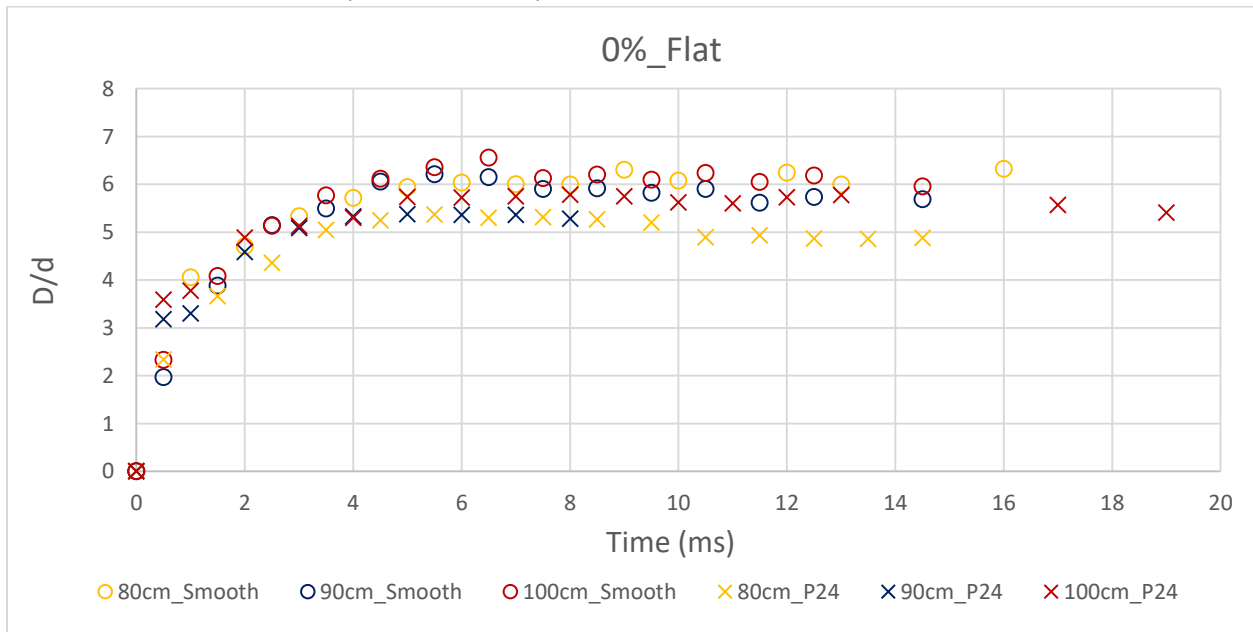


Figure 5-64: 0% w/w methanol solution ( $We=B. 765.89, We=909.43, We=971.39$  for 80, 90 and 100 cm respectively).

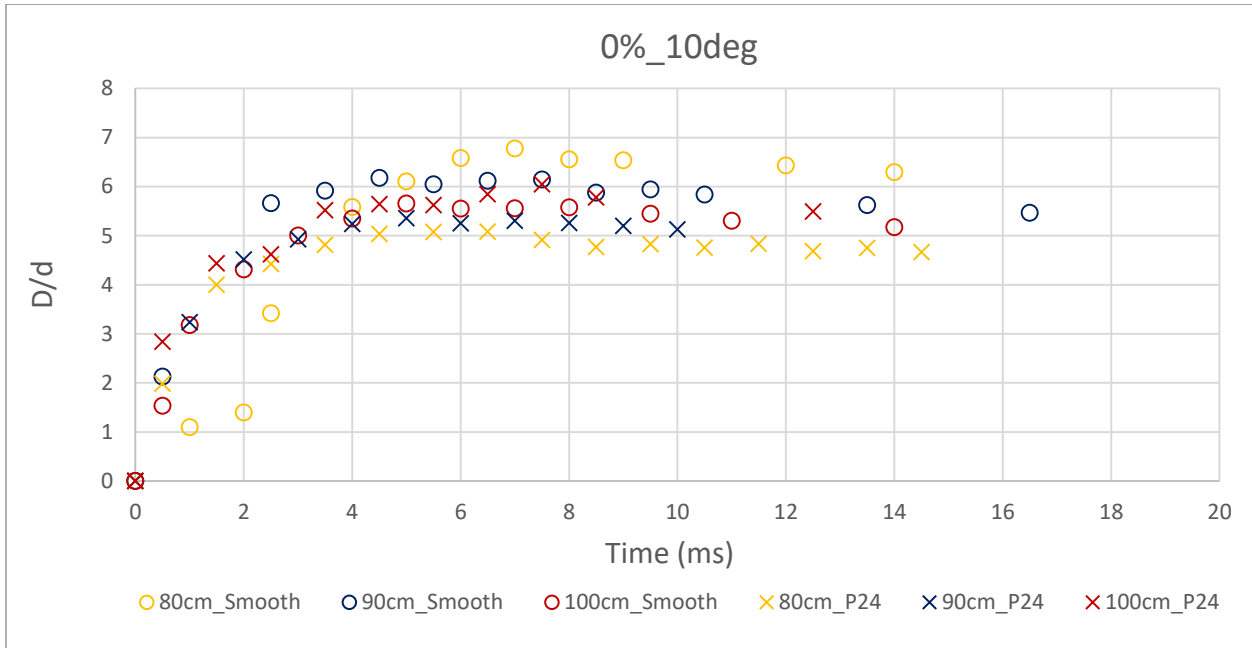


Figure 5-65: 0% w/w methanol solution ( $We=B. 765.89, We=909.43, We=971.39$  for 80, 90 and 100 cm respectively).

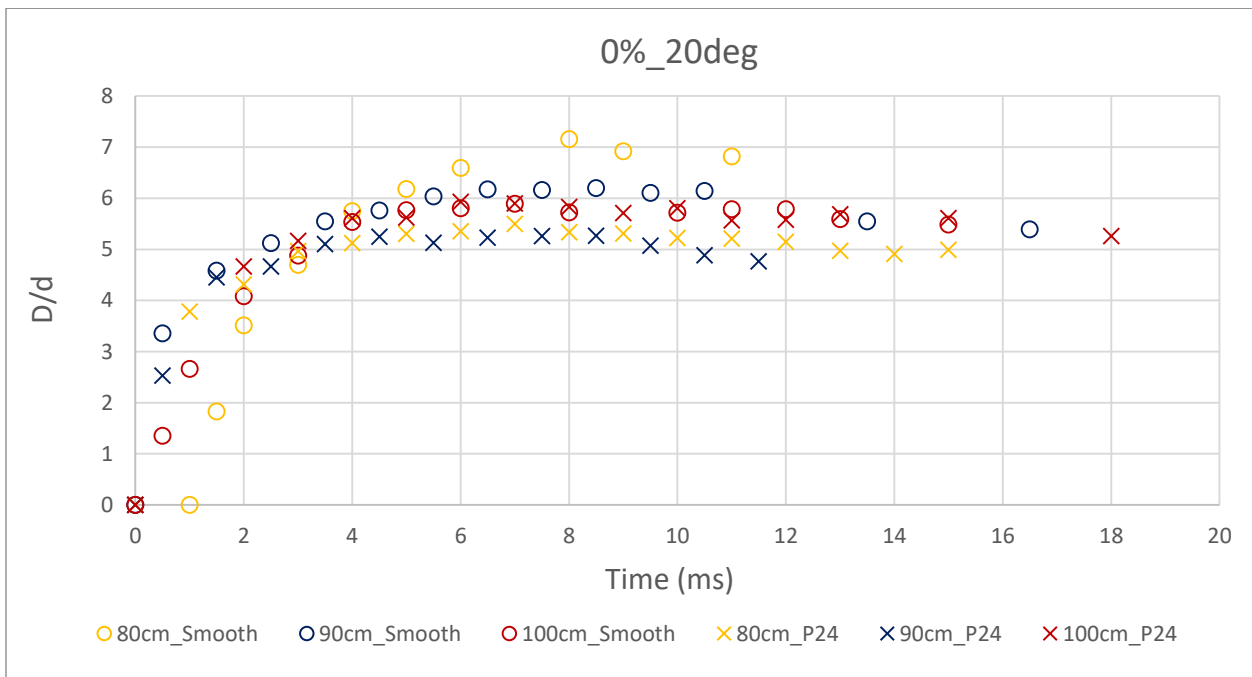
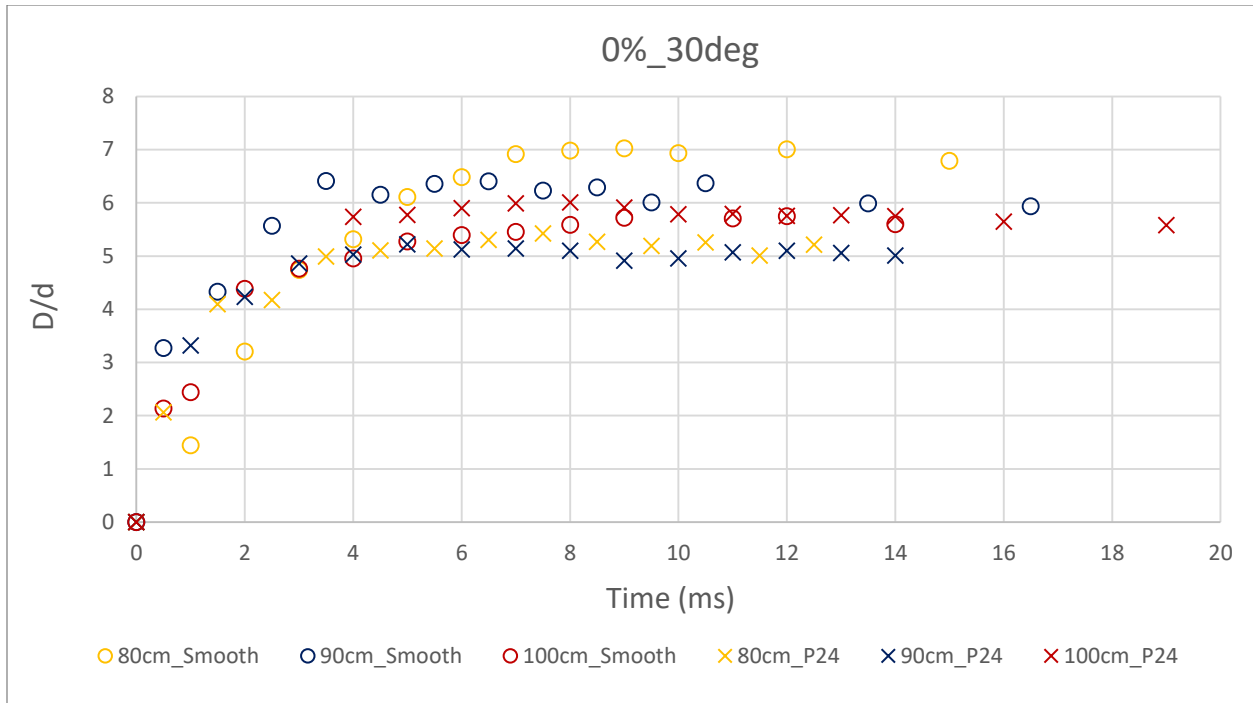


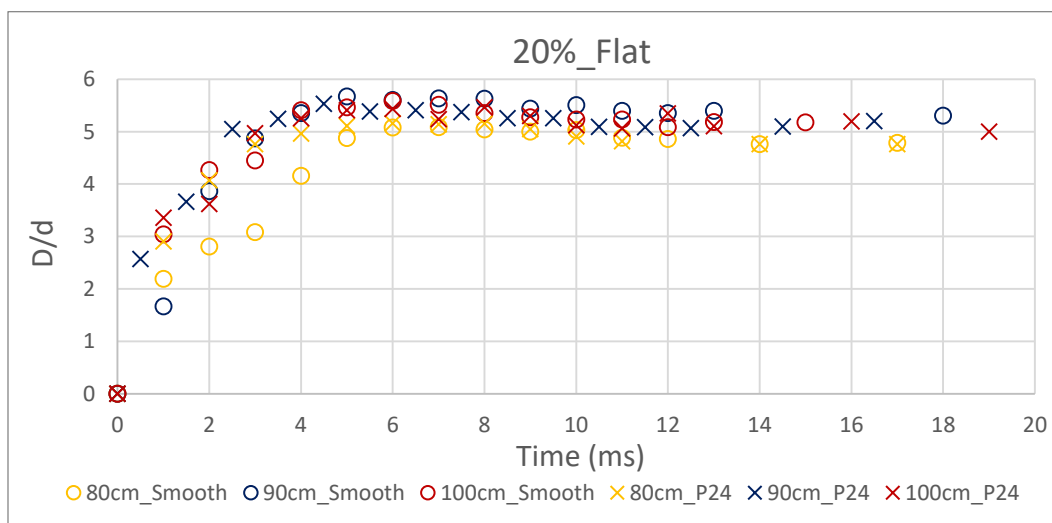
Figure 5-66: 0% w/w methanol solution ( $We=765.89, We=909.43, We=971.39$  for 80, 90 and 100 cm respectively).



**Figure 5-67: 0% w/w methanol solution ( $We=765.89, We=909.43, We=971.39$  for 80, 90 and 100 cm respectively).**

0% methanol (distilled water) is the solution which shows the biggest deviation of lamella spreading between the smooth and the coarse surface (as far as the 80cm and 90cm are concerned). This deviation can be spotted in diagrams of all inclination angles from the time of the impact till the lamella takes its maximum diameter length. However at 100cm signs for coarse and smooth surface almost coincide in all diagrams, so it can be assumed that for higher velocities surface roughness does not affect water spreading.

B. 20% w/w methanol



**Figure 5-68: 20% w/w methanol solution ( $We=986.35, We=1125.26, We=1197.2$  for 80, 90 and 100 cm respectively).**



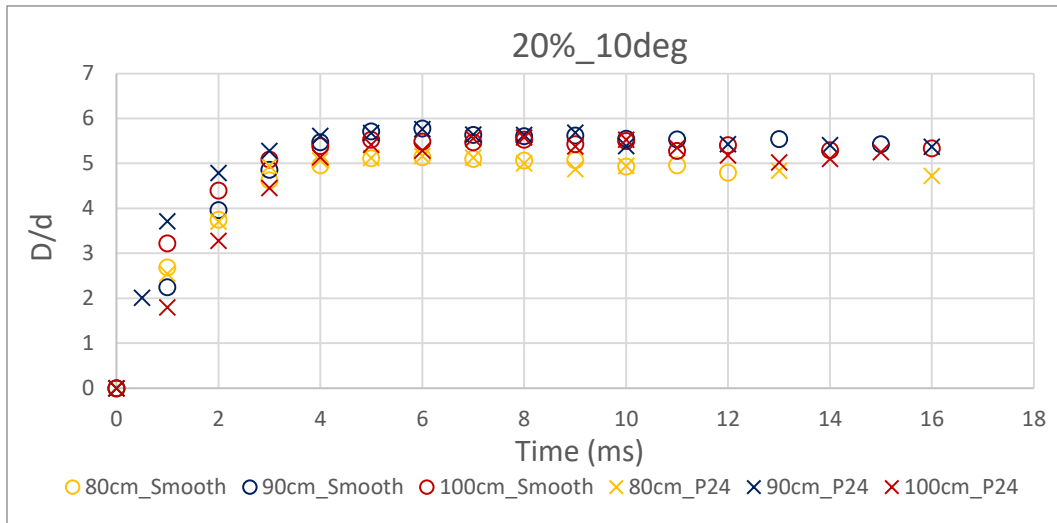


Figure 5-69: 20% w/w methanol solution ( $We=986.35$ ,  $We=1125.26$ ,  $We=1197.2$  for 80, 90 and 100 cm respectively).

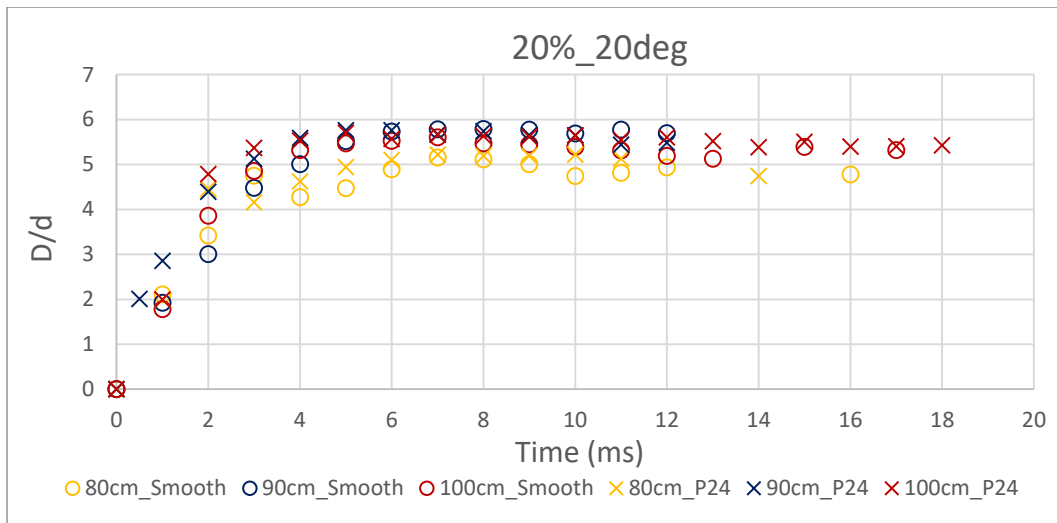


Figure 5-70: 20% w/w methanol solution ( $We=986.35$ ,  $We=1125.26$ ,  $We=1197.2$  for 80, 90 and 100 cm respectively).

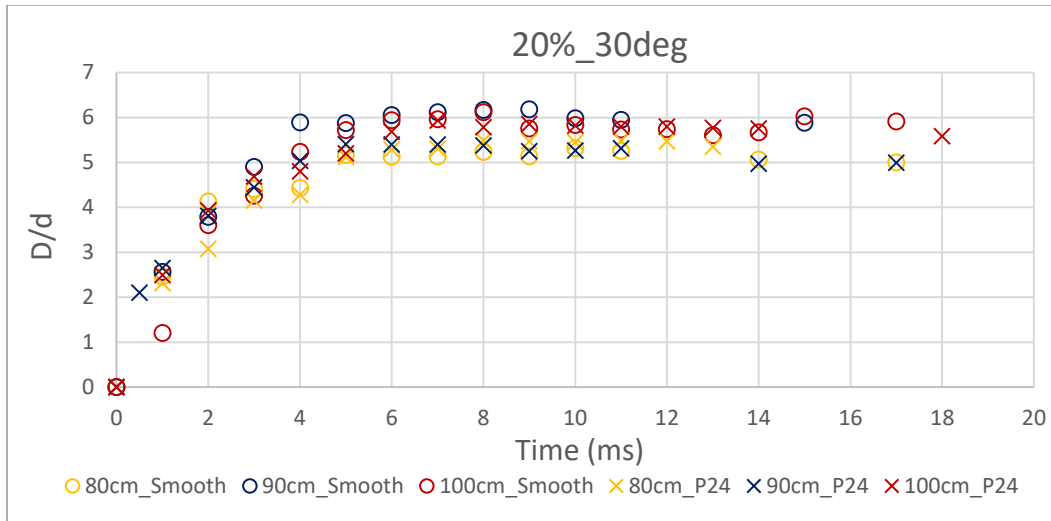


Figure 5-71: 20% w/w methanol solution ( $We=986.35$ ,  $We=1125.26$ ,  $We=1197.2$  for 80, 90 and 100 cm respectively).

At 20% water-methanol solution “x” and “o” signs of the same color (height) fall very close to each other especially for impacts on flat an 10degrees tilted substrates which indicates that surface roughness does not impede spreading. However, at 30degrees and 90cm height, the liquid lamella advances with the same speed (“x” and “o” signs follow the same slope path) but more in length at the smooth substrate.

C. 40% w/w methanol

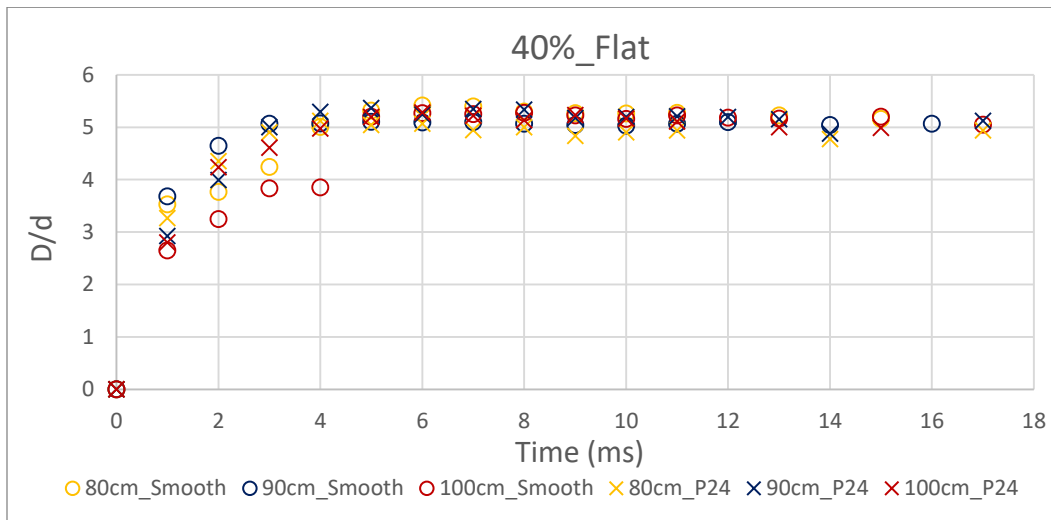


Figure 5-72: 40% w/w methanol solution ( $We=1233.33$ ,  $We=1390.58$ ,  $We=1462.99$  for 80, 90 and 100 cm respectively).

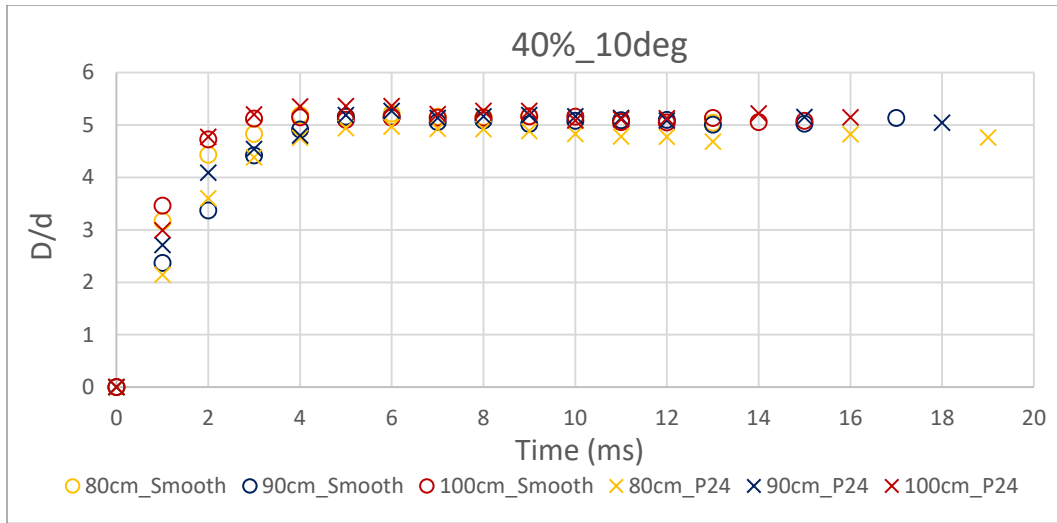


Figure 5-73: 40% w/w methanol solution ( $We=1233.33$ ,  $We=1390.58$ ,  $We=1462.99$  for 80, 90 and 100 cm respectively).

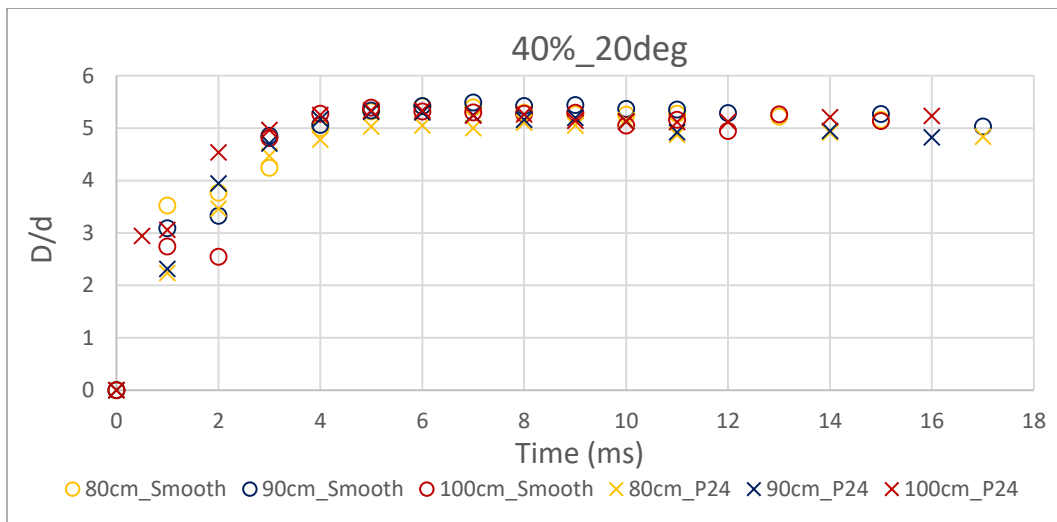


Figure 5-74: 40% w/w methanol solution ( $We=1233.33$ ,  $We=1390.58$ ,  $We=1462.99$  for 80, 90 and 100 cm respectively).

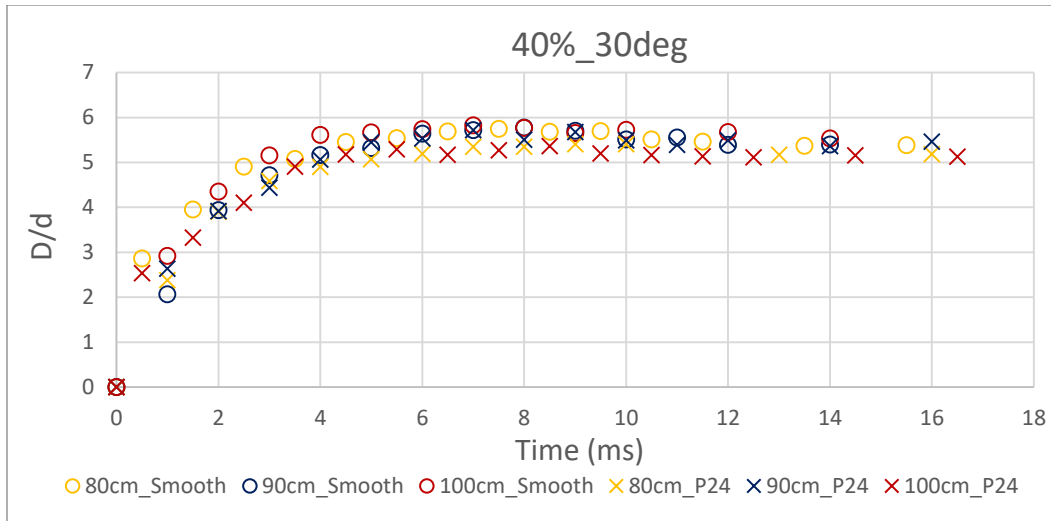


Figure 5-75: 40% w/w methanol solution ( $We=1233.33$ ,  $We=1390.58$ ,  $We=1462.99$  for 80, 90 and 100 cm respectively).

At 40% solution surface roughness continues to be unrelated to lamella spreading with a small exception at 30 degrees where “o” signs appear to have a little higher value comparing to the “x” signs of the same color.

D. 60% w/w methanol

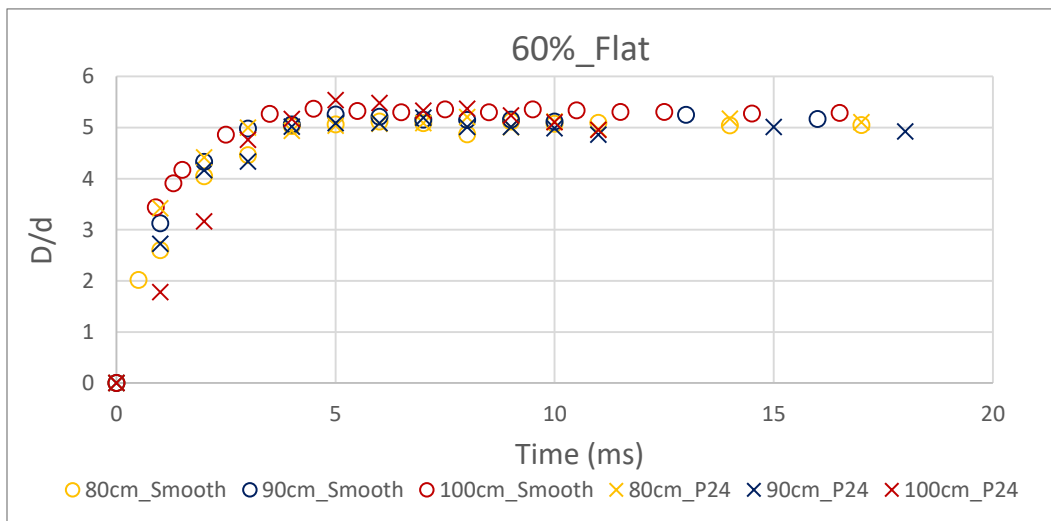


Figure 5-76: 60% w/w methanol solution ( $We=1124.52$ ,  $We=1295.45$ ,  $We=1431.38$  for 80, 90 and 100 cm respectively).

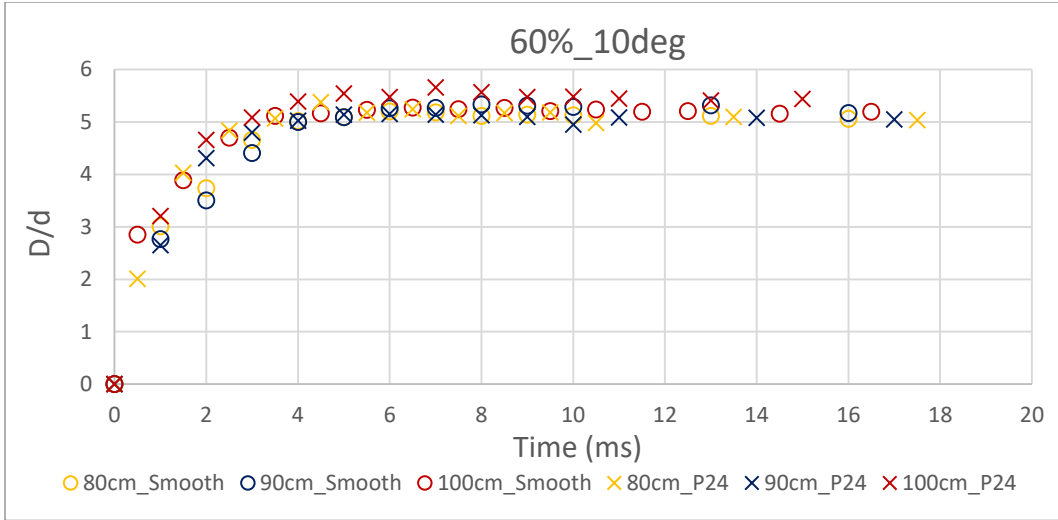


Figure 5-77: 60% w/w methanol solution ( $We=1124.52$ ,  $We=1295.45$ ,  $We=1431.38$  for 80, 90 and 100 cm respectively).

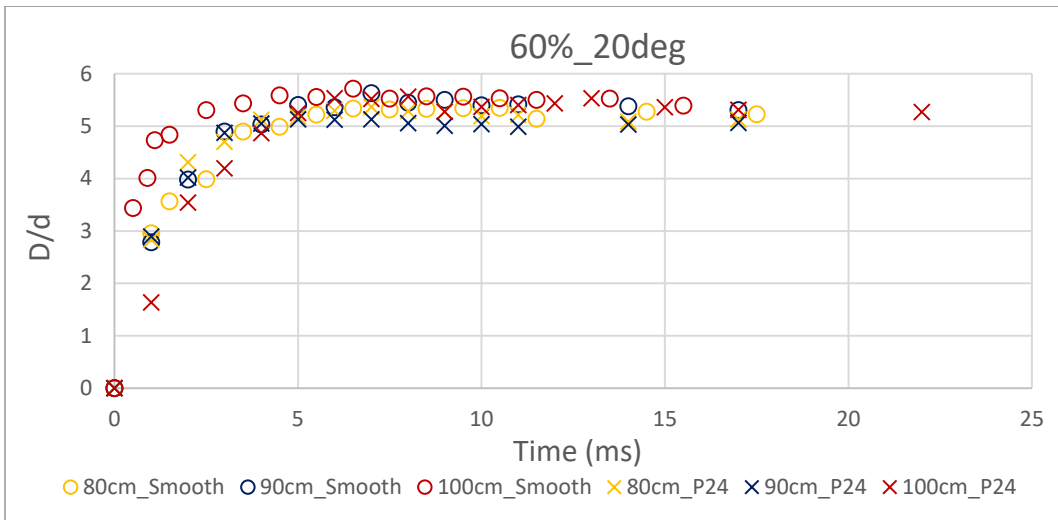


Figure 5-78: 60% w/w methanol solution ( $We=1124.52$ ,  $We=1295.45$ ,  $We=1431.38$  for 80, 90 and 100 cm respectively).

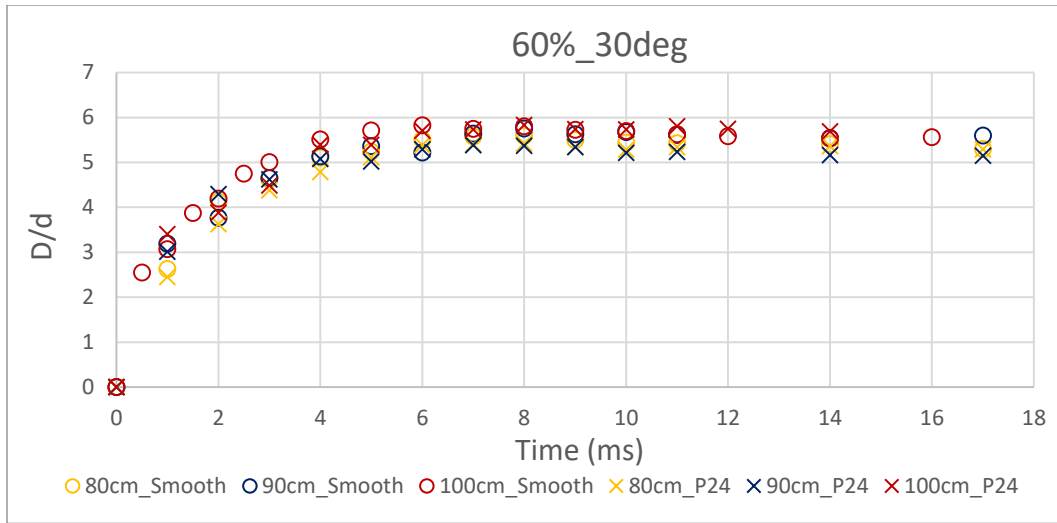


Figure 5-79: 60% w/w methanol solution ( $We=1124.52$ ,  $We=1295.45$ ,  $We=1431.38$  for 80, 90 and 100 cm respectively).

60% water-methanol solution appears to have the same pattern as 20% and 40% solutions which also applies at 30 degrees inclination. Furthermore, a sharper than usual slope at 100cm and 20degrees.

E. 80% w/w methanol

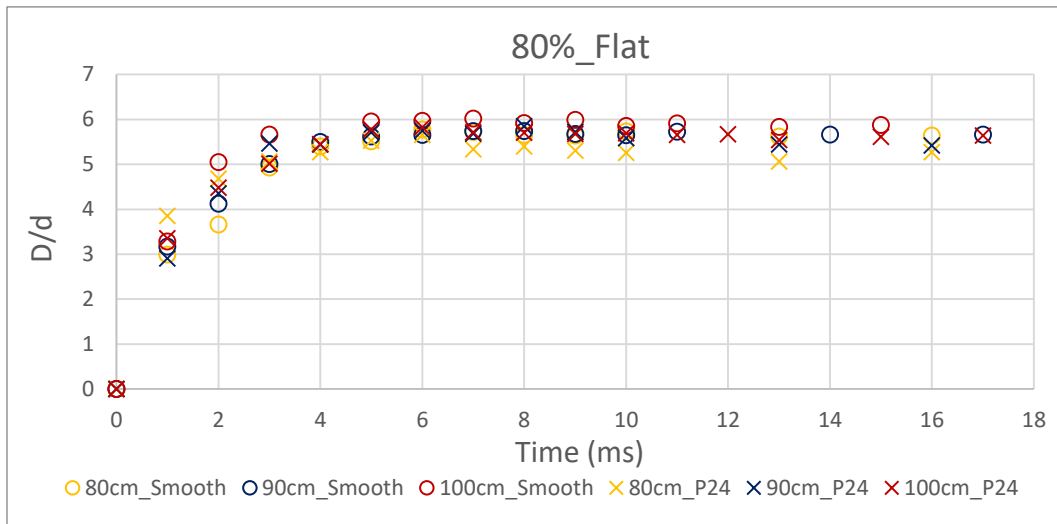


Figure 5-80: 80% w/w methanol solution ( $We=1183.17$ ,  $We=1321.50$ ,  $We=1448.52$  for 80, 90 and 100 cm respectively).

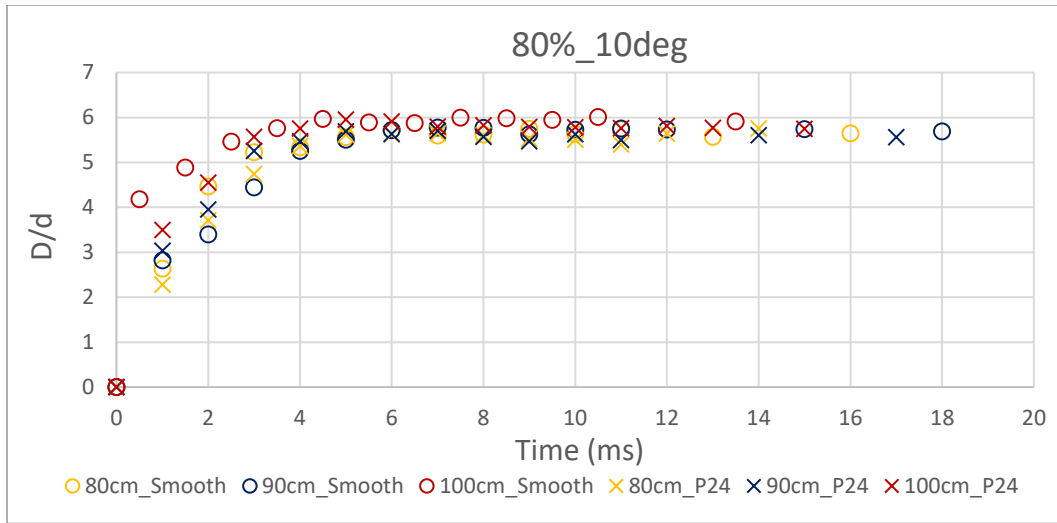


Figure 5-81: 80% w/w methanol solution ( $We=1183.17$ ,  $We=1321.50$ ,  $We=1448.52$  for 80, 90 and 100 cm respectively).

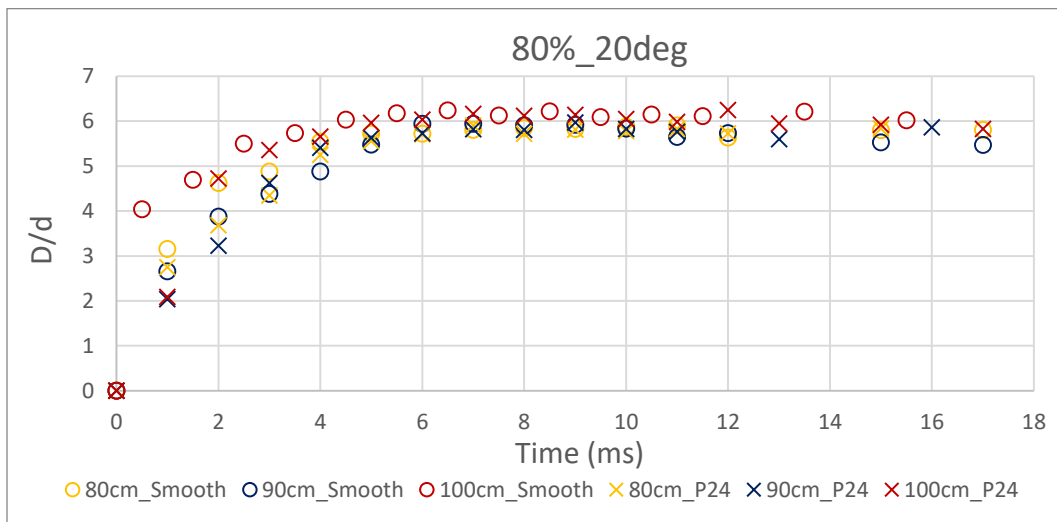
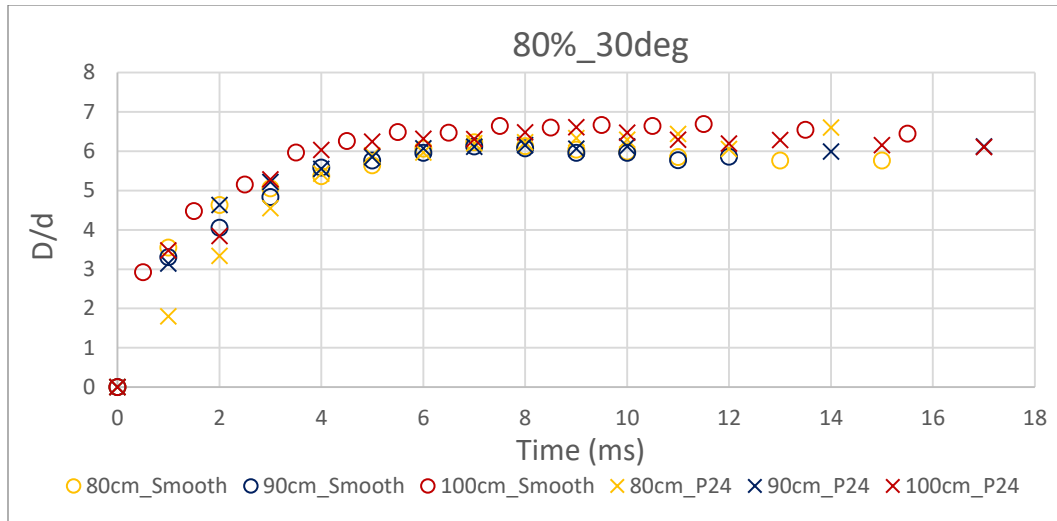


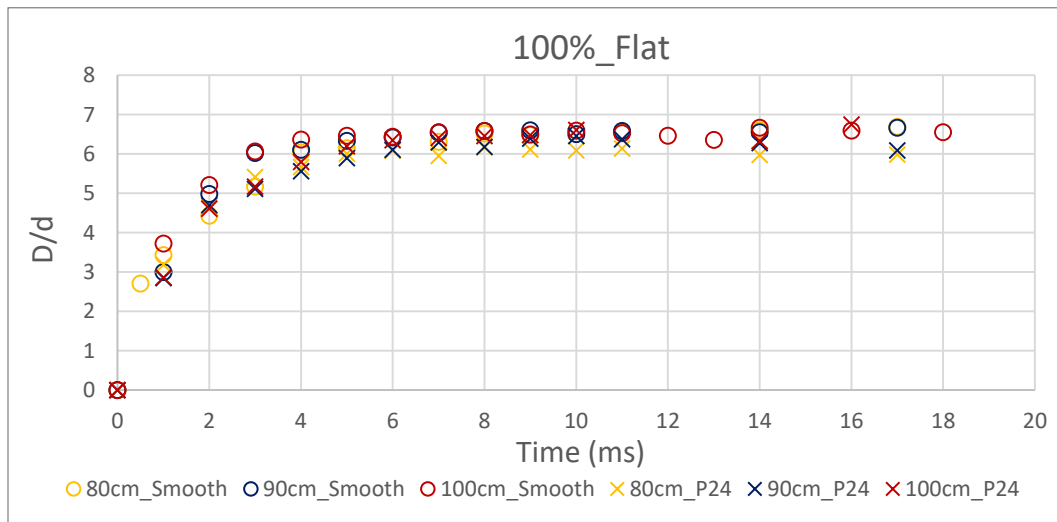
Figure 5-82: 80% w/w methanol solution ( $We=1183.17$ ,  $We=1321.50$ ,  $We=1448.52$  for 80, 90 and 100 cm respectively).



**Figure 5-83: 80% w/w methanol solution ( $We=1183.17$ ,  $We=1321.50$ ,  $We=1448.52$  for 80, 90 and 100 cm respectively).**

At 80% solution, a sharper slope can be detected, at 100cm for all tilted surfaces however surface roughness continues to play no role at spreading.

F. 100% w/w methanol



**Figure 5-84: 100% w/w methanol solution ( $We=1225.99$ ,  $We=1352.28$ ,  $We=1490.52$  for 80, 90 and 100 cm respectively).**



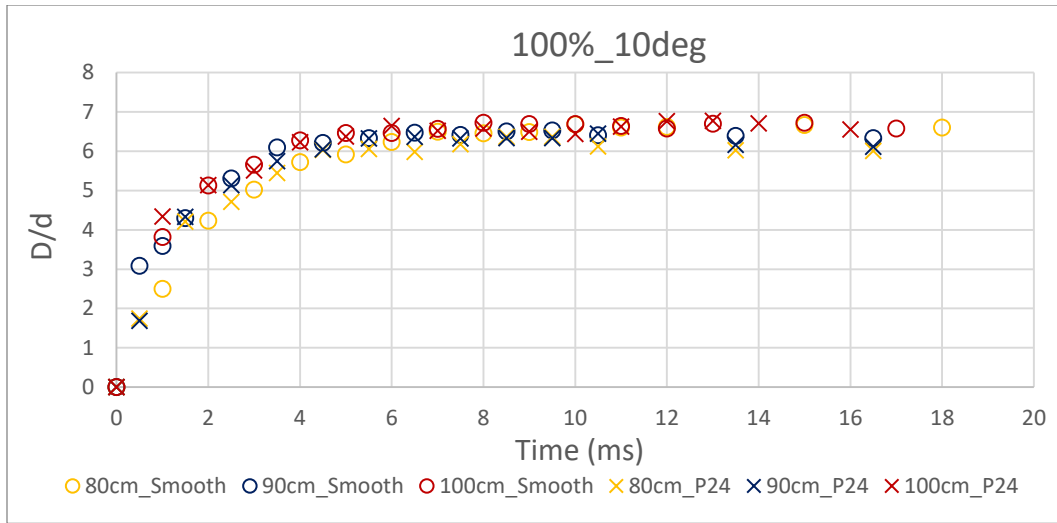


Figure 5-85: 100% w/w methanol solution ( $We=1225.99$ ,  $We=1352.28$ ,  $We=1490.52$  for 80, 90 and 100 cm respectively).

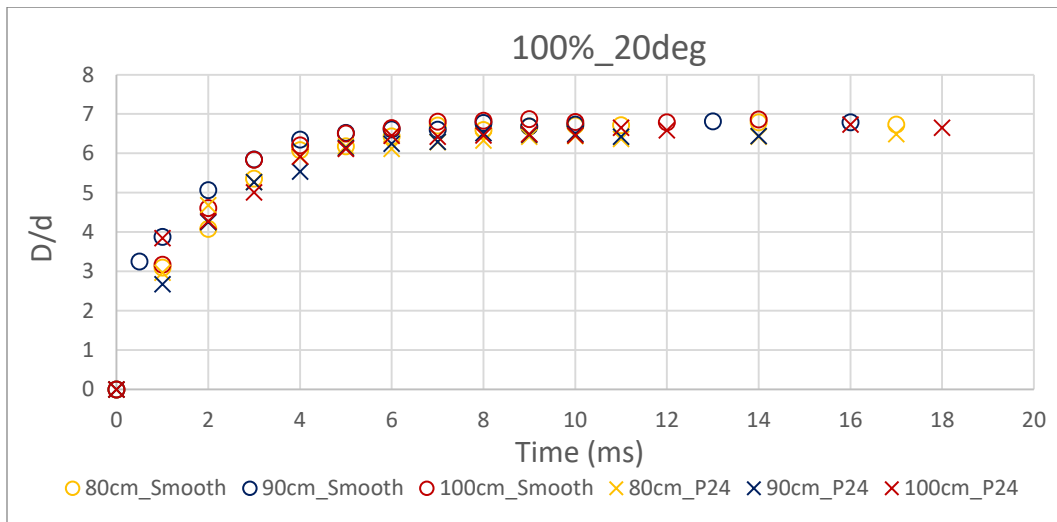
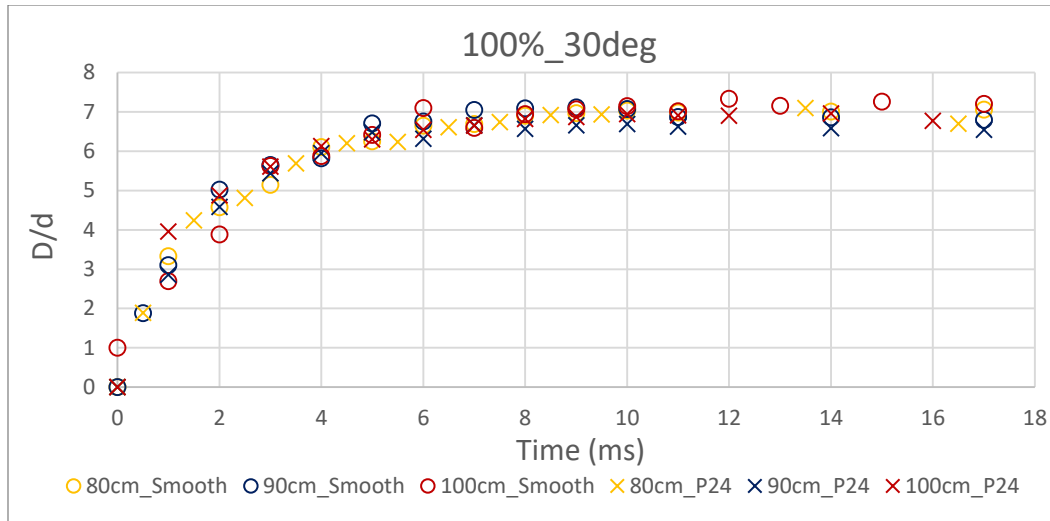


Figure 5-86: 100% w/w methanol solution ( $We=1225.99$ ,  $We=1352.28$ ,  $We=1490.52$  for 80, 90 and 100 cm respectively).



**Figure 5-87: 100% w/w methanol solution ( $We=1225.99$ ,  $We=1352.28$ ,  $We=1490.52$  for 80, 90 and 100 cm respectively).**

At 100% water methanol solution follows the same pattern concerning surface roughness.

Comparing all diagrams, we can mark that when using distilled water, the lamella diameter reaches its maximum values on the smooth substrate at all cases (both at flat and oblique surfaces).

### 5.3.3 Characteristic Time $T_o$

In this final chapter, an attempt was made to investigate how fast the evolution of the spreading occurs and how the moment of maximum spreading varies for the several parameters of the experiment. In order to approximate the Time- $D_{ND}$  curves of the spreading regime the function  $D_{ND}(t) = \beta(1 - e^{-t/T_o})$  (38) was selected (**Figure 5-88**). In (38),  $T_o$  represents the characteristic time of the equation and  $\beta$  represents the maximum value of  $D_{ND}$  in each case. This time refers to the time needed for the lamella to spread to obtain about 63% of its ultimate diameter. The smaller it is the faster the system reaches the  $\beta$  value. In the diagrams following, the lines between the points are added to show the inclination at which each point corresponds (1<sup>st</sup> point – 30 degrees inclined substrate, 2<sup>nd</sup> -20 degrees, 3<sup>rd</sup> – 10 degrees, 4<sup>th</sup> – flat, as  $We$  increases).

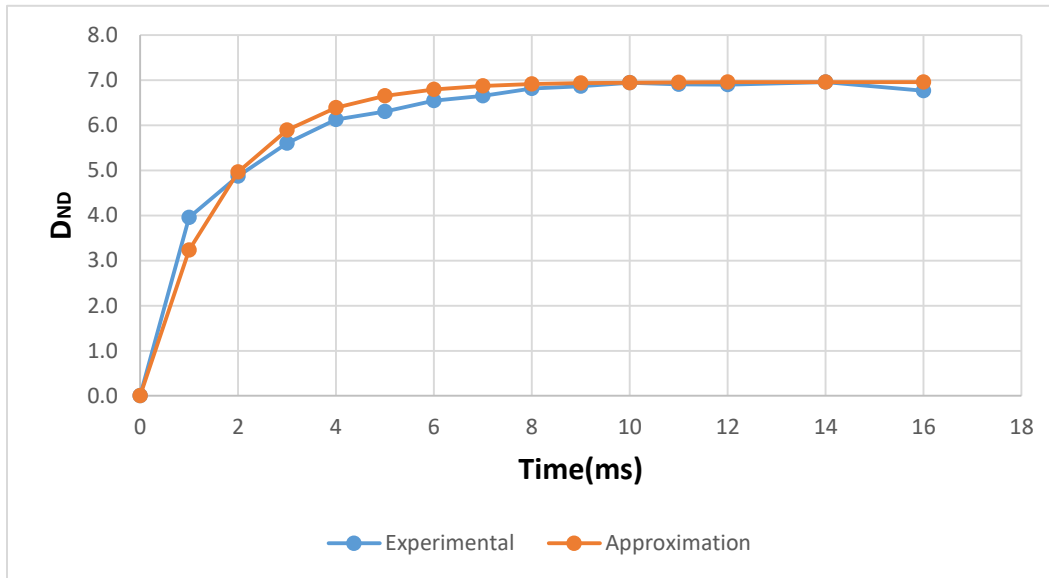


Figure 5-88: Approximation of the experimental curve based on equation (38)

The ensuing figures display the behavior of the characteristic time for each liquid solution of the experiment  $T_o$  and for all the altering parameters used.

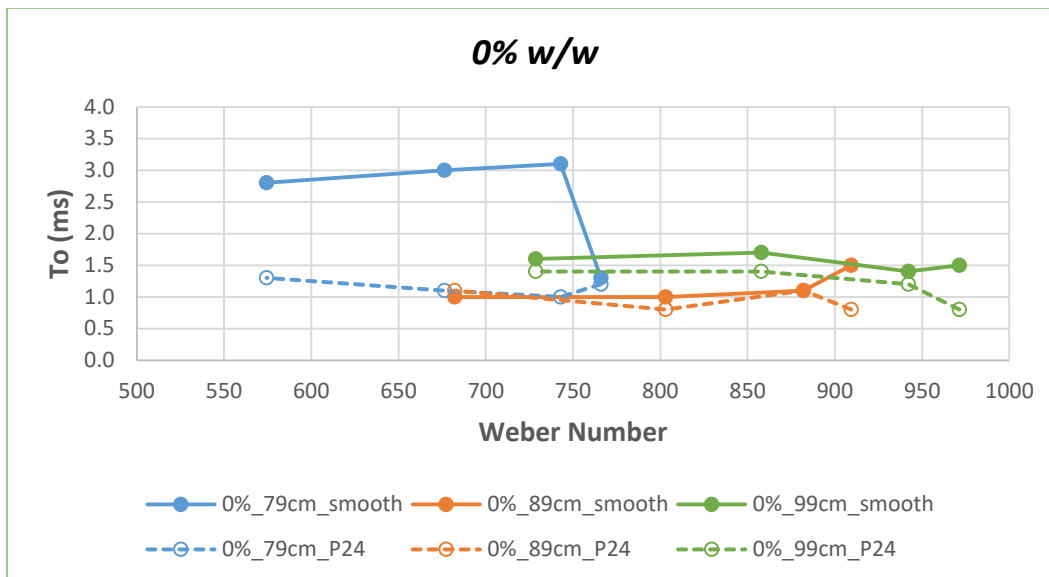
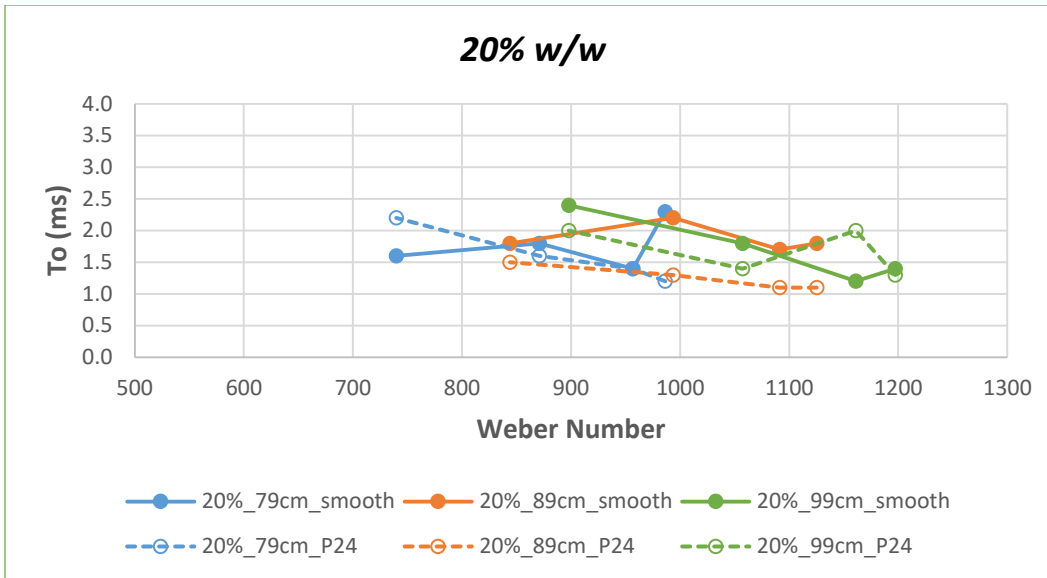


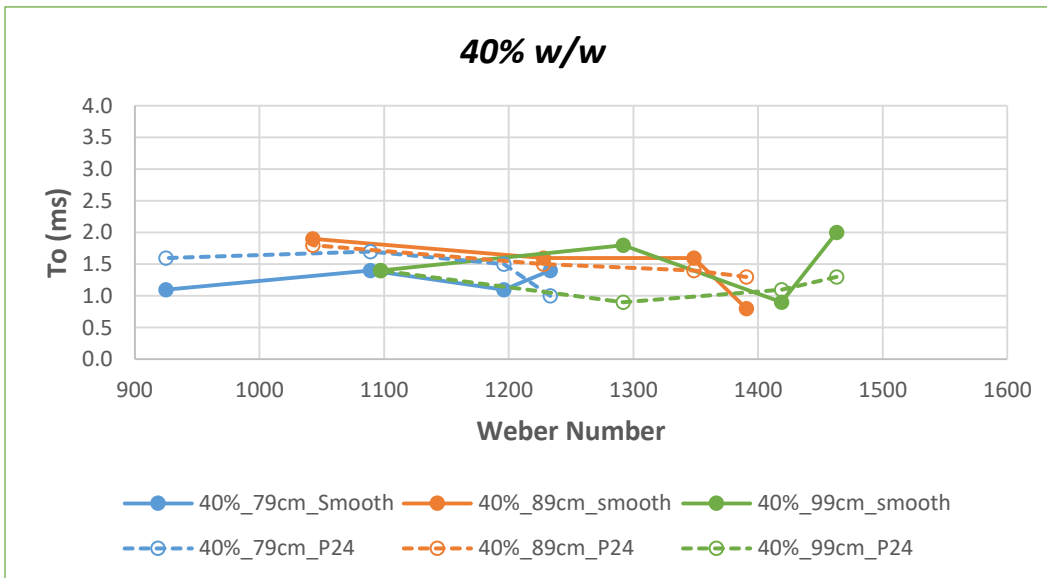
Figure 5-89: Characteristic time  $T_o$  values for pure water

Characteristic time  $T_o$  values for the 0% solution (Figure 5-89) have a small range of variation which is between 0.8 and 1.8 millisecond with the exception of 79cm on the smooth substrate which has a  $T_o$  close to 3 ms for 0,10 and 20 degrees inclination. Moreover, in all three heights,  $T_o$  is greater for the smooth substrate which indicates that liquid flows easier especially for lower impacting velocities (distance between  $T_o$  for 79cm smooth and P24 is larger than the ones of 89cm and 99cm).



**Figure 5-90: Characteristic time  $T_o$  values for 20% w/w methanol solution**

At 20% w/w solution  $T_o$  falls at all times between 1.1 and 2.4ms. Again the liquid spreads easier on the smooth substrate except 79cm-flat surface and 99cm 20degrees. Here at 89cm appears the most notable difference between the smooth and the coarse substrate ( $\Delta T_o=0.9s$  at 10 deg).



**Figure 5-91: Characteristic time  $T_o$  values for 40% w/w methanol solution**

At 40% w/w methanol solution the  $T_o$  range is also relatively narrow (0.8s-2s). In this case, we observe that for 79cm  $T_o$  for P24 appears higher for 0-20 degrees. However the difference is approximately 0.5 s, so we can assume that the spreading is not affected by surface roughness,

which also applies at 89cm. Concerning 99cm we have notable differences at 10 and 30 degrees inclination.

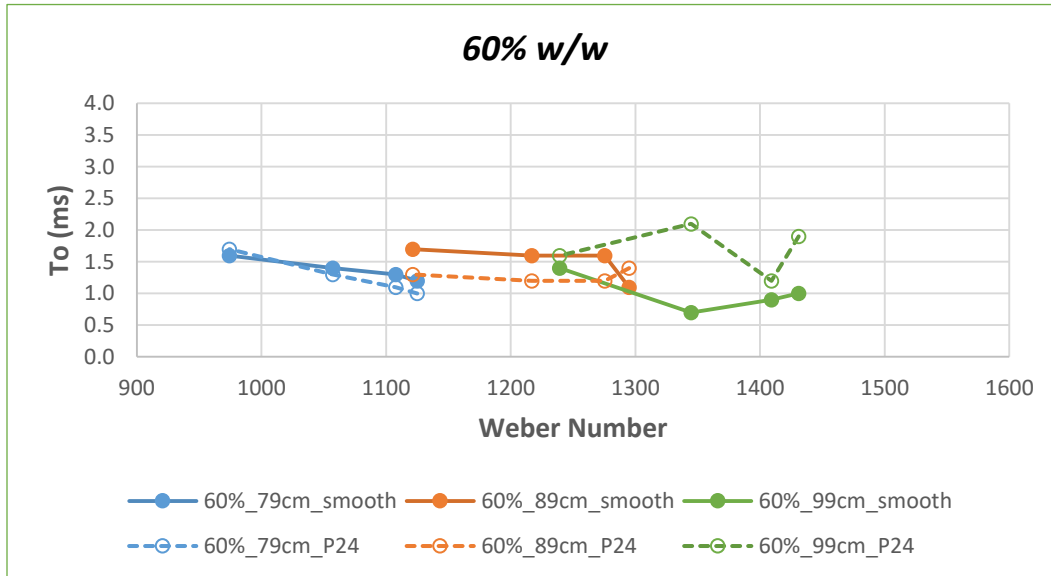


Figure 5-92: Characteristic time  $T_o$  values for 60% w/w methanol solution

In Figure 5-92 for the height of 79cm, the spreading displays similar characteristic times for both substrates, while as the inclination of the surface increases,  $T_o$  displays small decrease. On the contrary, for greater heights the substrate type seems to affect the characteristic time. For 89cm the solution reaches  $\beta$  faster when impacting on the coarse surface, while for 99cm the opposite happens (smaller characteristic times for the smooth surface).

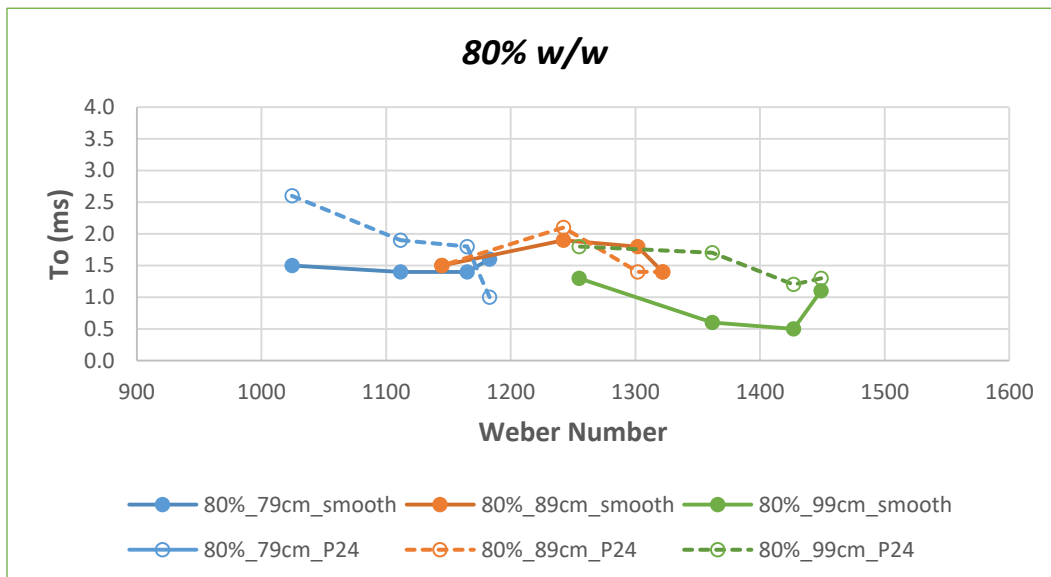
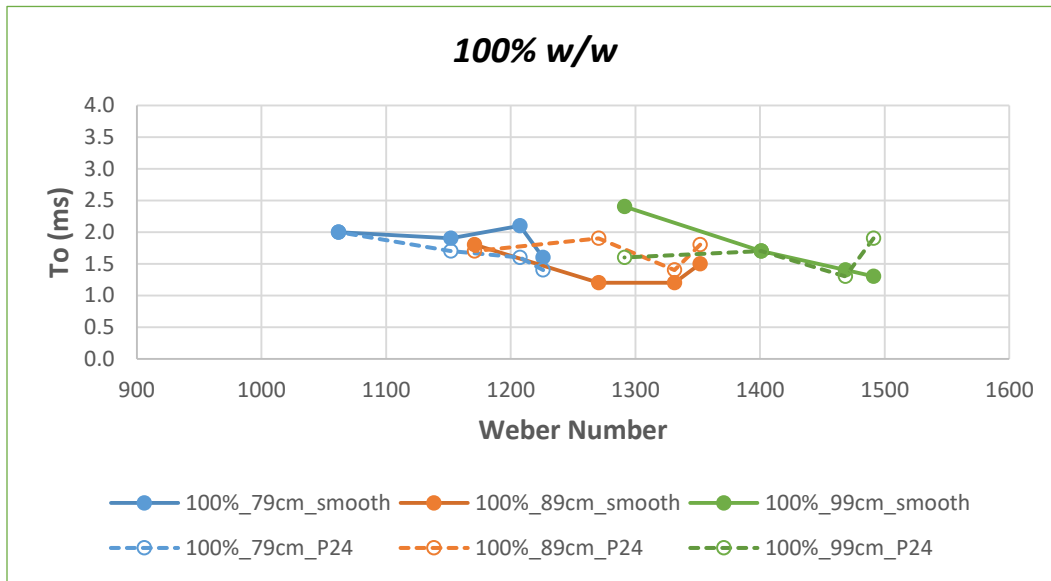


Figure 5-93: Characteristic time  $T_o$  values for 80% w/w methanol solution.

From Figure 5-93 no clear effect of the substrate inclination on the value of  $T_o$  can be determined. However, it appears that the solution reaches an equilibrium for the smooth surface faster than

for the coarse one (P24). This observation is more evident for fall heights of 0.79 and 0.99 cm where the  $T_o$  values are smaller for the smooth substrate.



**Figure 5-94: Characteristic time  $T_o$  values for 100% w/w methanol solution.**

Figure 5-94 displays the characteristic time  $T_o$  values for pure methanol which exhibit relatively small variations (below 0.3ms) between the two substrates for the majority of heights and inclinations. Exceptions are the cases of impact from 79cm at 10° inclined substrate and from 99cm at a 30° surface where the solutions attains  $\beta$  faster for the coarse substrate. The opposite effect is displayed for 0.99cm at a flat surface and for 0.89cm at 20° of inclination.

## 6 Conclusions

In the previous sections the experimental material has been analyzed via diagram depictions and compared to existing published research. Thesis conclusions are based on results collected for six different water-methanol solutions impacting from various heights on two substrates, of the same aluminum alloy but different roughness value, placed horizontally or tilted by 10, 20 or 30 degrees. Impact outcomes included a) prompt splashing especially when using distilled water (0% w/w water-methanol solution) and generally the rough substrate, b) corona splashing (40%, 60% and 80% w/w water-methanol solutions) which has been captured at all of its stages, lasting from 1 to 1.5 millisecond and c) simple deposition which was the main occurrence at 100% solution.

Photographic results of this experiment on flat surfaces were consistent with the Vander Wals criterion for splashing (either prompt or corona) with almost no discrepancies.

Corona splash analysis showed that, the crown forms symmetrically on both sides on a horizontal substrate, while for oblique impacts there is asymmetry which becomes stronger with increase of the inclination from 10° to 30°. The mixtures that present higher Weber numbers (40%, 80%) form more durable crowns than the 60% mixture, as the impingement height decreases and the inclination of the substrate increases. Furthermore, after result comparison with the Riboux Gordillo criterion (2019) for impacts on inclined surfaces, it was found that prediction of water (corona) splashing can be quite accurate. However, RG criterion does not fully comply with 20, 40 and 60% solutions and concerning 80% and 100% solutions, results are less compatible.

Analysis of lamella spreading factors revealed that surface roughness does not affect the advancing with an exception of distilled water, where the lamella reaches higher diameters on smooth substrates. Secondly at both smooth and rough substrates was revealed that the spreading diameter displays an increase, as the kinematic viscosity  $\nu$  decreases or the substrate inclination increases. The only liquid that sometimes deviates from this behavior is pure water. Moreover, during the calculation of the characteristic times  $T_0$ , which indicate how fast the lamella takes its maximum value, no significant trend was met, except that in most cases values were a little higher on the smooth than on the rough substrate or the deviation was neglectable.

We would also like to mention the points in the experiment that caused some of the results to be uncertain in order to be taken into consideration for any future work. As the data gathered from the experimental process were in form of photographic material the main obstacle was the background blurring of some images. The camera needed to be placed at a certain distance from the impacting droplet to avoid the falling of secondary droplets on the lenses. However, the lenses we used could not zoom enough in the point of the collision resulting in partial utilization of the CCD area. As a result, the obtained spatial resolution of the images was lower than what was possible. So, we would suggest the use of long working distance microscope lenses for improved spatial resolution of the droplet impingement images. Secondly, a highspeed camera would surely be an enhancement to the experiment as it will allow the full temporal resolution of droplet impingement. Finally, an interesting extension to the experiment that we did not have the time to

include, is the covering of the existing aluminum substrates with superhydrophobic coating and see how the impact outcome alters.



## 7 References

- Aboud, D. G. K., & Kietzig, A. M. (2015). Splashing Threshold of Oblique Droplet Impacts on Surfaces of Various Wettability. *Langmuir*, 31(36), 10100–10111. <https://doi.org/10.1021/acs.langmuir.5b02447>
- Almohammadi, H., & Amirfazli, A. (2019). Droplet impact: Viscosity and wettability effects on splashing. *Journal of Colloid and Interface Science*, 553, 22–30. <https://doi.org/10.1016/j.jcis.2019.05.101>
- Antonini, C., Villa, F., Bernagozzi, I., Amirfazli, A., & Marengo, M. (2013). *Drop rebound after impact : the role of receding contact angle*. <https://doi.org/10.1021/la4012372>
- Ashgriz, N. (2011). *Handbook of Atomization and Sprays*. Springer. <https://doi.org/10.1007/978-1-4419-7264-4>
- Bange, P. G., & Bhardwaj, R. (2015). *Computational study of bouncing and non-bouncing droplets impacting on superhydrophobic surfaces*. <https://doi.org/10.1007/s00162-015-0376-3>
- Bird, J. C., Tsai, S. S. H., & Stone, H. A. (2009). Inclined to splash: Triggering and inhibiting a splash with tangential velocity. *New Journal of Physics*, 11, 1–10. <https://doi.org/10.1088/1367-2630/11/6/063017>
- Burzynski, D. A., & Bansmer, S. E. (2019). Role of surrounding gas in the outcome of droplet splashing. *Physical Review Fluids*, 4(7). <https://doi.org/10.1103/PhysRevFluids.4.073601>
- Chandra, S., & Avedisian, C. T. (1991). On the collision of a droplet with a solid surface. *Proceedings of the Royal Society A: Mathematical, Physical and Engineering Sciences*, 432(1884), 13–41. <https://doi.org/10.1098/rspa.1991.0002>
- Charalampous, G., & Hardalupas, Y. (2017). Collisions of droplets on spherical particles. *Physics of Fluids*, 29(10). <https://doi.org/10.1063/1.5005124>
- Clanet, C. (2004). Maximal deformation of an impacting drop. *J. Fluid Mech. (2004), Vol. 517, Pp. 199–208.*, 517, 199–208. <https://doi.org/10.1017/S0022112004000904>
- Cossali, G. E., Coghe, A., & Marengo, M. (1997). The impact of a single drop on a wetted solid surface. *Experiments in Fluids*, 22(6), 463–472. <https://doi.org/10.1007/s003480050073>
- Driscoll, M. M., & Nagel, S. R. (2011). Ultrafast interference imaging of air in splashing dynamics. *Physical Review Letters*, 107(15), 1–4. <https://doi.org/10.1103/PhysRevLett.107.154502>
- Duez, C., Ybert, C., Clanet, C., & Bocquet, L. (2007). Making a splash with water repellency. *Nature Physics*, 3(3), 180–183. <https://doi.org/10.1038/nphys545>
- Eggers, J., Fontelos, M. A., Josserand, C., & Zaleski, S. (2010). *Drop dynamics after impact on a solid wall : Theory and simulations*. 1–14. <https://doi.org/10.1063/1.3432498>

- Girard, H. L., Soto, D., & Varanasi, K. K. (2019). Waterbowls: Reducing Impacting Droplet Interactions by Momentum Redirection. *ACS Nano*, *13*(7), 7729–7735. <https://doi.org/10.1021/acsnano.9b01301>
- Guo, Y., Lian, Y., & Sussman, M. (2016). Investigation of drop impact on dry and wet surfaces with consideration of surrounding air. *Physics of Fluids*, *28*(7). <https://doi.org/10.1063/1.4958694>
- Hao, J. (2017). Effect of surface roughness on droplet splashing. *Physics of Fluids*, *29*(12). <https://doi.org/10.1063/1.5005990>
- Jian, Z., Josserand, C., Popinet, S., Ray, P., & Zaleski, S. (2018). Two mechanisms of droplet splashing on a solid substrate. *Journal of Fluid Mechanics*, *835*, 1065–1086. <https://doi.org/10.1017/jfm.2017.768>
- Josserand, C., & Thoroddsen, S. T. (2016). Drop Impact on a Solid Surface. *Annual Review of Fluid Mechanics*, *48*(1), 365–391. <https://doi.org/10.1146/annurev-fluid-122414-034401>
- Latka, A., Boelens, A. M. P., Nagel, S. R., & De Pablo, J. J. (2018). Drop splashing is independent of substrate wetting. *Physics of Fluids*, *30*(2). <https://doi.org/10.1063/1.5012529>
- Latka, A., Strandburg-peshkin, A., Driscoll, M. M., Stevens, C. S., & Nagel, S. R. (2012). *Creation of Prompt and Thin-Sheet Splashing by Varying Surface Roughness or Increasing Air Pressure*. *054501*(August), 3–6. <https://doi.org/10.1103/PhysRevLett.109.054501>
- Li, E. Q., Vakarelski, I. U., & Thoroddsen, S. T. (2015). *Probing the nanoscale : the first contact of an impacting drop*. 1–12. <https://doi.org/10.1017/jfm.2015.643>
- Li, H. (2013). Drop Impact on Dry Surfaces with Phase Change. *PhD Thesis*, 296.
- Li, X., Ma, X., & Lan, Z. (2010). *Dynamic Behavior of the Water Droplet Impact on a Textured Hydrophobic / Superhydrophobic Surface : The Effect of the Remaining Liquid Film Arising on the Pillars ' Tops on the Contact Time*. *26*(3), 4831–4838. <https://doi.org/10.1021/la903603z>
- Liu, J., Vu, H., Yoon, S. S., Jepsen, R. A., & Aguilar, G. (2010). Splashing phenomena during liquid droplet impact. *Atomization and Sprays*, *20*(4), 297–310. <https://doi.org/10.1615/AtomizSpr.v20.i4.30>
- Mandre, S., Mani, M., & Brenner, M. P. (2009). Precursors to splashing of liquid droplets on a solid surface. *Physical Review Letters*, *102*(13), 4–7. <https://doi.org/10.1103/PhysRevLett.102.134502>
- Mani, M., Mandre, S., & Brenner, M. P. (2010). Events before droplet splashing on a solid surface. *Journal of Fluid Mechanics*, *647*, 163–185. <https://doi.org/10.1017/S0022112009993594>
- Moevius, L., Liu, Y., Wang, Z., & Yeomans, J. M. (2014). *Pancake Bouncing: Simulations and Theory and Experimental Verification*.
- Moreira, A. L. N., Moita, A. S., & Panão, M. R. (2010). Advances and challenges in explaining fuel

- spray impingement: How much of single droplet impact research is useful? *Progress in Energy and Combustion Science*, 36(5), 554–580.  
<https://doi.org/10.1016/j.pecs.2010.01.002>
- Mundo, C., Sommerfeld, M., & Tropea, C. (1995). Droplet-wall collisions: Experimental studies of the deformation and breakup process. *International Journal of Multiphase Flow*, 21(2), 151–173. [https://doi.org/10.1016/0301-9322\(94\)00069-V](https://doi.org/10.1016/0301-9322(94)00069-V)
- Palacios, J., Hernández, J., Gómez, P., Zanzi, C., & López, J. (2013). Experimental study of splashing patterns and the splashing/deposition threshold in drop impacts onto dry smooth solid surfaces. *Experimental Thermal and Fluid Science*, 44, 571–582.  
<https://doi.org/10.1016/j.expthermflusci.2012.08.020>
- Pochylý, F., Fialová, S., Kozubková, M., & Zavadil, L. (2010). *Study of the Adhesive Coefficient Effect on the Hydraulic Losses and Cavitation*. 3(4), 386–395.  
<https://doi.org/10.5293/IJFMS.2010.3.4.386>
- Qu, M., He, J., & Zhang, J. (2007). *Superhydrophobicity, Learn from the Lotus Leaf*.
- Range, K. (1998). *Influence of Surface Roughness on Liquid Drop Impact*. 30(203), 16–30.
- Riboux, G., & Gordillo, J. M. (2014). Experiments of drops impacting a smooth solid surface: A model of the critical impact speed for drop splashing. *Physical Review Letters*, 113(2), 1–5.  
<https://doi.org/10.1103/PhysRevLett.113.024507>
- Rioboo, R., Delattre, B., Duvivier, D., Vaillant, A., & Coninck, J. De. (2012). Superhydrophobicity and liquid repellency of solutions on polypropylene. *Advances in Colloid and Interface Science*, 175, 1–10. <https://doi.org/10.1016/j.cis.2012.03.003>
- Rioboo, R., Marengo, M., & Tropea, C. (2002). *Time evolution of liquid drop impact onto solid, dry surfaces*. 33, 112–124. <https://doi.org/10.1007/s00348-002-0431-x>
- Rioboo, Romain, & Marengo, M. (2001). *Outcomes from a Drop Impact on Solid Surfaces. February 2014*. <https://doi.org/10.1615/AtomizSpr.v11.i2.40>
- Roisman, I. V., Lembach, A., & Tropea, C. (2015). Drop splashing induced by target roughness and porosity: The size plays no role. *Advances in Colloid and Interface Science*, 222, 615–621.  
<https://doi.org/10.1016/j.cis.2015.02.004>
- Roisman, I. V., Berberovi, E., Tropea, C., Roisman, I. V., Berberovi, E., & Tropea, C. (2014). *Inertia dominated drop collisions. I. On the universal flow in the lamella Inertia dominated drop collisions. I. On the universal flow in the lamella*. 052103(2009).  
<https://doi.org/10.1063/1.3129282>
- Šikalo, Š., Tropea, C., & Ganić, E. N. (2005). Impact of droplets onto inclined surfaces. *Journal of Colloid and Interface Science*, 286(2), 661–669. <https://doi.org/10.1016/j.jcis.2005.01.050>
- Stevens, C. S. (2014). Scaling of the splash threshold for low-viscosity fluids. *Epl*, 106(2), 3–8.  
<https://doi.org/10.1209/0295-5075/106/24001>

- Stow, C. D., & Hadfield, M. G. (1981). An experimental investigation of fluid flow resulting from the impact of a water drop with an unyielding dry surface. *Proceedings of the Royal Society of London. A. Mathematical and Physical Sciences*, 373(1755), 419–441. <https://doi.org/10.1098/rspa.1981.0002>
- Tanner. (1979). *The spreading of silicone oil drops on horizontal surfaces*. 1473.
- Tate, T. (1864). *on the Magnitude of a Drop of Liquid*. 176–180.
- The Royal Society is collaborating with JSTOR to digitize, preserve, and extend access to Proceedings of the Royal Society of London. © www.jstor.org. (n.d.). *Society*.
- Thoroddsen, S. T., Etoh, T. G., & Takehara, K. (2003). Air entrapment under an impacting drop. *Journal of Fluid Mechanics*, 478(478), 125–134. <https://doi.org/10.1017/S0022112002003427>
- Thoroddsen, S. T., Etoh, T. G., & Takehara, K. (2008). High-Speed Imaging of Drops and Bubbles. *Annual Review of Fluid Mechanics*, 40(1), 257–285. <https://doi.org/10.1146/annurev.fluid.40.111406.102215>
- Ukiwe, C., & Kwok, D. Y. (2005). *On the Maximum Spreading Diameter of Impacting Droplets on Well-Prepared Solid Surfaces*. 31, 666–673. <https://doi.org/10.1021/la0481288>
- Vadillo, D. C., Soucemarianadin, A., Delattre, C., & Roux, D. C. D. (2012). *Dynamic contact angle effects onto the maximum drop impact spreading on solid surfaces Dynamic contact angle effects onto the maximum drop impact spreading*. 122002(2009). <https://doi.org/10.1063/1.3276259>
- Vander Wal, R. L., Berger, G. M., & Mozes, S. D. (2006). The splash/non-splash boundary upon a dry surface and thin fluid film. *Experiments in Fluids*, 40(1), 53–59. <https://doi.org/10.1007/s00348-005-0045-1>
- Xu, L., Barcos, L., & Nagel, S. R. (2007). Splashing of liquids: Interplay of surface roughness with surrounding gas. *Physical Review E*, 76(6), 1–5. <https://doi.org/10.1103/physreve.76.066311>
- Xu, L., Zhang, W. W., & Nagel, S. R. (2005). Drop splashing on a dry smooth surface. *Physical Review Letters*, 94(18), 1–4. <https://doi.org/10.1103/PhysRevLett.94.184505>
- Yarin, A. L., & Weiss, D. A. (1995). Impact of Drops on Solid Surfaces: Self-Similar Capillary Waves, and Splashing as a New Type of Kinematic Discontinuity. *Journal of Fluid Mechanics*, 283, 141–173. <https://doi.org/10.1017/S0022112095002266>
- Yildirim, O. E., Xu, Q., Basaran, O. A., Yildirim, O. E., Xu, Q., & Basaran, O. A. (2005). *Analysis of the drop weight method Analysis of the drop weight method*. 062107. <https://doi.org/10.1063/1.1938227>
- Yokoi, K. (2011). *Numerical studies of droplet splashing on a dry surface : triggering a splash with the dynamic contact angle  $\theta$* . 1, 5120–5123. <https://doi.org/10.1039/c1sm05336a>

